THE UNIVERSITY OF CHICAGO

MOLECULAR MECHANISMS OF THE ACTIN CYTOSKELETON

A DISSERTATION SUBMITTED TO

THE FACULTY OF THE DIVISION OF THE PHYSICAL SCIENCES

AND

THE FACULTY OF THE DIVISION OF THE BIOLOGICAL SCIENCES

AND THE PRITZKER SCHOOL OF MEDICINE

IN CANDIDACY FOR THE DEGREE OF

DOCTOR OF PHILOSOPHY

GRADUATE PROGRAM IN BIOPHYSICAL SCIENCES

BY

VILMOS ZSOLNAY

CHICAGO, ILLINOIS

AUGUST 2023

Table of Contents

List of Figures

List of Tables

Acknowledgements

I have had the great pleasure of working with a long list of wonderful colleagues and collaborators as I have pursued the research presented in these chapters.

I would like to acknowledge my thesis advisors David Kovar and Gregory Voth, who have provided me with access to a wide range of research tools and fascinating research questions. They entrusted me with the latitude and autonomy to follow my interests, and it has been a delightful way to conduct scientific research.

My advisors have also attracted fantastic group members that I have enjoyed having as my colleagues. I want to thank Glen Hocky, Tamara Bidone, Harshwardhan Katkar, Fikret Aydin, Cristian Suarez, Rachel Kadzik, and Kaitlin Homa for generously investing in my training and setting me up to have successes early on. I want to thank Sriramvignesh Mani, Yihang Wang, Timothy Loose, Arpa Hudait, Daniel Beckett, Kuntal Ghosh, Sarah Yde, and Kash Baboolall for never hesitating to entertain an impromptu meeting to talk through some data or iterate on an out-there research idea.

I am grateful to have had Thomas Pollard and Margaret Gardel as close collaborators. They have been exceptionally generous, energetic, and insightful, and their passion is contagious.

Michele Wittels, Juliana Feder, and Adam Hammond perpetually amaze me with their dedication to providing sound advice and valuable opportunities for the Biophysical Sciences graduate students.

I thank Dirk Gillespie for providing a wonderful research opportunity before graduate school.

I am grateful to my family and friends for support and fulfillment outside of academics. I especially want to thank my parents for endless encouragement.

Abstract

Cells need to move, divide, change shape, transport cargo, and explore their environment. To perform this diverse array of functions, cells dynamically construct and rearrange actin filaments into distinct networks through interactions between actin and unique combinations of actin-binding proteins (ABPs). These proteins constitute the actin cytoskeleton. The protein-protein interactions, which typically occur on the scale of ångströms to nanometers, lead to profound changes in the emergent actin filament networks at the micron scale. By understanding the mechanisms that govern the behavior at the molecular level, one can gain a deeper understanding of the higher-order structures that emerge. This appreciation is key to identifying how healthy cells carry out important cytoskeletal functions and how unhealthy cells, some with only one amino acid mutated, fail to do so.

In recent years, research has demonstrated that the behavior of a wide range of ABPs can be modulated by mechanical forces. The effect of this is that cells can utilize the actin cytoskeleton in ways that are tailored to particular mechanical stimuli. Interestingly, different forms of mechanoregulation have been reported. Some systems respond when forces are applied to the ABP, as in the case of the actin nucleation and elongation factor, formin. For other systems, the behavior of the ABP changes when force is applied to the actin filaments themselves, as in the case of mechanosensitive LIM domains. Additionally, the effect of the force can either enhance ABP binding or activity, as in the case of LIM and certain isoforms of formin, respectively, or limit protein activity, as in one isoform of formin.

However, many of these interesting phenomena have not been explained in mechanistic detail. Here, I present a body of work that explains the molecular origins of important behaviors

and interactions that govern the actin cytoskeleton. First, I use classical molecular dynamics simulations to elucidate why one end of a bare actin filament has much faster polymerization kinetics than the other, and report that the conformational change between actin monomers in solution and actin subunits in filaments occurs gradually as additional subunits are added. In the second project, I apply forces to actin filaments using steered molecular dynamics. This reveals that a distinct residue switch governs at which interface the actin filament fragments. However, before fragmentation occurs, a metastable 'cracked' state presents a unique strain-induced binding surface. I find that mechanosensitive LIM domains bind the crack, and these binding poses offer natural explanations for what conveys mechanosensitivity to LIM domains. Third, I use a coarse grained model to simulate the process of cytokinetic ring assembly in a fission yeast cell. These results demonstrate how the mechanoregulation of formin impacts the higher-order emergent phenomenon of ring formation. Fourth, I set up and use a microfluidics apparatus to exert forces onto individual formin molecules anchored to the coverslip. This reveals that a single formin dimer isoform can be either enhanced or inhibited when subjected to tension. Lastly, I report on ongoing projects aimed at understanding the mechanism of spontaneous actin filament nucleation and inorganic phosphate release, and suggest future directions.

Chapter 1: Introduction

1.1 The dynamic cell

If you surveyed a random sample of people and asked them to describe their mental picture of a cell, I suspect the most common response would be a circle with another circle inside of it. The larger circle would represent the cell membrane and the smaller one would represent the nucleus. This is the idea people seem to be left with from high school biology, and as with many things from your high school science curriculum, you later find out the reality is so much more fascinating, it's surprising your teachers didn't start with that.

There's this amazing movie of a white blood cell chasing around a bacterium recorded on 16-mm film by David Rogers in the 1950s (1). The movements of the neutrophil are so dynamic and so concerted that, upon remembering it lacks eyes or a brain, you can't help but wonder how it all works. I initially saw this in my first year of graduate school and rewatch it every so often. More recent examples are even more amazing in their level of detail and ability to convey the three-dimensionality of a cell's dynamics as it navigates complex environments (2).

Taking a step back, one can begin to appreciate that the dynamic rearrangements of a cell's shape, in addition to enabling the neutrophil to chase down a pathogen, also enable various cell types to, for example, divide into two daughter cells, probe the environment with finger-like protrusions, make connections with neighboring cells during development, ingest cargo through endocytosis, or fill in the space left by a wound. A cell's shape and its ability to rearrange it is important. Without this capability, cells do not divide, wounds do not heal, babies do not develop, and white blood cells do not chase down and ingest bacteria. One can easily imagine scenarios where researchers and clinicians alike would want to restore or inhibit these functions in various types of cells.

Amazingly, each of these dynamic processes utilizes the same building blocks to perform the diverse set of tasks described above. In the same way that a large number of bricks can be arranged into a giant pyramid, a great wall, or a town of single-family homes, the actin cytoskeleton uses the same building block, actin, to construct a number of distinct network architectures. At the leading edge of a cell, actin assembles into a meshwork of short, branched filaments that pushes on the cell membrane to propel it forward. In a cytokinetic ring, actin is assembled into long, straight filaments that become bundled together to provide a substrate for molecular motors to exert and propagate forces upon. The factors determining these different network properties are a suite of actin-binding proteins (ABPs) that interact with actin, as well as each other, to dynamically reshape the emergent filament architecture (3). Altogether, these components make up the actin cytoskeleton.

Furthermore, actin is present in all eukaryotic cells and is highly conserved among vastly different lineages (4). Organisms as diverse as orangutans, dandelions, shrimp, and baker's yeast all utilize very similar machinery to carry out cytoskeletal functions and morphological change. In addition to having highly conserved actin primary sequences, eukaryotic cells also share homologous versions of the ABPs that carry out the same or similar functions.

1.2 Properties of actin

Given the importance and diversity of functions that actin mediates within cells, one might naturally ask how it works. Decades of scientific effort into this area of research have yielded many interesting and important insights into the properties of actin. The most fundamental among these is that actin monomers assemble into actin polymer filaments above a critical concentration (Fig. 1.1A) (5). The two ends of the filament are polarized and have distinct properties, where one end,

the ‘barbed’ end, has much higher rate kinetics than the other, ‘pointed’ end (Fig. 1.1A). The net effect of the higher on and off rates is that the barbed end elongates significantly faster than the pointed end. Additionally, actin binds ATP (adenosine triphosphate) (Fig. 1.1B). The bound ATP nucleotide can be hydrolyzed into ADP (adenosine diphosphate) with the inorganic phosphate (P_i) being released sometime later. These hydrolysis and P_i-release reactions result in three distinct nucleotide states of actin: ATP, ADP-P_i, and ADP. The state of the nucleotide can have profound effects, not only on each of the kinetic rates at the barbed and pointed end of an actin-only system (Fig. 1.1A), but also on the interactions that actin has with the ABPs that shape actin filament networks.

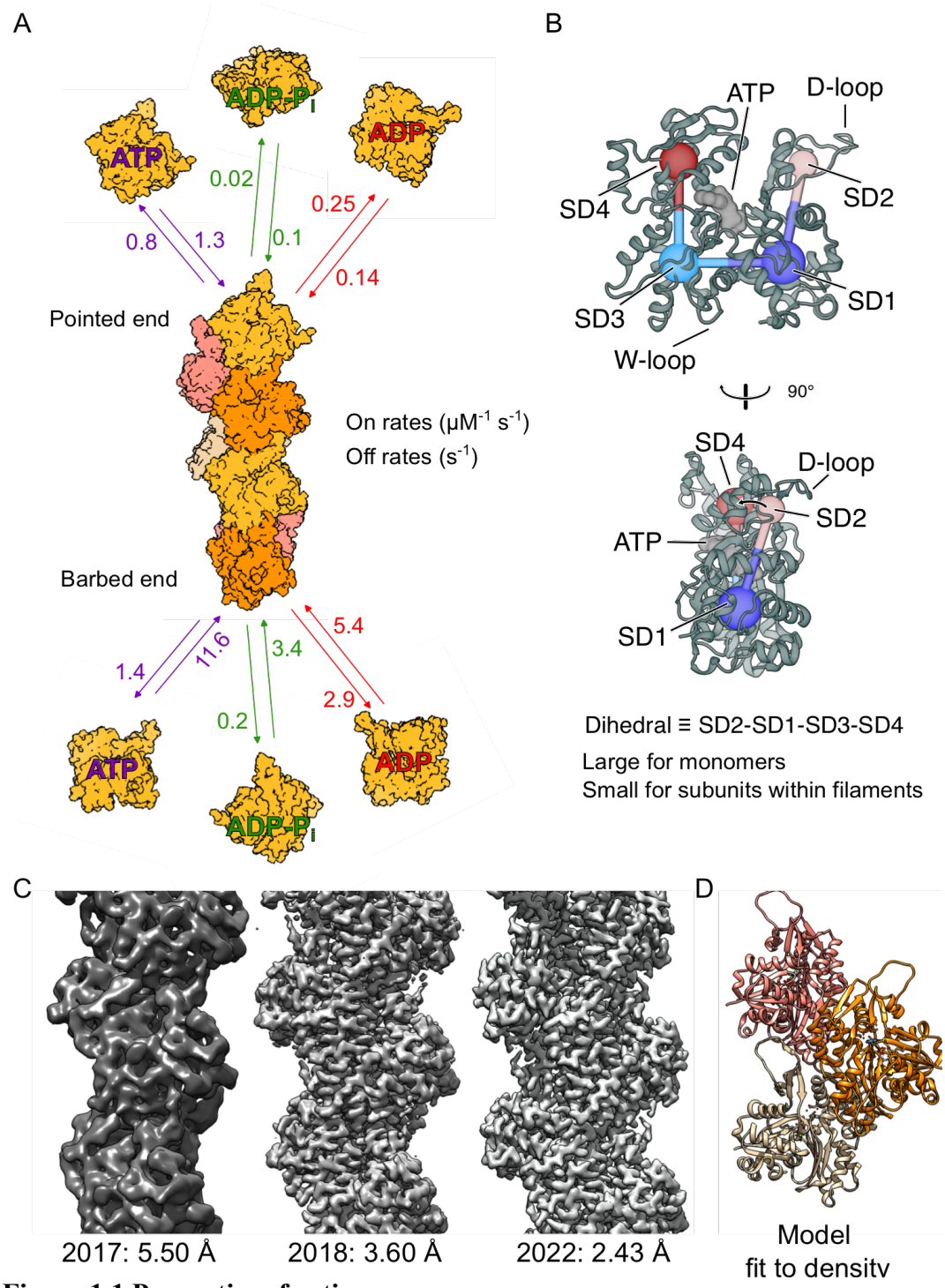

Figure 1.1 Properties of actin.

(A) On and off rates for barbed and pointed end elongation in three nucleotide states of actin. On rates have units of $\mu M^{-1} \bullet s^{-1}$ and off rates have units of s^{-1}. (B) Two orientations of ribbon diagrams of an actin monomer with bound ATP (PDB 1NWK). The four subdomains, W-loop, and D-loop are labeled. (C) Three cryo-EM densities (PDB: 6BNO, 6DJO, 8D13) with year of deposition and resolution labeled. Before 2018, filament structures solved by x-ray fiber diffraction were preferred, such as PDB 2ZWH. (D) Ribbon diagram of actin fit to the 8D13 density.

Many of the properties described above were arrived at through observations made at the level of actin filament bundles or bulk assays containing many filaments (6, 7, 8, 9, 10). Quantification of rate and binding kinetics for each nucleotide state were made by observing the behavior of fluorescently-labeled single filaments (11, 12). However, to get at the underlying mechanisms of what causes each of these properties to emerge at higher length scales, it is very useful to understand what is happening at an even smaller scale. Why does the barbed end have lightning kinetics relative to the sedate pointed end? How does the nucleotide state influence the behavior and interactions of actin molecules? Answers to these questions are critical to understanding how one could modulate the behavior of biological systems, either through drug treatments or mutations, or emulate the behavior in non-biological contexts. Yet answering questions that get at mechanism is tremendously difficult without understanding the structure of the molecules involved– both alone and in complex with each other. Absent a clear picture of the molecular configuration, generating and testing hypotheses pertaining to molecular mechanisms is like trying to assemble furniture in the dark. Sure, you could probably do an okay job with a huge amount of time and effort– but it's going to be a lot easier and lead to a better outcome if you can see what you're working with.

1.3 Actin structures

Much of my PhD work has been enabled by advances in structural biology. In particular, the emergence of high-resolution cryo-EM (cryogenic electron microscopy) has given an entire field of dedicated researchers the tools to resolve protein structures in greater detail than ever before. Over the course of the work presented in this thesis, the cryo-EM structures of molecules in the actin cytoskeleton have become significantly more detailed. If having the first structure of a

protein is like turning the lights on, each improvement in resolution is like putting on better-prescribed glasses. Details you didn't necessarily realize you were missing begin to come into focus. This is illustrated for bare actin filaments in Fig. 1.1C. I hope readers who have not spent years staring at cryo-EM electron density maps can appreciate the successive increases in detail. On the far left is a structure that was reported two months after I started graduate school (13). With a resolution of 5.5 Å, the shape of the protein and the backbone are clear, but most sidechains cannot be resolved. In the middle is a 3.6 Å resolution structure reported the following year (14). In this structure, almost all sidechain orientations are visible. In the past year, two research groups reported actin filament structures with resolutions approaching 2 Å, shown on the right. This level of detail reveals the location of individual water molecules that coordinate with the protein sidechains and bound nucleotide (15, 16).

Powerful insights can arise from comparing the structure of a protein in one environment to the same protein under different conditions. These comparisons give clues that point towards the transition that must have occurred to bring the molecule from one conformation to another. A common example of this would be to compare the structure of a protein by itself to its structure in complex with additional protein molecules. In the case of actin, this reveals an important conformational change. While actin takes on a twisted conformation as a monomer in solution (Fig. 1.1B), it is much flatter when it is in the filament (17, 18). Actin has four major subdomains, which can be used to define a dihedral angle that highlights the flattening transition by tracing a path from the centers of mass of subdomain 2 (SD2) to SD1 to SD3 and then to SD4. This value is low for subunits within filament interiors and larger for actin monomers in solution.

In addition to comparing structures of a protein in complex with other proteins, one can compare the structures of the same protein bound to different ligands. This leads to a somewhat surprising result for actin: The effect of the bound nucleotide on the protein structure of actin

filaments is remarkably subtle (14, 19). The surprise lies in that, although the structures are exceptionally similar, we know from biochemical assays that the nucleotide has a profound effect on the interactions between actin and ABPs, which reshapes the higher-order filament architectures. Given the lack of clear differences in structure, a reasonable hypothesis is that the important difference imparted by the nucleotide's state actually lies in its impact on the dynamics of the actin molecule, not on its average structure.

1.4 Molecular dynamics

Sometimes the relevant structure for understanding a particular molecular mechanism cannot be obtained. Other times, the static structure is only the starting point and protein dynamics will tell much of the story. In these cases, which are myriad, molecular simulation is a powerful, complementary technique to both test and generate hypotheses that refine the field's understanding of the mechanisms governing a biochemical process. The idea behind molecular simulation is that, given an initial configuration of particles, one can compute forces on each particle, propagate their positions a small time in the future using these forces, and repeat. As these steps build, one predicts how the simulated system evolves in time in a way that, if the initial configuration and forces were chosen well, is a meaningfully accurate representation of how the real system behaves.

It is often useful to categorize the type of molecular simulation based on resolution. The resolution of the simulation determines how much detail one can eventually analyze, but also determines how much detail must be computed, which limits how big and how long the simulation can be. Therefore, choosing the model resolution best suited for the question is critically important when setting up a new computational study.

At the highest computational cost, one calculates the forces based on electronic structure on-the-fly using a simulation protocol called *ab initio* molecular dynamics (AIMD) (20). This

provides quantum-level accuracy and allows for the breaking and formation of chemical bonds. However, it is extremely computationally intensive, which typically limits the simulation time hundreds of picoseconds, even for QM/MM (quantum mechanics/molecular mechanics) approaches designed to mitigate speed limitations.

Foregoing quantum mechanical detail, one can achieve much longer simulations for the same computational cost using classical molecular dynamics (MD) simulations. These treat every atom in the system as a classical particle that is then propagated using pre-calibrated atomic force fields, such as the CHARMM force field (21), according to Newton's equations of motion. These simulations retain a great deal of accuracy and allow large (1+ million atoms) systems to achieve durations on the microsecond timescale using modern computing hardware.

For processes involving larger length and time scales, one can develop coarse-grained (CG) models that represent multiple atoms as individual CG beads. The resolution and force fields for these simulations are often tailor-made for the specific scientific question that is being investigated by the CG model. Frequently, CG models come with the additional benefit of representing the solvent implicitly, which can make up a vast majority of the atoms (and therefore computational cost) in an atomistic simulation.

Each of these types of simulations can be combined with enhanced sampling techniques to explore configurations much more efficiently than unbiased simulations through the addition of an external bias potential. Often these biasing methods can be used to estimate the underlying free energy landscape that is being sampled over, which provides additional insight into how molecular systems behave at long timescales.

1.5 Road map

The theme of the work presented here is to investigate important processes of the actin cytoskeleton in the level of detail necessary to draw conclusions about underlying molecular mechanisms. To do this, I have sought out the most appropriate methods for the specific scientific question that I am pursuing. The work is broken up into four chapters, targeting four unique questions. In turn, each utilizes a different technique.

In Chapter 2, I use all-atom MD simulations to investigate the origins of polarized growth of actin filaments. The research strategy uses our collaborators' high-resolution cryo-EM structures of actin filaments as an initial structure for MD simulations. Importantly, the system is set up with the barbed and pointed end subunits exposed to the solvent. As the MD simulation progresses, the actin subunits at the filament ends relax to equilibrium conformations, which differ from the initial conformations of internal subunits. These changes reveal distinct characteristics of each terminal subunit, which can be connected to the kinetic on and off rates at the filament ends in intuitive ways. Additionally, I report differences in the behavior of the barbed and pointed end subunits that result from the state of the bound nucleotide, which lead to natural explanations of the nucleotide-dependence observed in the rate constants (Fig. 1.1A). My findings lead me to make predictions about the conformations of the barbed and pointed end subunits. Excitingly, improved cryo-EM techniques have recently enabled high-resolution structures of the barbed and pointed end to be solved, and these validate my predictions. I highlight this development in Chapter 6.

In Chapter 3, I use steered molecular dynamics (SMD) to explore how actin filaments behave under tension and how this may be sensed by mechanosensitive ABPs. Recent studies have demonstrated that a subset of proteins in the LIM domain family bind to strained actin filaments, and do not bind actin in the absence of applied force. However, the molecular mechanism for this interaction was not understood. I report that filaments under strain do not appear to be

meaningfully different from unstrained actin filaments when all subunits retain connections with each other. Conversely, a discrete conformational change leads to a 'cracked' conformation of the actin filament that presents a unique to filament surface under tension, and mechanosensitive LIM domains bind the cracked interface preferentially in protein-protein docking simulations. This leads to natural explanations for why mechanosensitive LIM domains all share specific sequence features.

In Chapter 4, I use a CG model to explain how the properties of formin, an ABP that nucleates and elongates actin filaments, impact the assembly of the cytokinetic ring. This project successfully bridges the dynamics of single filaments to emergent behavior at the length scale of an entire cell, and interfaces with *in vivo* experiments performed by experimental collaborators. In particular, I implemented formin mechanoinhibition into the model and developed a continuous collective variable to track the formation of the ring over time.

In Chapter 5, I use a microfluidics system to apply strain to formin-bound actin filaments *in vitro* and analyze their elongation rates as a function of force using TIRF (total internal reflection fluorescence) microscopy. In preliminary experiments, I report that the actin filament elongation activity of mammalian formin mDia2 can be accelerated by almost an order of magnitude when subjected to applied tension. I also observe a subpopulation of formin-bound actin filaments that elongate and then completely stop and speculate these may be mechanically inhibited. The difference between the two behaviors likely originates from differences in how the formin molecule is anchored to the coverslip.

In Chapter 6, I report on the progress of two ongoing projects, suggest new research directions based on the findings of each chapter, and provide an outlook on the most interesting open questions in the various fields that my research has interfaced with.

1.6 References

1. Hill, M.A. (2023, April 19) Embryology Movie - Neutrophil chasing bacteria. Retrieved from https://embryology.med.unsw.edu.au/embryology/index.php/Movie_-_Neutrophil_chasing_bacteria

2. Fritz-Laylin, Lillian K et al. "Actin-based protrusions of migrating neutrophils are intrinsically lamellar and facilitate direction changes." eLife vol. 6 e26990. 26 Sep. 2017, doi:10.7554/eLife.26990

3. Pollard, Thomas D, and John A Cooper. "Actin, a central player in cell shape and movement." *Science (New York, N.Y.)* vol. 326,5957 (2009): 1208-12. doi:10.1126/science.1175862

4. R. Dominguez, K. C. Holmes, Actin structure and function. Annu. Rev. Biophys. 40, 169–186 (2011).

5. Pollard, Thomas D. "Regulation of actin filament assembly by Arp2/3 complex and formins." *Annual review of biophysics and biomolecular structure* vol. 36 (2007): 451-77. doi:10.1146/annurev.biophys.35.040405.101936

6. T. D. Pollard, Rate constants for the reactions of ATP- and ADP-actin with the ends of actin filaments. J. Cell Biol. 103, 2747–2754 (1986).

7. T. D. Pollard, M. S. Mooseker, Direct measurement of actin polymerization rate constants by electron microscopy of actin filaments nucleated by isolated microvillus cores. J. Cell Biol. 88, 654–659 (1981).

8. D. T. Woodrum, S. A. Rich, T. D. Pollard, Evidence for biased bidirectional polymerization of actin filaments using heavy meromyosin prepared by an improved method. J. Cell Biol. 67, 231–237 (1975).

9. Tilney, L G. "Actin filaments in the acrosomal reaction of Limulus sperm. Motion generated by alterations in the packing of the filaments." The Journal of cell biology vol. 64,2 (1975): 289-310. doi:10.1083/jcb.64.2.289

10. L. Blanchoin, T. D. Pollard, Hydrolysis of ATP by polymerized actin depends on the bound divalent cation but not profilin. Biochemistry 41, 597–602 (2002).

11. I. Fujiwara, D. Vavylonis, T. D. Pollard, Polymerization kinetics of ADP- and ADP-Pi-actin determined by fluorescence microscopy. Proc. Natl. Acad. Sci. U.S.A. 104, 8827–8832 (2007).

12. Suarez, Cristian et al. "Cofilin tunes the nucleotide state of actin filaments and severs at bare and decorated segment boundaries." Current biology : CB vol. 21,10 (2011): 862-8. doi:10.1016/j.cub.2011.03.064

13. Gurel, Pinar S et al. "Cryo-EM structures reveal specialization at the myosin VI-actin interface and a mechanism of force sensitivity." eLife vol. 6 e31125. 4 Dec. 2017, doi:10.7554/eLife.31125

14. S. Z. Chou, T. D. Pollard, Mechanism of actin polymerization revealed by cryo-EM

structures of actin filaments with three different bound nucleotides. Proc. Natl. Acad. Sci. U.S.A. 116, 4265–4274 (2019).

15. Reynolds, Matthew J et al. “Bending forces and nucleotide state jointly regulate F-actin structure.” Nature vol. 611,7935 (2022): 380-386. doi:10.1038/s41586-022-05366-w

16. Oosterheert, Wout et al. “Structural basis of actin filament assembly and aging.” Nature vol. 611,7935 (2022): 374-379. doi:10.1038/s41586-022-05241-8

17. P. Graceffa, R. Dominguez, Crystal structure of monomeric actin in the ATP state. Structural basis of nucleotide-dependent actin dynamics. J. Biol. Chem. 278, 34172–34180 (2003).

18. T. Oda, M. Iwasa, T. Aihara, Y. Maéda, A. Narita, The nature of the globular- to fibrous-actin transition. Nature 457, 441–445 (2009).

19. Dominguez, Roberto. “Nucleotide-dependent conformational changes in the actin filament: Subtler than expected.” Proceedings of the National Academy of Sciences of the United States of America vol. 116,10 (2019): 3959-3961. doi:10.1073/pnas.1900799116

20. Iftimie, Radu et al. “Ab initio molecular dynamics: concepts, recent developments, and future trends.” Proceedings of the National Academy of Sciences of the United States of America vol. 102,19 (2005): 6654-9. doi:10.1073/pnas.0500193102

21. B. R. Brooks et al., CHARMM: The biomolecular simulation program. J. Comput. Chem. 30, 1545–1614 (2009).

Chapter 2: Structural basis for polarized elongation of actin filaments

Preface

The work presented in this chapter was performed in collaboration with Harshwardhan Katkar, Steven Chou, Thomas Pollard, and Gregory Voth. Harshwardhan Katkar and I built the simulation systems. I performed the simulations and analyzed the data presented in all figures. This work was published in the Proceedings of the National Academy of Sciences in November 2020 (doi: 10.1073/pnas.2011128117).

Abstract

Actin filaments elongate and shorten much faster at their barbed end than their pointed end, but the molecular basis of this difference has not been understood. We use all-atom molecular dynamics simulations to investigate the properties of subunits at both ends of the filament. The terminal subunits tend towards conformations that resemble actin monomers in solution, while contacts with neighboring subunits progressively flatten the conformation of internal subunits. At the barbed end the terminal subunit is loosely tethered by its DNase-1 loop to the third subunit, because its monomer-like conformation precludes stabilizing contacts with the penultimate subunit. The motions of the terminal subunit make the partially flattened penultimate subunit accessible for binding monomers. At the pointed end, unique contacts between the penultimate and terminal subunits are consistent with existing cryo-EM maps, limit binding to incoming

monomers, and flatten the terminal subunit, which likely promotes ATP hydrolysis and rapid phosphate release. These structures explain the distinct polymerization kinetics of the two ends.

Significance Statement

Eukaryotic cells utilize actin filaments to move, change shape, divide, and transport cargo. Decades of experiments have established that actin filaments elongate and shorten significantly faster from one end than the other, but the underlying mechanism for this asymmetry has not been explained. We used molecular dynamics simulations to investigate the structures of the actin filament ends in the ATP, ADP plus γ-phosphate, and ADP nucleotide states. We characterize the structures of actin subunits at both ends of the filament, explain the mechanisms leading to these differences, and connect the divergent structural properties of the two ends to their distinct polymerization rate constants.

2.1 Introduction

Actin is one of the most abundant proteins in eukaryotic cells. By polymerizing into filaments, actin and its associated proteins form polymer networks that drive cell motility, division and morphological change. Critical to these functions, the elongation rate at one end, the 'barbed end', is much faster than the other 'pointed end'. Although this asymmetric growth has been known for decades (1–3), the underlying basis that gives rise to these vastly different kinetic rates has not been understood. The lack of structural data of subunits at the filament ends has limited this understanding.

Monomeric actin may be crystallized, which has allowed the determination of many high-resolution crystal structures of the actin monomer (4–7). Actin filaments have not been crystallized, and so X-ray fiber diffraction (8) and cryo-electron microscopy (9, 10) have been

employed to determine actin filament structures at resolutions up to 3.1 Å. These reconstructions have revealed that the primary conformational change between monomeric and filamentous actin is a flattening of the actin molecule. This flattening can be quantified by measuring the dihedral angle made by actin's four subdomains (Fig. 2.1A), which is around -18° for actin monomers and around -3° for subunits within filaments (Fig. 2.1B). The flattened conformation increases the hydrolysis rate of actin's bound ATP by a factor of 10^4 (11–14).

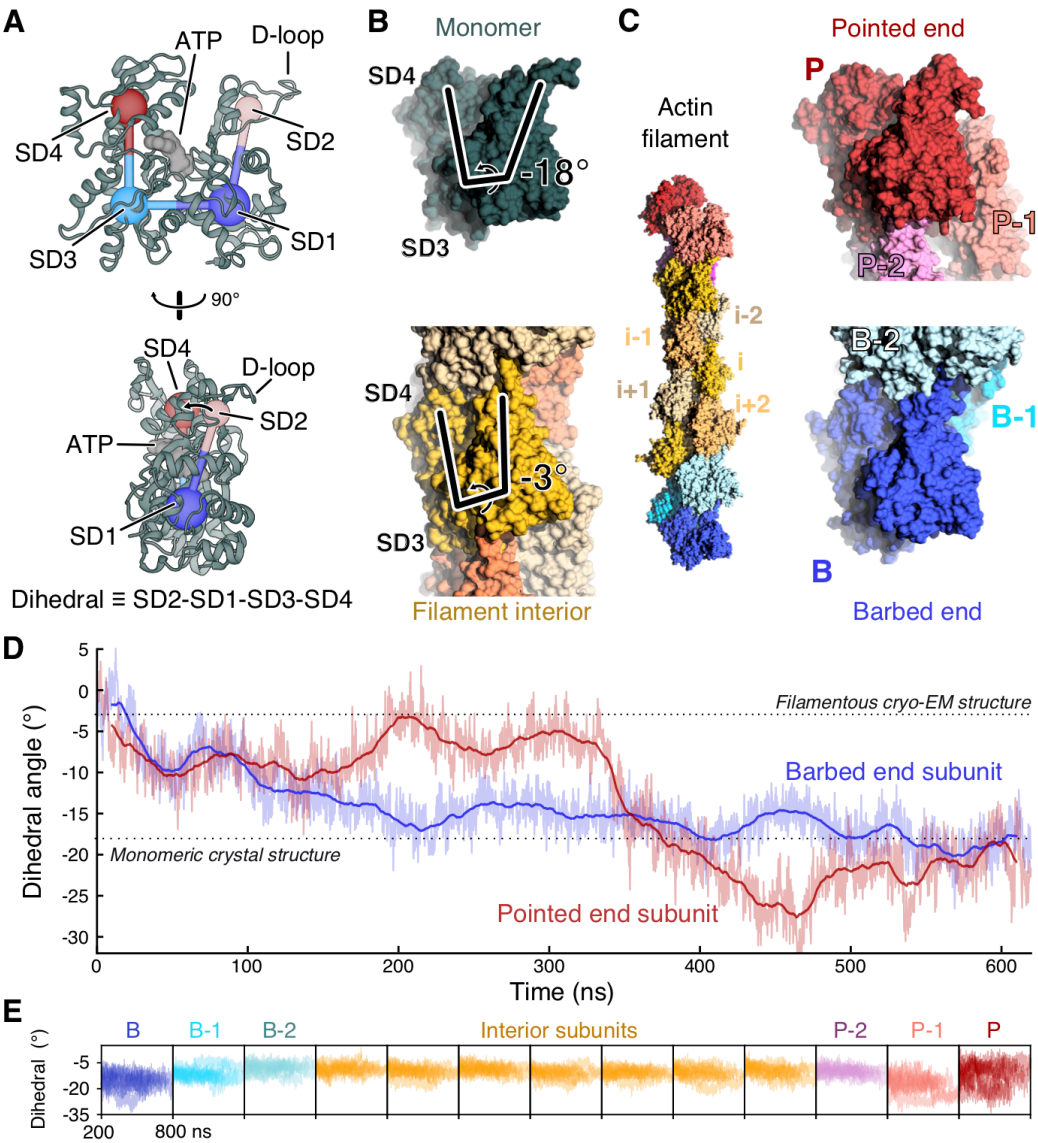

Figure 2.1 The terminal subunits of actin filaments take on monomer-like conformations. (**A**) Two orientations of a ribbon diagram of the ATP-bound actin monomer with labels on the four subdomains, SD1-4. The dihedral angle defined by SD2-SD1-SD3-SD4 characterizes the primary structural transition between monomeric actin and polymerized, filamentous actin. The flexible D-loop in SD2 forms stabilizing contacts between subunits. Protein data bank (PDB) entry 3TU5. (**B**) Side views of space-filling models of monomeric actin (dark green, PDB 3TU5) and a subunit within a filament (yellow, PDB 6JDM). The lines highlight the difference in the dihedral angle between actin monomers (-18°) and a subunit in a filament (-3°). The models are aligned by subdomains 3 and 4. (**C**) Left: Space-filling model from the second half of a 620-ns molecular dynamics simulation of an ATP-actin 13-mer. Note that the terminal subunits at the barbed end (B, blue) and pointed end (P, red) lack two neighboring subunits that form contacts between interior subunits. The penultimate subunits B-1 and P-1 each lack one neighboring subunit. Right: Zoom in on the filament ends showing the terminal subunits B and P in conformations closely resembling monomers. Subunits B and P are aligned relative to each other by subdomains 3 and 4.

Figure 2.1. continued: (**D**) Time course of changes of the dihedral angle of the terminal P and B subunits during a 620-ns simulation of the ATP-actin filament, in which all subunits started in the conformation of interior subunits (PDB 6DJM). During the simulation, both terminal subunits transitioned spontaneously from the filamentous conformation toward the monomer conformation. Raw data (light) and 20-ns moving average (dark) are shown. Data and snapshots are from simulation 3 (Table 2.1). (**E**) Time courses of the dihedral angles of each subunit in the 13-mer actin filaments for times greater than 200 ns. Nine runs are shown (simulations 1-9 (Table 2.1)). Subunits at the filament ends sample a wider range of conformations than the flattened internal subunits (yellow).

Acquiring structures of subunits at the filament ends is a much greater challenge. As of this study, only the structure of the pointed end has been solved at a resolution of 22.9 Å (15). In the absence of structural data, it has largely been assumed that subunits at the filament ends adopt the flattened conformation of interior subunits.

Here we use all-atom molecular dynamics (MD) simulations of an actin filament to investigate the equilibrium conformations of subunits at the filament ends. Specifically, we constructed actin 13-mers from structures of interior subunits for each of the ATP, ADP-P_i, and ADP nucleotide states (Fig. 2.1C, left). Our simulations show that the barbed end and pointed end subunits adopt distinct equilibrium conformations, which lead to meaningful differences in the contacts between neighboring subunits. These distinct structural properties lead to natural explanations for the observed differences in actin elongation kinetics of the two filament ends.

2.2 Results

Subunits at filament ends transition to monomer-like conformations. In all-atom MD simulations of actin filaments, subunits at both ends spontaneously transitioned from the flattened conformation found in the middle of filaments to conformations with larger negative dihedral angles that resemble free actin monomers (Fig. 2.1, C and D). The relaxation to a large dihedral

angle was generally less pronounced for subunits further from the ends (Fig. 2.1E), suggesting that the transition to the flattened conformation does not occur discretely when a subunit incorporates into the filament, but rather, occurs as contacts formed by addition of new monomers facilitate a gradual transition from the monomeric conformation to the structure of interior subunits.

ATP Barbed End. A major consequence of monomer-like conformations of barbed end subunits is that a monomeric subunit cannot make the full set of contacts that connect subunits i and i-1 in the interior of the filament. This is due to the fact that subdomain 2 and subdomain 4 of subunit i must be roughly planar (i.e., subunit i must be flat) to make contacts with subunits i-1 and i-2 simultaneously. At the ATP-bound barbed end, subunit B takes on a monomeric conformation (Fig. 2.2A, top), and therefore cannot make one or more contacts with subunits B-1 or B-2.

In keeping with the transition of subunit B to a large dihedral angle, subunit B lost its contacts with subunit B-1, and the distance between subdomain 4 of subunit B and subdomains 1 and 3 of subunit B-1 increased from ~26 to ~37 Å (Fig. 2.2A). The loss of contacts between them (Fig. 2.3) led to pronounced dynamics of subunit B, which only maintained stabilizing attachments to subunit B-2 through its D-loop in subdomain 2 (Fig. 2.2B).

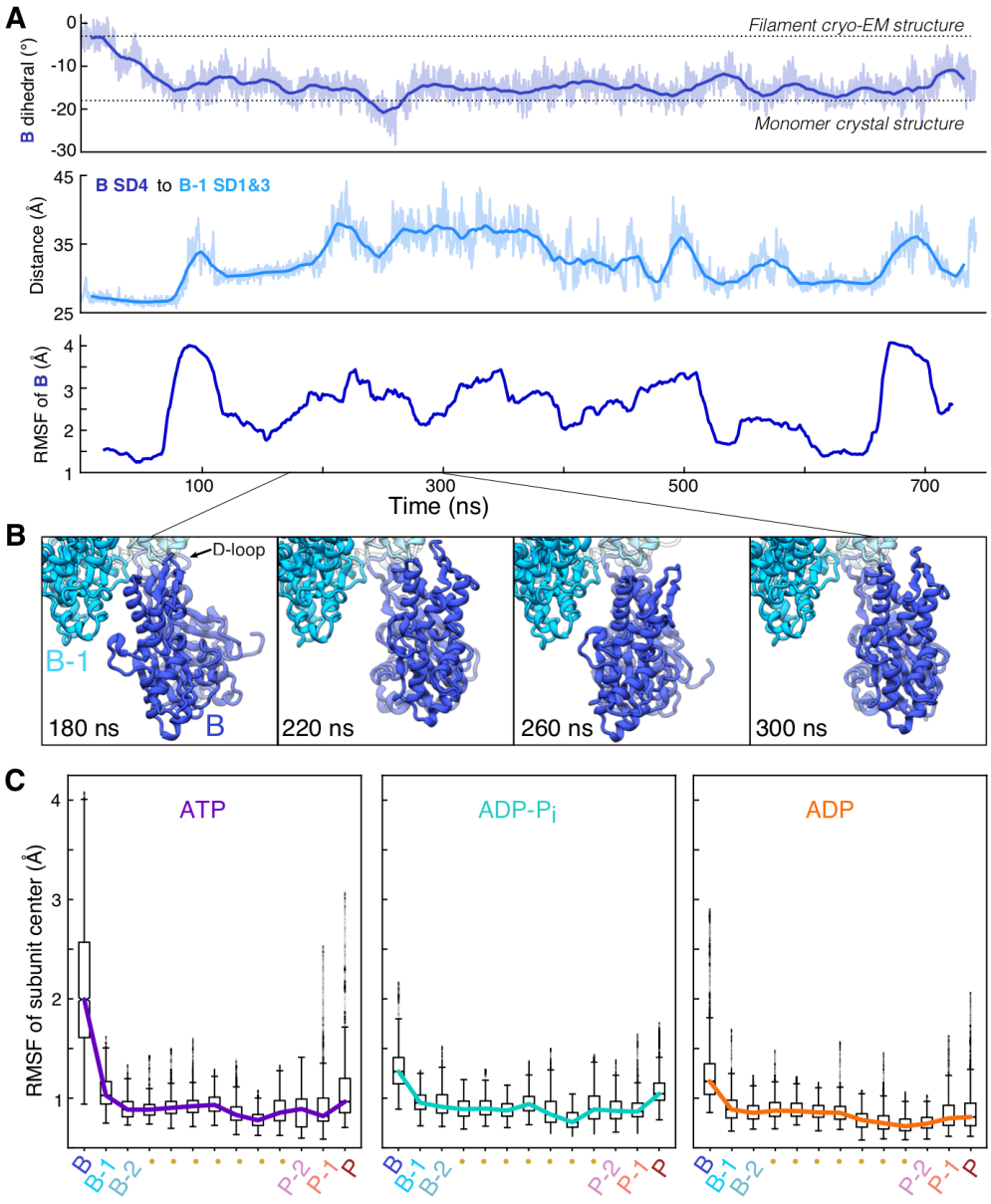

Figure 2.2. The transition of the ATP barbed end subunit to a monomeric dihedral angle is associated with loss of lateral subunit contacts, while remaining tethered to the barbed end by its D-loop.

(**A**) Time course of changes during a 742-ns MD simulation of an ATP-actin filament. The top and middle figures show raw data (light) and 20-ns moving averages (dark). Top: The dihedral angle of barbed end subunit B spontaneously increases as the subunit transitions to a monomeric conformation. Middle: The distance between centers of mass of subdomain 4 of subunit B and subdomains 1 and 2 of subunit B-1 increase as subunit B transitions to a monomer-like structure. Bottom: The root-mean-square fluctuation (RMSF in 40-ns windows) center of mass of subunit B increases in step with the transition to a monomer-like conformation and the loss of inter-subunit contacts. (**B**) Ribbon diagrams of the terminal subunit B at 40-ns intervals showing movements around the tether formed by the D-loop of subunit B stably bound to subunit B-2. Data are from simulation 1.

Figure 2.2. continued: (**C**) Boxplots of the center of mass RMSF for each subunit in the 13-mer reveal gradients of fluctuations from both ends the filament. Barbed end subunits with bound ATP fluctuate the most and those with ADP fluctuate the least. Data comes from times greater than 200 ns in simulations 1-3 for ATP, simulations 4-6 for ADP-Pi, and simulations 7-9 for ADP (Table 2.1).

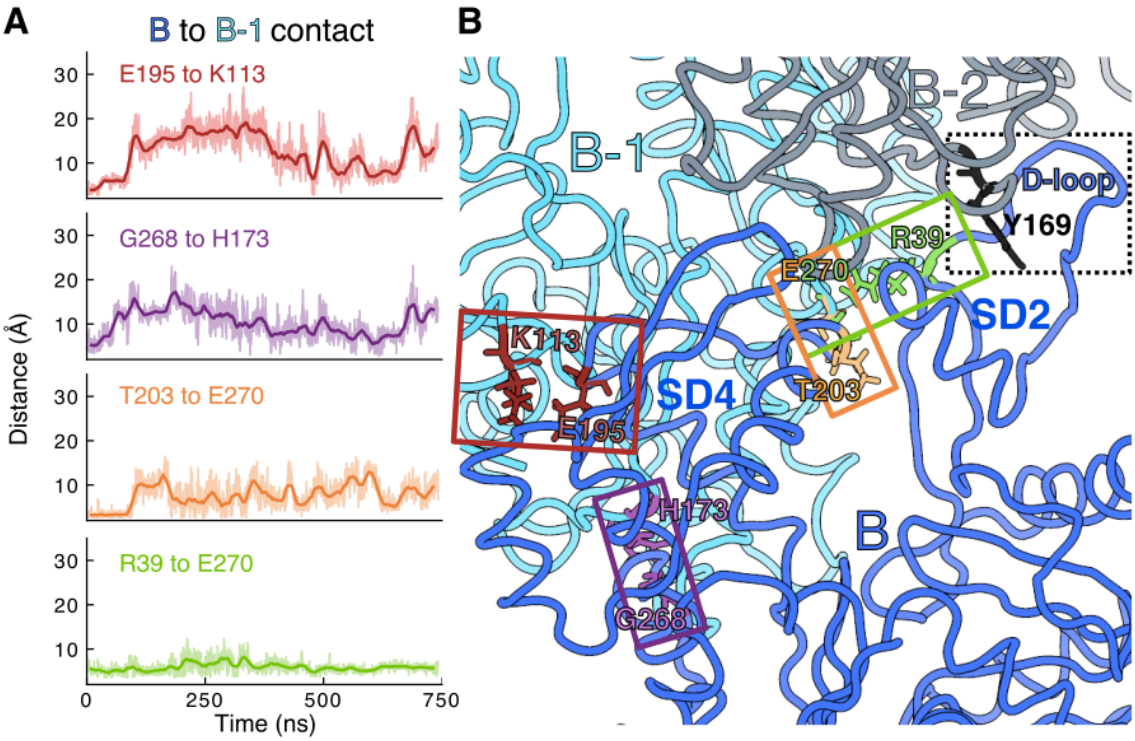

Figure 2.3. Lateral contacts between subdomain 4 of interior subunit i and subunit i-1 are broken between barbed end subunits B and B-1 in simulations of ATP and ADP-P_i filaments.
(**A**) The distance between the backbone O of E195 of subunit B and the backbone N of K113 of subunit B-1 increased significantly (top, red), while the distance between the terminal sidechain carbons of R39 of subunit B and of E270 of subunit B-1 increased very little (bottom, green). The distance between the backbone O of G268 of subunit B and sidechain nitrogen NE2 of H173 of subunit B-1 (purple), as well as the distance between the backbone N of T203 of subunit B and the sidechain O (OE2) of E270 of subunit B-1 (orange) both also increased to the point of no longer mediating a stabilizing inter-subunit connection. Contact partially reform around 600 ns before being lost again. Data comes from simulation 1 (Table 2.1). (**B**) The contacts that break are located in subdomain 4 of subunit B (labeled SD4), whereas those that connect subdomain 2 of subunit B to subunit B-1 are preserved. This is because the D-loop of subunit B maintains a highly stable attachment to Y169 of subunit B-2 (dashed box), which steadies all of subdomain 2. Subunits B (blue), B-1 (cyan), and B-2 (gray) are depicted in ribbon representation, whereas specific contacts are depicted in licorice representation and contact pairings are colored according to the corresponding time course shown in panel A.

Calculations of the root-mean-square fluctuation (RMSF) of subunit B's center of mass relative to neighboring subunits B-1 and B-2 (see Methods) revealed a large and sustained increase in the motion of subunit B following the loss of lateral contact with B-1 (Fig. 2.2A, bottom). Despite these fluctuations, the D-loop of B remained securely associated with B-2 throughout the entirety of the simulations, and complete dissociation of subunit B from the filament appeared unlikely on the simulation timescale. Fluctuations of the barbed end subunit were consistently higher than elsewhere in the filament.

The nucleotide bound to the barbed end subunit influenced its dynamic fluctuations (Fig. 2.2C). The ATP-bound barbed end subunit fluctuated most, with a RMSF interquartile range (IQR) spanning 1.6 to 2.6 Å. In contrast, the ADP-bound barbed end subunit was least dynamic with an IQR spanning 1.0 to 1.3 Å. Subunit B in this nucleotide state fluctuated less because it relaxed to a lesser dihedral angle (~-13°), allowing it to maintain its lateral contacts with subunit B-1. The RMSF of subunit B in the ADP-P_i state had an intermediate IQR spanning 1.1 Å to 1.4 Å, which resulted from generally weakened lateral contacts. However, these associations were not so weak that full separation between subunits B and B-1 occurred consistently, as in simulations of ATP-bound filaments.

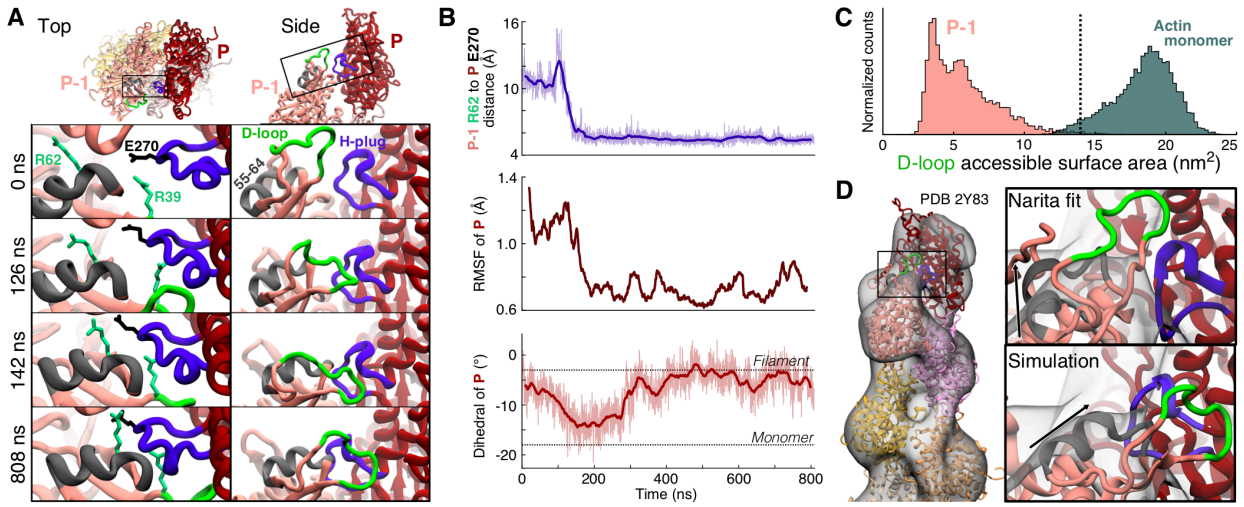

Figure 2.4. Transition of the ADP pointed end subunit P-1 to a monomeric dihedral angle gives rise to stabilizing contacts with subunit P that flatten P and sequester the D-loop of P-1.

(**A**) Ribbon diagrams from two views of the pointed end of an ADP-actin filament showing unique contacts formed during MD simulations between subdomain 2 of subunit P-1 and subdomains 3-4 of subunit P. The four panels in each column show selected time points. Left: looking down the filament axis at the pointed end, R39 and R62 of subunit P-1 (foam green) contact the hydrophobic plug (violet) of subunit P (E270 shown in black). These long-lasting interactions stabilize a shift in the position of a helix composed of residues 55-64 (gray) of subunit P-1. Right: a side view depicts the progressive shift of subdomain 2 of P-1 toward subunit P resulting in the D-loop of subunit P-1 (green) forming a stable, lateral contact with subunit P. (**B**) Time course of the formation of the connection between subunits P and P-1 that stabilizes and flattens the pointed end. Raw data (light) and 20-ns moving averages (dark) are shown. Top: Distance between the C_α atoms of R62 of subunit P-1 and E270 in the H-plug of subunit P. Middle: The 40-ns RMSF of subunit P's center of mass drops in step with the formation of contacts with P-1. Bottom: The dihedral angle of subunit P transitions toward the monomer conformation, then back to flattened structure after forming contacts with P-1 (**C**) Histograms of the accessible surface areas at a radius of 7 Å around the D-loops of subunit P-1 and actin monomers. The dotted line marks the value assuming P-1 takes on the flattened conformation of interior subunits (PDB 6DJO). Data and snapshots are from simulations 7-9 for P-1 and simulations 10-12 for the actin monomers (Table 2.1). (**D**) Comparison of pointed end models with the 3D reconstruction of the ADP-actin pointed end by Narita et al (2011). Left: Narita model. Right: Enlargement of the bridge-like density connecting P-1 and P in the model. Our simulated ADP structure (bottom) places the structured alpha-helix of subunit P-1 (black arrow) and H-plug of P within the bridge density with the D-loop stably attached to subunit P.

ADP Pointed End. The tendency for terminal subunits to take on monomer-like conformations led to changes at the pointed end (Fig. 2.4) almost opposite to those at the barbed end. In simulations of ADP-actin filaments, the penultimate pointed end subunit, P-1, which lacks

an i-2 neighbor to secure its subdomain 2, initially sampled a broad range of dihedral angles. Wide dihedral angles brought residues in subdomain 2 of subunit P-1 close to subunit P, the terminal subunit at the pointed end. These contacts allowed attractive interactions to form between the neighboring subunits P and P-1. Of the interacting residues, the most important contacts were established by the sidechain of R39 of subunit P-1, which formed a hydrogen-bond network with oxygens of several nearby residues (Fig. 2.5). Additionally, a strong interaction formed between the sidechains of R62 of subunit P-1 and E270 of subunit P in two of the four ADP-filament simulations (Fig. 2.4A, left). As a result, subdomain 2 of P-1, including the structured helix composed of residues 55-64, shifted towards subunit P and was secured in a monomer-like conformation (Figs. 2.4A and 2.5). Furthermore, the D-loop of P-1 formed a long-lasting association with subunit P (Fig. 2.4A, right), although the specific residue-residue contacts varied over time.

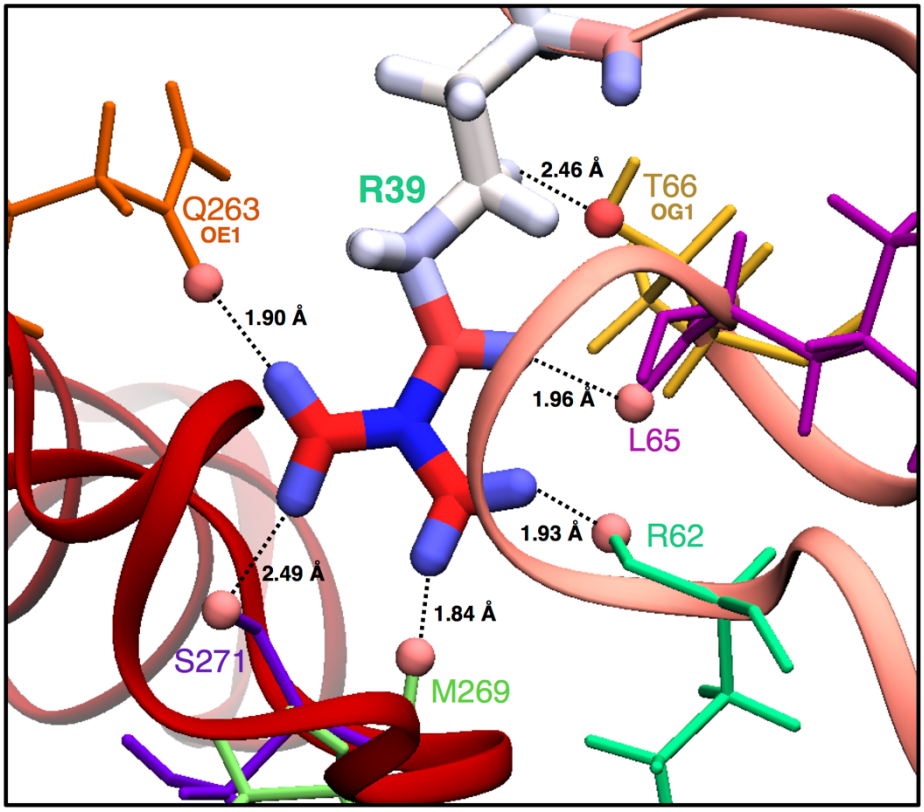

Figure 2.5. A hydrogen-bond network stabilizes R39 of subunit P-1 with oxygens of nearby residues in the connection between subunit P-1 and subunit P.
R39 of subunit P-1 is depicted in licorice representation with atoms colored by charge (blue is positive; red is negative). Subunits P-1 and P are shown as pink and red ribbons, respectively. Atoms within 2.5 Å of R39 of P-1 are shown as spheres and colored by charge; dotted lines depict the distance to atoms of R39. All atoms within the cutoff are backbone oxygens unless labeled, in which case they are sidechain oxygens. The entire residue containing the nearby oxygen atoms is depicted in a thin licorice representation colored by amino acid species. This snapshot is from the last frame of simulation 7 (Table 2.1)—in other frames, the backbone oxygens of G63 of subunit P-1 and E270 of subunit P participated in the hydrogen-bond network.

The fluctuations of subunit P decreased significantly after this new association with subunit P-1 (Fig. 2.4B) and generally remained as low as the fluctuations of interior subunits (~0.9 Å) (Fig. 2.2C) in spite of lacking two neighboring subunits, i-1 and i-2. Consequently, the pointed end subunits were very rigid with respect to each other in the ADP-state, in contrast to the loosely-attached and flexible ATP-bound barbed end. In addition, the formation of contact with P-1

reversed the transition of subunit P to the monomeric conformation (Fig. 2.4B, bottom), supporting the concept that monomeric conformations of terminal subunits arise from a lack of contact with neighboring subunits (Fig. 2.6).

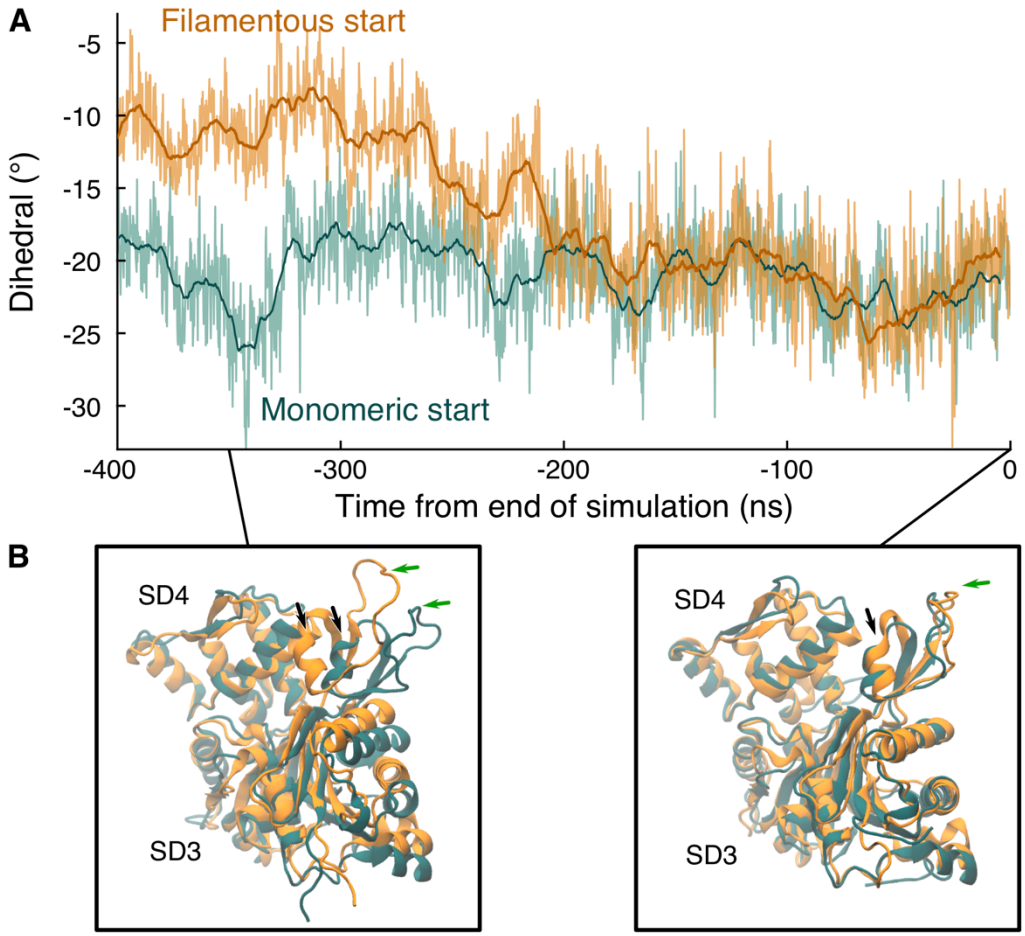

Figure 2.6. Monomers in the flattened conformation relax to a large dihedral angle. (A) Time courses of the dihedral angle of two simulations of ATP-actin monomers initialized in either a filamentous (orange) or monomeric (dark green) conformation. Raw data (light) and 10-ns moving averages (dark) are shown. The time courses are aligned to the final frame of both simulations. Regardless of the starting conformation, both simulations converge to the large dihedral angle conformation, as evidenced by the overlap in the last ~200 ns of simulation. (B) Ribbon diagrams depict the monomers at two time points. Subdomains 3 and 4 were aligned in the two structures. The orientations of alpha-helix number 1 (black arrows) and the D-loop (green arrows) of subdomain 2 differed early in the simulations (left) but aligned later in the simulation (right) owing to both assuming monomeric dihedral angles. Data and snapshots are from the final 400 ns of simulations 12 and 13 (Table 2.1).

A further consequence of the interaction between subunits P-1 and P is that the D-loop of P-1 is far less available to form other protein-protein interactions—namely, bind the barbed end of a nearby free actin monomer—due to its close association with subunit P. To quantify this effect, we calculated the accessible surface area (ASA) around the D-loop at a probe radius of 7 Å (Fig. 2.4C). Throughout the simulation, the D-loop of P-1 was greatly occluded, with the most common ASA being ~4 nm^2. For comparison, the ASA assuming subunit P-1 were in the conformation of an interior subunit is ~14 nm^2 (Fig. 2.4C dotted line, PDB 6DJO). More consequential for polymerization rate kinetics, however, is the comparison with the D-loop of a free actin monomer. At the barbed end of the filament, it is the monomer's D-loop that participates in the connection with subunit B-1. Strikingly, the accessibility of the monomer's D-loop is nearly five times that of subunit P-1, with a most likely ASA of ~19 nm^2. Furthermore, the two distributions hardly overlap (<2% intersection). This disparity implies that the stabilizing D-loop contact between a free monomer and a filament end forms much more readily at the barbed end than at the pointed end. Additionally, it is likely that the D-loop of subunit P-1 must lose its association with subunit P in order for an actin monomer to become fully incorporated at the pointed end.

The connections between subunits P and P-1 formed readily (within 250 ns) in all four ADP simulations, including one which was initialized with the D-loops in helical conformations, but did not form as readily in the ATP and ADP-P_i simulations. For instance, in one simulation of the ADP-P_i filament, the connection observed between subunits P and P-1 in ADP-filaments emerged after ~580 ns and remained thereafter. In the other two ADP-P_i- and all three ATP-filament replicates, the connection did not form in simulations as long as 742 ns. However, subunit P-1 generally assumed large dihedral angles (Fig. 2.6B), which was a precursor for this connection to form in the other simulations. Therefore, we propose that the contacts connecting subunit P-1

to subunit P described above are likely to occur in the ADP and ADP-P_i states, but are less probable in the ATP state, though likely not forbidden. It should be noted that because phosphate dissociates rapidly from pointed end subunits (16), ATP and ADP-P_i will occupy pointed end subunits only transiently, favoring the interactions between subunits P and P-1.

The stable connection that forms at the pointed end between subdomain 2 of subunit P-1 and subdomains 3 and 4 of subunit P in our simulations bears striking resemblance to electron potential maps of the pointed end of ADP-bound filaments (15). Although the resolution was limited to 22.9 Å, that reconstruction revealed a bridge-like density connecting subunit P-1 to subunit P. The authors proposed a model whereby the D-loop of subunit P-1 and the hydrophobic plug of subunit P partially occupy the bridge density by forming lateral contact. However, in their proposed fit, P-1 is mostly in the conformation of a flattened subunit, and so the alpha-helix of subdomain 2 does not match the bridge density well (Fig. 2.4D, right). In contrast, the connection between subunits P and P-1 that emerged in our MD simulations forms after a significant shift of subdomain 2 of P-1 towards subunit P. Because of this shift, the conformation emerging from our simulations fits better into the bridge density (Fig. 2.4D, right). Additionally, terminal subunit P in the electron potential map appears to be flattened, in agreement with our simulations of the ADP-pointed end.

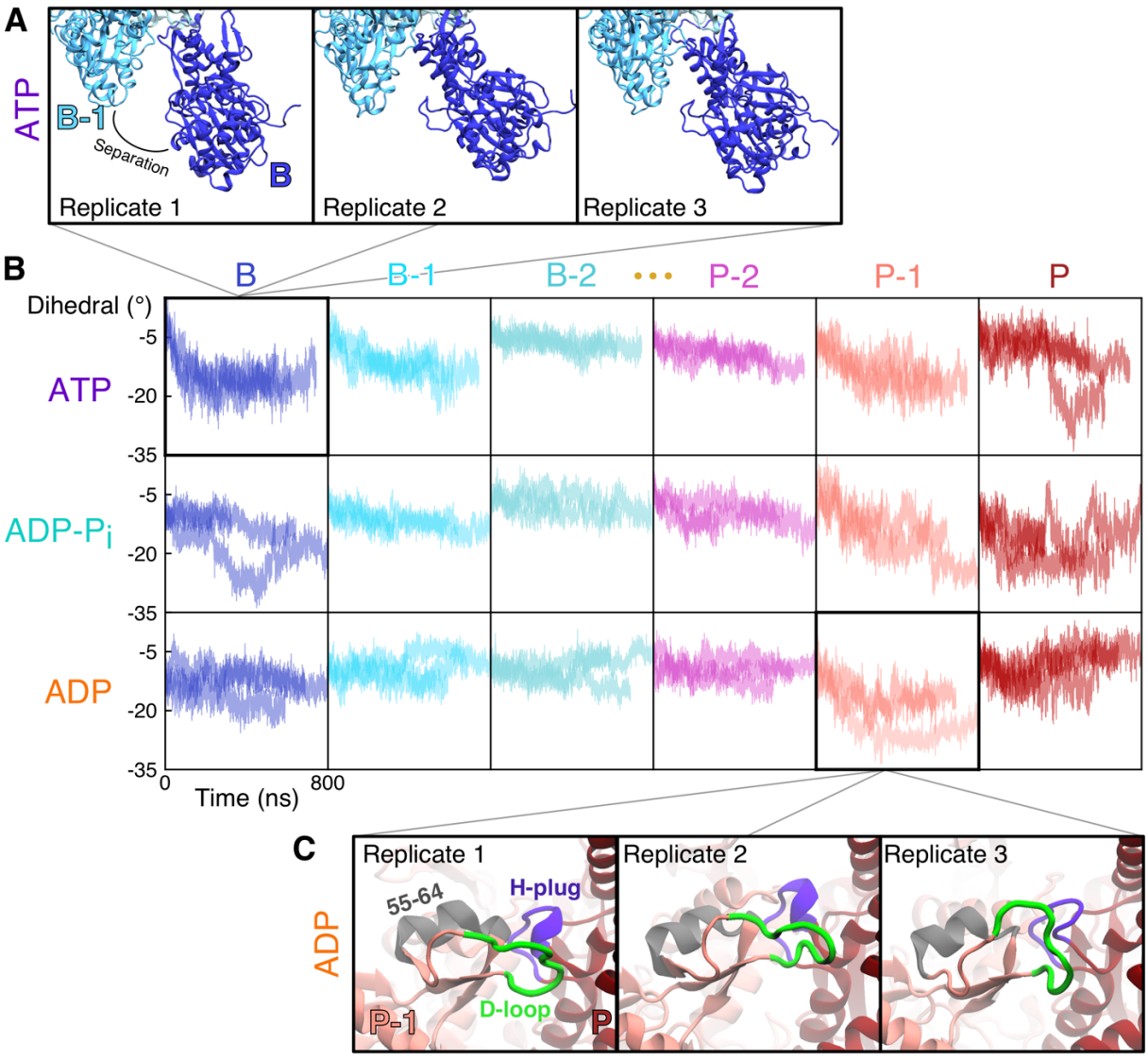

Figure 2.6. Comparison between replicates.
(A) Ribbon diagrams depict the separation between barbed end subunits B (blue) and B-1 (cyan) in each of the three ATP-filament MD simulation replicates. Snapshots come from simulations 1-3. (B) Time courses of the dihedral angles of the terminal subunits B, B-1, B-2, P-2, P-1, and P are shown for each nucleotide state. Three replicates are shown in each nucleotide state: simulations 1-3 for ATP, simulations 4-6 for ADP-Pi, and simulations 7-9 for ADP (Table 2.1). (C) Ribbon diagrams of the pointed ends of filaments from three ADP-actin filament MD simulations depicting the unique contacts formed between subdomain 2 of subunit P-1 and subdomains 3-4 of subunit P. Snapshots from simulations 7-9 show contacts between the hydrophobic plug (violet) of subunit P and the alpha helix composed of residues 55-64 (gray) of subunit P-1, as well as between the D-loop of subunit P-1 (green) and residues of subunit P.

2.3 Discussion

We find the mechanism that underlies the distinct structures at the two ends of actin filaments is in fact the same: subunits with limited contacts with neighboring subunits are free to adopt the conformation of monomers with large dihedral angles (Fig. 2.6). Monomeric actin without neighboring subunits has a dihedral angle of ~-18°, whereas interior subunits within filaments with four neighboring subunits assume a flat dihedral angle around -3°. Therefore, terminal subunits, which lack one or two neighbors, may take on intermediate dihedral angles (Figs. 2.1E and 2.7). The tendency for terminal subunits to assume large dihedral angles leads to unique structures at the two filament ends, which explain their different elongation kinetics, as detailed below.

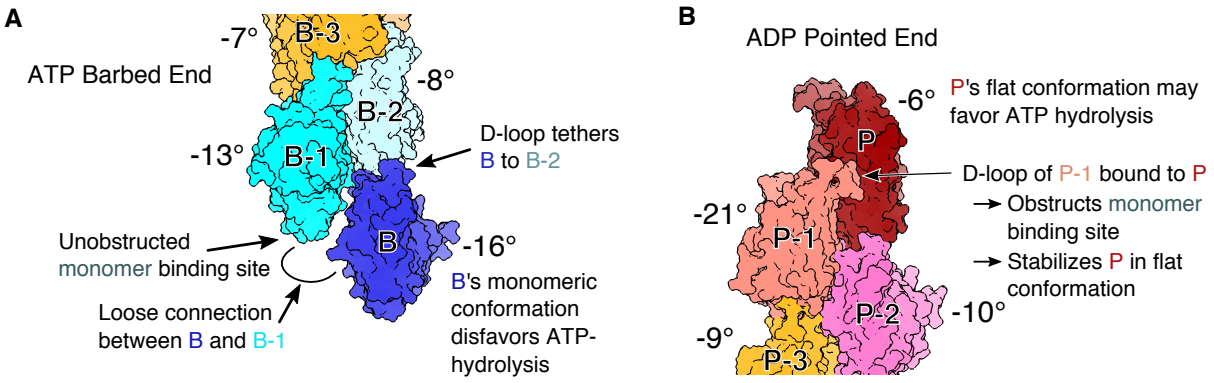

Figure 2.7. Structural basis for polarized actin filament elongation kinetics.
Space-filling models of subunits at the ATP barbed end and ADP pointed end. Median dihedral angles are shown next to each subunit. (**A**) Subunits incorporated at the barbed end are progressively flattened as they make contacts with newly polymerized subunits, so ATP hydrolysis is more likely in interior subunits. Subunit B's monomeric conformation hinders stable contact with subunit B-1, leaving the D-loop of subunit B tethered to subunit B-2 and the monomer-binding site on subunit B-1 unobstructed. (**B**) Unique contacts formed between subdomain 2 of subunit P-1 and subunit P greatly limit interactions of the D-loop of P-1 with monomers and stabilize subunit P in a flattened conformation that may favor hydrolysis of the bound ATP.of subunit P.

Our simulations show that flattening generally progresses as subunits acquire neighbors at the barbed end (Fig. 2.7A). This progression to a flat conformation appears to be gradual and cooperative. Each additional lateral contact further stabilizes the flat conformation and strengthens connections along the short-pitch helix, as predicted from reconstructions of interior subunits (10). Pointed end subunits P and P-1 are different. The monomeric conformation of subunit P-1 facilitates the formation of a unique lateral contact with subunit P, which is linked to flattening of this terminal subunit in spite of having only two neighbors (Fig. 2.4B and 2.7B). The lateral contact between subunits P and P-1 is not observed elsewhere in filaments but stabilizes the unique conformation of pointed ends originally observed by Narita et al. (15).

Nucleotide states of terminal subunits. Flattening actin subunits increases ATP-hydrolysis 10^4-fold (11–14), so the progressive flattening of terminal subunits must influence the nucleotide state of subunits at both filament ends. Our simulations suggest that ATP-hydrolysis is delayed at the barbed end until subunits have been flattened by contacts with four neighbors (i.e., position B-2 and deeper in the filament). Thus, the terminal barbed end subunits likely have bound ATP.

At the pointed end, the unique lateral contact made by penultimate subunit P-1 flattens terminal subunit P (Fig. 2.4B, bottom), which should favor ATP hydrolysis. If subunit addition is slow, this temporary flattening may result in the hydrolysis of ATP bound to most new subunits added to the pointed end. For example, at steady state with about 0.1 μM free ATP-actin monomers, the association rate is ~0.1 subunit per second and the hydrolysis rate within the filament is 0.3 s^{-1}. In simulations of ADP and ADP-Pi filaments, the R177 gate on the phosphate release channel (10) is mostly open on subunit P and opens for subunit P-1 in step with the formation of the contact between subunits P and P-1. Open gates on these two subunits may explain

why phosphate dissociates rapidly at the pointed end compared with the barbed end and interior subunits (16). Rapid dissociation of phosphate from subunit P-1 would favor formation of the contact with subunit P.

These features suggest a cooperative mechanism for ATP hydrolysis and phosphate dissociation by pointed end subunits. Specifically, assuming newly incorporated subunit P arrives with bound ATP, having ADP bound to subunit P-1 makes more likely the formation of the lateral connection and flattening of subunit P, favoring the hydrolysis of its bound ATP. On the other hand, with high concentrations of ATP-actin monomers, subunit addition would exceed the rate of ATP hydrolysis on subunit P, so subunit P-1 would also have bound ATP, reducing the chance that it would form the connection with subunit P, leaving P in its monomeric conformation and less likely to hydrolyze its bound ATP until it is deeper in the filament.

A kinetic analysis of elongation at the pointed end (16) found that the high critical concentration of the pointed end can be explained by a smaller rate constant for adding an ATP-actin monomer to an ADP-actin pointed end than an ATP-actin pointed end. The cooperative mechanism described above is consistent with a higher critical concentration for ATP-actin at the pointed end.

Elongation at barbed ends. Elongation at barbed ends is a diffusion-limited reaction with a high probability that random collisions with incoming subunits result in binding (17). The dependence of the elongation rate on the solution viscosity demonstrated that the reaction is diffusion limited, and the calculated collision rate constant is only 50 times higher than the observed rate constant, giving a very high orientation factor (probability of binding) of 0.02 in the Smoluchowski equation. The high degree of freedom of barbed end subunits revealed by our simulations may contribute to making these reactions highly favorable in three ways.

First, monomer binding to subunit B-1 is likely enhanced by the separation of subunit B from subunit B-1 (Fig. 2.6A), which opens up the initial binding site for the D-loop on subunit B-1 (Fig. 2.7A). This mobility of subunit B results from its monomeric conformation, which precludes stable lateral contacts with B-1. As a result, subunit B is only attached to the filament through association of its D-loop with subunit B-2. Despite this single attachment point, the large buried surface area of the D-loop connection (10) tethers terminal subunit B to the filament end throughout energetic fluctuations. Thus, the D-loop association alone suffices to bind an incoming subunit B+1 to the barbed end. Additionally, the nucleotide state impacted the affinity of subunit B for subunit B-1, with the barbed ends in the ADP and ADP-P_i states fluctuating the least, and the ATP state fluctuating the most (Fig. 2.2C). Thus, hydrolysis of ATP on the terminal subunits might impact the barbed end elongation rate at very low concentrations of ATP-actin monomers where elongation is slow enough to allow for ATP hydrolysis.

Second, partial flattening of subunit B-1 may favor binding of the D-loop of an incoming actin monomer. Flattening of interior subunits opens a hydrophobic pocket for binding M44 from the D-loop of the next subunit along the long-pitch helix (10). In our simulations, this pocket on subunit B-1 was generally closed even though the subunit relaxed to an intermediate dihedral angle around -12°. However, subunit B-1 spent ~13% of the time with dihedral angles flatter than -6°, which may favor transient opening of the pocket for M44.

Third, the simulations also show that tethered subunit B spontaneously forms lateral associations with subunit B-1. For example, the longest ATP-filament simulation revealed that after losing the starting contacts between subunits B and B-1, subunit B transiently visited a state that reestablished some of the contacts with subunit B-1 ~500 ns later. These contacts lasted ~50 ns before dissociating again (Fig. 2.3). It is reasonable to believe that this state would be visited periodically in a longer simulation. If this were true, then every half microsecond or so the tethered

subunit B will spontaneously approach a state where lateral contacts with subunit B-1 form easily. Therefore, when incoming subunit B+1 makes contact with B-1, subunit B is poised to quickly establish lateral contact with B-1 and participate in the next polymerization reaction (i.e., accept contact from subunit B+2).

Although the separation between subunits B and B-1 could limit addition of subunit B+1 at rates faster than the reversible association of subunit B with B-1, their rejoining occurs on a time scale of ~2 μs^{-1}. Therefore, subunit addition would have to exceed ~2 million subunits per second before this step limits the rate of elongation. Because 2 million subunits per second exceeds any rate than can be reasonably achieved either *in vivo* or *in vitro* (corresponding to an actin monomer concentration of ~0.2 M), our results are consistent with diffusion-limited barbed end elongation.

Elongation at pointed ends. At the pointed end, elongation is slow and not diffusion-limited (17). Our simulations show that the monomeric conformation of subunit P-1 allows its D-loop to attach to subunit P (Fig. 2.4A), which reduces the probability that the D-loop can bind an incoming monomer. It is likely that this association is essential for an incoming subunit to be incorporated as P+1, because the D-loop connection appears to be the strongest stabilizing contact between subunits at the barbed end (Fig. 2.2B) and in the filament interior (10). Therefore, unbinding of the D-loop of subunit P-1 from subunit P is a pointed-end-specific step that limits the rate of elongation, as predicted by Narita et al. (15). Compromising the reaction further, the pointed end connection formed most readily in the ADP-nucleotide state, which is also the most probable nucleotide state for subunits P and P-1 given that phosphate dissociates rapidly from pointed end subunits (16) and P is flattened by subunit P-1 (Fig. 2.4B). Additionally, the barbed end of the free monomer does not have a favorable conformation to bind the D-loop of subunit P-1, which could also limit pointed end elongation.

Methodological considerations. All atomistic MD studies are limited to finite timescales, generally in the hundreds of nanoseconds to microsecond range, so we cannot rule out that other properties would emerge in longer simulations. In particular, we began the simulations with all subunits in the conformations of interior subunits. If this initial structure were to be very far from the true equilibrium conformations of the ends, then reaching the preferred orientations may not presently be possible in all-atom MD simulation. However, the close match to existing structural data of the pointed end (15) suggests that our all-atom approach adequately sampled conformational space in order to reach equilibrium distributions. Furthermore, recent coarse-grained Monte Carlo simulations of an actin monomer associating with an actin dimer reported high-probability barbed end conformations similar to ones sampled in our all-atom simulations (18).

New mechanisms for actin binding proteins. In addition to establishing a structural basis for the great differences in elongation rate constants at the two ends of bare actin filaments, our simulations provide a new framework for understanding the behavior of actin binding proteins that interact with terminal subunits. As an example, profilin has a high affinity for the barbed end of actin monomers, and a weak affinity for subunits in the flattened conformation. Concentrations of profilin that saturate barbed ends slow elongation (19, 20). Previously, it was assumed that the terminal subunits at the barbed end are flattened, but our simulations demonstrate that terminal subunit B has a monomeric conformation and subunit B-1 is only partially flattened so both may be able to bind profilin. Additionally, the freedom of subunit B reduces steric clashes when both subunits B and B-1 are bound to profilin. These insights lead to a straightforward mechanism by

which the FH2 domains of formins can promote the dissociation of profilin from subunit B: contacts with the FH2-domain may flatten subunit B, lowering its affinity for profilin.

2.4 Materials and Methods

System setup for molecular dynamics simulations. We constructed actin filaments in the ATP, ADP-P_i, and ADP-bound nucleotide states by patterning 13 of the corresponding F-actin structures reported in (10) (PDB: 6DJM, 6DJN, 6DJO) and using the accompanying rise and twist values. For PDB 6DJM, we substituted AMPPNP for ATP. We included waters in the catalytic center from previously-equilibrated actin filament simulations, and solvated the filament structure using VMD (21) plugin auto-solvate such that at least 11 Å of TIP3P water solvated each direction. We used the auto-ionize plugin to reach a charge-neutral system with a KCl concentration of 100 mM. Periodic boundaries were active across each box dimension, meaning at least 22 Å of buffer separated the protein from its periodic image. The CHARMM27 force field with CMAP correction was used (22).

Each of the systems were sequentially energy minimized in NAMD version 2.11 (23) for 200 ps using a 2-fs timestep under each of the following harmonic constraint selections (k = 10 kcal•mol^{-1}•Å^{-2}): (a) everything except buffer; (b) everything except buffer and protein sidechains; (c) only the bound nucleotide and Mg^{2+}; (d) only Mg^{2+}. This was followed by a heating protocol lasting 1 ns from 0 to 310K under constraint selection (a). The systems were then equilibrated with constraint selection (a) being progressively weakened by a factor of 2 every 400 ps for 5 iterations (i.e., k = 10, 5, 2.5, 1.25, 0.625 kcal•mol^{-1}•Å^{-2}) and followed by a final constrained equilibration with k = 0.1 kcal•mol^{-1}•Å^{-2} for 1 ns. The systems were equilibrated without constraints for 6 ns. Time courses include data immediately following equilibration, which illustrates transitions.

However, aggregate data analysis included data following an additional 200 ns of simulation, which represented the period after major structural transitions occurred.

Production runs were performed on NSF XSEDE supercomputers using the final frame of the equilibration protocol as an initial structure. These were performed using GROMACS version 2018.3 (24) with the leap-frog integrator in the isothermal-isobaric (constant *NPT*) ensemble using Parinello-Rahman pressure coupling and v-rescale temperature coupling. Electrostatic interactions were calculated using the particle mesh Ewald sum method with a cutoff of 1.2 nm.

Set up of the simulation of monomeric actin (PDB 1NWK) (4) was performed using the same protocol. Production runs of simulation 11 were performed in NAMD on group-owned compute nodes. Construction of simulation 13, a monomer with a flat dihedral angle, used the final frame of the 7^{th} subunit of the ATP-actin 13-mer from simulation 1 along with the nucleotide, Mg^{2+}, and nearby waters as its initial structure. This was then solvated, ionized, minimized, equilibrated, and run using the same protocol as detailed above.

It should be noted that PDBs 1NWK, 6DJM, 6DJN, and 6DJO have identical amino acid sequences, so comparisons between all of these molecules can be made straightforwardly.

Construction of simulation 10 (ADP-filament with folded D-loops; Table 2.1) used an early structure of the ADP-bound subunit (25), in which residues 36-58 were replaced by corresponding residues in simulations from reference (26) that had the D-loop in a helical conformation. The rest of the construction, minimization, equilibration, and production protocol was the same as with the other simulations. See Table 2.1 for initial structures and MD run times.

Although we constructed our actin filaments to include every subunit in a repeat length of actin (13 subunits), many of the interior subunits behaved similarly (Fig. 2.1E and 2.2C). Therefore, a shorter filament of ~7 subunits is likely appropriate for future MD studies and would save considerable computational cost.

Analysis protocols for molecular dynamics simulations. For the calculation of the dihedral angle, actin was divided into four subdomains following standard residue assignments: Subdomain 1 (SD1): residue 1 to 32, 70 to 144, 338 to 375; SD2: residue 33 to 69; SD3: residue 145 to 180, 270 to 337; SD4: residue 181 to 269. The center of mass of the C_α atoms of each subdomain was calculated and these positions were used to compute a dihedral angle SD2-SD1-SD3-SD4.

We reported a measurement of subunit-level root-mean-square fluctuation (RMSF) relative to neighboring subunits. To calculate this metric for subunit i, we aligned the simulation to the C_α atoms of two of the subunit's neighbors, either (i+1, i+2) or (i-1, i-2) depending on positioning in the filament. We then mapped subunit i into a single coarse-grained (CG) bead using the C_α center of mass of subunit i for its position. Finally, we calculated the RMSF of the CG bead throughout 40-ns windows for the simulation.

To quantify the occlusion of the D-loop, we calculated the accessible surface area (ASA). This analysis draws a surface one probe radius around the D-loop and calculates how much of it is blocked by something other than water or ions. ASA calculations are commonly performed in the context of solvent exposure, where the probe radius is chosen to approximate the radius of a water molecule (1.4 Å). In our study, the relevant context is the D-loop's availability to form new protein-protein interactions, so the probe radius was chosen to approximate the distance at which sidechains interact with each other. To account for the many ways in which sidechains are able to interact, we chose a 7 Å probe radius.

Table 2.1: Simulations performed in Chapter 2						
Number	F or G	Bound nucleotide	Replicate #	Time (ns)	PDB ID	Initial D-loop
1	F	ATP	1	742	6DJM	Extended
2	F	ATP	2	543	6DJM	Extended
3	F	ATP	3	620	6DJM	Extended
4	F	ADP-P_i	1	323	6DJN	Extended
5	F	ADP-P_i	2	798	6DJN	Extended
6	F	ADP-P_i	3	642	6DJN	Extended
7	F	ADP	1	808	6DJO	Extended
8	F	ADP	2	687	6DJO	Extended
9	F	ADP	3	589	6DJO	Extended
10	F	ADP	1	327	N/A[a]	Folded
11	G	ATP	1	347	1NWK	Extended
12	G	ATP	2	752	1NWK	Extended
13	G	ATP	1	672	N/A[b]	Extended

Table 2.1. Simulations performed in Chapter 2.
a: ADP-filament in which the D-loop of each subunit begins in a helical conformation. See *Materials and Methods* for details on constructing this system.
b: ATP-monomer in which the initial conformation is that of an interior subunit. This approximates an interior subunit stripped of its neighboring subunits. See *Materials and Methods* for details on constructing this system.

2.5 References

1. T. D. Pollard, Rate constants for the reactions of ATP- and ADP-actin with the ends of actin filaments. *J. Cell Biol.* **103**, 2747–2754 (1986).

2. T. D. Pollard, M. S. Mooseker, Direct measurement of actin polymerization rate constants by electron microscopy of actin filaments nucleated by isolated microvillus cores. *J. Cell Biol.* **88**, 654–659 (1981).

3. D. T. Woodrum, S. A. Rich, T. D. Pollard, Evidence for biased bidirectional polymerization of actin filaments using heavy meromyosin prepared by an improved method. *J. Cell Biol.* **67**, 231–237 (1975).

4. P. Graceffa, R. Dominguez, Crystal Structure of Monomeric Actin in the ATP State: STRUCTURAL BASIS OF NUCLEOTIDE-DEPENDENT ACTIN DYNAMICS. *J. Biol. Chem.* **278**, 34172–34180 (2003).

5. S. Vorobiev, *et al.*, The structure of nonvertebrate actin: Implications for the ATP hydrolytic mechanism. *Proc. Natl. Acad. Sci.* **100**, 5760–5765 (2003).

6. Z. A. O. Durer, *et al.*, Structural States and Dynamics of the D-Loop in Actin. *Biophys. J.* **103**, 930–939 (2012).

7. R. Dominguez, K. C. Holmes, Actin Structure and Function. *Annu. Rev. Biophys.* **40**, 169–186 (2011).

8. T. Oda, M. Iwasa, T. Aihara, Y. Maéda, A. Narita, The nature of the globular- to fibrous-actin transition. *Nature* **457**, 441–445 (2009).

9. F. Merino, *et al.*, Structural transitions of F-actin upon ATP hydrolysis at near-atomic resolution revealed by cryo-EM. *Nat. Struct. Mol. Biol.* **25**, 528–537 (2018).

10. S. Z. Chou, T. D. Pollard, Mechanism of actin polymerization revealed by cryo-EM structures of actin filaments with three different bound nucleotides. *Proc. Natl. Acad. Sci.* **116**, 4265–4274 (2019).

11. L. Blanchoin, T. D. Pollard, Hydrolysis of ATP by polymerized actin depends on the bound divalent cation but not profilin. *Biochemistry* **41**, 597–602 (2002).

12. M. A. Rould, Q. Wan, P. B. Joel, S. Lowey, K. M. Trybus, Crystal Structures of Expressed Non-polymerizable Monomeric Actin in the ADP and ATP States. *J. Biol. Chem.* **281**, 31909–31919 (2006).

13. M. McCullagh, M. G. Saunders, G. A. Voth, Unraveling the Mystery of ATP Hydrolysis in Actin Filaments. *J. Am. Chem. Soc.* **136**, 13053–13058 (2014).

14. R. Sun, O. Sode, J. F. Dama, G. A. Voth, Simulating Protein Mediated Hydrolysis of ATP and Other Nucleoside Triphosphates by Combining QM/MM Molecular Dynamics with Advances in Metadynamics. *J. Chem. Theory Comput.* **13**, 2332–2341 (2017).

15. A. Narita, T. Oda, Y. Maéda, Structural basis for the slow dynamics of the actin filament pointed end: Structure of the actin filament pointed end. *EMBO J.* **30**, 1230–1237 (2011).

16. I. Fujiwara, D. Vavylonis, T. D. Pollard, Polymerization kinetics of ADP- and ADP-Pi-actin determined by fluorescence microscopy. *Proc. Natl. Acad. Sci.* **104**, 8827–8832 (2007).

17. D. Drenckhahn, T. D. Pollard, Elongation of actin filaments is a diffusion-limited reaction at the barbed end and is accelerated by inert macromolecules. *J. Biol. Chem.* **261**, 12754–12758 (1986).

18. B. G. Horan, A. R. Hall, D. Vavylonis, Insights into Actin Polymerization and Nucleation Using a Coarse-Grained Model. *Biophys. J.* **119**, 553–566 (2020).

19. N. Courtemanche, T. D. Pollard, Interaction of Profilin with the Barbed End of Actin Filaments. *Biochemistry* **52**, 6456–6466 (2013).

20. J. Funk, *et al.*, Profilin and formin constitute a pacemaker system for robust actin filament growth. *eLife* **8**, e50963 (2019).

21. W. Humphrey, A. Dalke, K. Schulten, VMD: Visual molecular dynamics. *J. Mol. Graph.* **14**, 33–38 (1996).

22. B. R. Brooks, *et al.*, CHARMM: The biomolecular simulation program. *J. Comput. Chem.* **30**, 1545–1614 (2009).

23. L. Kalé, *et al.*, NAMD2: Greater Scalability for Parallel Molecular Dynamics. *J. Comput. Phys.* **151**, 283–312 (1999).

24. D. Van Der Spoel, *et al.*, GROMACS: fast, flexible, and free. *J. Comput. Chem.* **26**, 1701–1718 (2005).

25. S. Z. Chou, T. D. Pollard, "Mechanism of actin polymerization revealed by cryo-EM structures of actin filaments with three different bound nucleotides" (Biochemistry, 2018) https:/doi.org/10.1101/309534 (May 16, 2020).

26. H. H. Katkar, *et al.*, Insights into the Cooperative Nature of ATP Hydrolysis in Actin Filaments. *Biophys. J.* **115**, 1589–1602 (2018).

Chapter 3: Cracked actin filaments as mechanosensitive receptors

Preface

The work presented in this chapter was performed in collaboration with Margaret Gardel, David Kovar and Gregory Voth. I performed the simulations and analyzed the data presented in all figures.

Abstract

Actin filament networks are exposed to mechanical stimuli. Recent studies have revealed that proteins in the LIM domain family localize to regions of the actin cytoskeleton under mechanical strain, but the molecular basis of this mechanosensitivity is unknown. We use all-atom molecular dynamics simulations to apply tensile strains to actin filaments. We find that a conformational change disrupts a critical connection between longitudinal neighboring subunits, which leads to a metastable cracked conformation of the actin filament. This crack exposes two binding sites that are recognized by LIM domains in protein-protein docking simulations. Through its interactions with the cracked interface, LIM increases the time damaged filaments remain stable. Our findings provide a new model for mechanosensitive binding to actin filaments.

Significance Statement

Cells continually experience mechanical strain. Interactions between actin filaments and actin-binding proteins have been observed to be altered by mechanical stimuli in recent experimental studies. However, the structural basis of this mechanosensitivity is not understood. We used molecular dynamics and protein-protein docking simulations to investigate how tension alters the actin filament binding surface and interactions with associated proteins. We identify a

novel strain-induced binding site, show that mechanosensitive actin-binding proteins preferentially associate with it, and observe that these binding interactions stabilize damaged actin filaments.

3.1 Introduction

Eukaryotic cells utilize the actin cytoskeleton to move, change and maintain shape, divide, and transport cargo. These processes subject the underlying actin filament (F-actin) cytoskeleton to a wide range of mechanical forces including tension, bending, compression, and twisting (1, 2). Cells utilize mechanotransduction pathways to exploit mechanical cues to modify biochemical activity, which enables cells to alter cell physiology, transcription, and actin dynamics (1-3). For example, the actin-binding proteins (ABPs) Arp2/3 complex (4, 5) , α-catenin (6), and in some studies, cofilin (7, 8) , have been reported to exhibit altered binding affinities for actin filaments subjected to mechanical strain. These altered ABP interactions have important downstream implications for network architecture, stiffness, and disassembly (1, 2).

At the molecular level, actin filaments are composed of two protofilament strands that form a double helix (Fig. 3.1A). Individual actin subunits within the filament form inter-strand (lateral) or intra-strand (longitudinal) interactions with neighboring subunits. A number of cryo-electron microscopy (cryo-EM) structures have recently been reported of actin filaments up to a resolution of 2.2 Å (9-12). These structures have facilitated an unprecedented understanding of the conformation of actin filaments under unstrained conditions. However, much less is known about how the conformation of the actin filament changes under strain. A pioneering cryo-EM study recently reconstructed bent actin filaments at a resolution of ~3.6 Å (12). These structures revealed deformations to the actin filament lattice consistent with the twist-bend coupling predicted by theoretical studies and did not find that the filament surface charge or hydrophobicity changes in

a meaningful way. As such, the molecular mechanism by which binding of mechanosenstive ABPs is activated by strain remains an open question.

For example, recent studies have identified that proteins in the LIM (Lin11, Isl-1, and Mec-3) domain family localize to actin filaments under mechanical strain (13, 14). Structurally, LIM domains are ~60 amino acid sequences containing two zinc finger motifs, and many LIM proteins contain multiple LIM domains in tandem separated by flexible linkers of 7-8 amino acids (14). These studies observed that the LIM-containing region (LCR) of these proteins alone is sufficient for force-activated binding to F-actin *in vivo* and *in vitro,* but that multiple tandem LIM domains with characteristic spacings are required for mechanosensitivity (13, 14). A subsequent study reported that a single LIM domain of testin is mechanosensitive on its own (15), but presently this is the only known exception. Despite a growing body of experimental literature investigating the behavior of a diverse set of LIM domain proteins, a mechanistic understanding of how LIM recognizes strained F-actin remains unknown.

Here we use all-atom molecular dynamics (MD) simulations to investigate the structure and dynamics of actin filaments under applied tension. We find that Y169 of one subunit flips away from the D-loop of its longitudinal neighboring subunit, which leads to the breaking of a single protofilament prior to filament fragmentation. This metastable cracked interface alters the filament binding surface, which mechanosensitive LIM domains preferentially associate with and their presence stabilizes damaged filaments. Our results elucidate key steps of the filament fragmentation pathway, lead to natural explanations for why multiple tandem LIM domains increase mechanosensitive binding, and provide a new molecular model for mechanosensitive binding to F-actin generally.

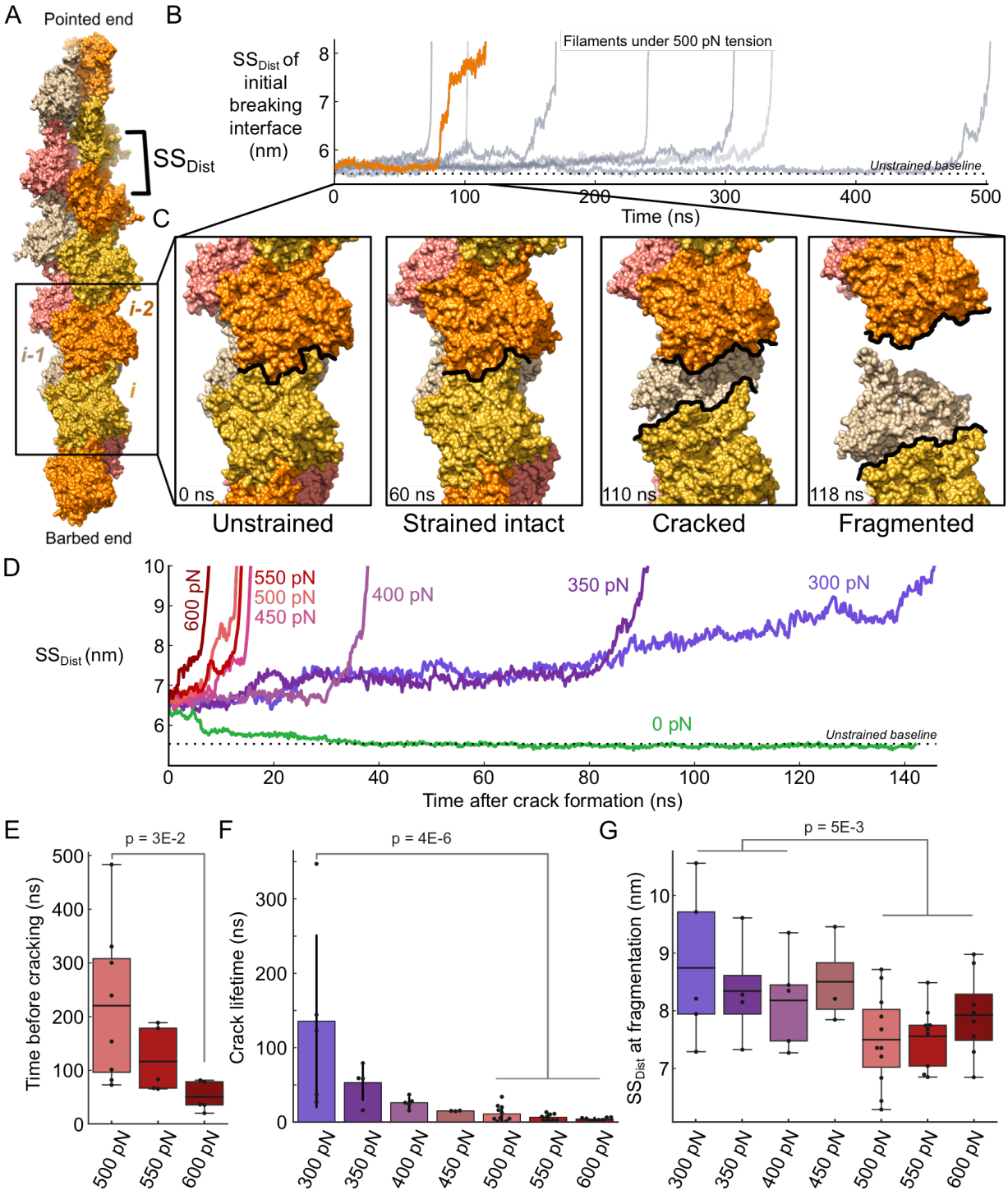

Figure 3.1 Actin filaments enter a metastable 'cracked' state prior to fragmentation.
(A) Space-filling model of the initial structure of an ADP-actin 13-mer. The two strands of the protofilament are colored in alternating orange and yellow, and pink and tan, respectively. The distance between longitudinal neighboring subunits, subunit-subunit distance (ss_{dist}), is labeled. (B) Time courses of the ss_{dist} at the initial breaking interface in all simulations run at 500 pN tension. (C) Space-filling models of simulation snapshots depicting the initial breaking interface in unstrained, strained-intact, cracked, and fragmented conformations.

Figure 3.1 continued: (D) Time courses of the ss_{dist} of cracked interfaces run under different magnitudes of tension depict a tension-dependent lifetime of cracks. In the absence of tension, cracked interfaces spontaneously return to unstrained baseline values (green). (E) Box plots of the time before the initial interface cracks reveal an inverse relationship between the applied force and the time the filament remains intact. (F) Bar plots of the time spent in the cracked state reveal that the crack lifetime is inversely correlated with the magnitude of the tension applied. Error bars represent standard deviation. The p-value is calculated between 300 pN and cases ≥ 500 pN. (G) Box plots of the ss_{dist} at the time of fragmentation show that the lower tensions fragment with larger separations at the cracked interface. The p-value is calculated between cases ≤ 400 pN and cases ≥ 500 pN.

3.2 Results

Actin filament fragmentation involves a metastable 'cracked' state. In all-atom MD simulations of actin filaments under applied tension, strains of 500 pN and above caused filaments to fragment within timescales accessible by large all-atom MD (~1 μs), whereas tensions 400 pN and below did not result in breaks on this timescale (Table 3.1). Interestingly, filament fragmentation did not occur as a single discrete event. Instead, longitudinal connections between subunits on each protofilament broke separately. At all longitudinal interfaces, including the first interface to break, the ss_{dist} initially remained close to the unstrained baseline value of ~5.53 ± 0.02 nm (Fig. 3.1B) and maintained the typical longitudinal connections of unstrained filaments (Fig. 3.1C *middle left*). After a period where all strained interfaces remained intact, one longitudinal interface lost contact and separated while interfaces on the other protofilament maintained their connections, which resulted in the formation of a metastable 'crack' (Fig. 3.1C *middle right*). Under continued tension, one of the laterally neighboring interfaces eventually lost contact and the filament fully fragmented (Fig. 3.1B, C *right*).

The timing of the steps along the fragmentation pathway was modulated by tension. Increasing the strain applied to the filament after the crack formed decreased the amount of time

before the filament fragmented (Fig. 3.1D, F). Conversely, cracks spontaneously reformed lost contacts in the absence of applied tension (Fig. 3.1D, green line*)*. The time preceding the initial break (i.e., the crack) also inversely correlated with strain (Fig. 3.1E). The ss_{dist} of the cracked interface at fragmentation somewhat trended with tension, whereby cracks under higher tensions resulted in fragments at lower separations (Fig. 3.1G).

Actin filaments break at interfaces where Y169 has flipped away from the D-loop. In unstrained actin filaments, the D-loop of subunit i completely envelopes Y169 of the neighboring subunit i-2 (9, 10). This connection provides a substantial fraction of the buried surface area between subunits (9) and is the primary connection between the terminal barbed end subunit and the rest of the filament (16). Under tension, the initial breaking interface was characterized by Y169 of subunit i-2 flipping away from the D-loop of subunit i (Fig. 3.2A). This flip increased the distance between Y169 and the D-loop from ~4 to >7 Å (Fig. 3.2B *top*) and precluded the typical enveloping interaction. In turn, the number of contacts Y169 formed with residues in subunit i decreased from ~10 to ~4 (Fig. 3.2B *middle top*). As this important connection eroded, the ss_{dist} of the interface increased (Fig. 3.2B *middle bottom*) in step with a marked decrease of the overall number of contacts between subunits i and i-2 (Fig. 3.2B *bottom*).

While the average interface maintained the low ~4 Å Y169 to D-loop distance in unstrained filament cryo-EM structures, there was a subpopulation of interfaces where Y169 was in the flipped orientation (Fig. 3.2C, *dark gray bar and small dots*). Interfaces under tension, but not at the breaking interface showed a similar distribution of Y169 orientations (Fig. 3.2C, *light gray bar and small dots*). However, at interfaces that broke, Y169 was always in the flipped state at the time the break occurred (Fig. 3.2C, *orange bar*). Intuitively, these trends were reflected in the number of connections Y169 of subunit i-2 formed with subunit i (Fig. 3.2D). Although Y169 flipping was

possible in unstrained simulations, the rate of flipping increased ~5 fold under tension (Fig. 3.2E). Flips of Y169 only resulted in broken longitudinal interfaces under applied tension and did not lead to cracks in unstrained simulations.

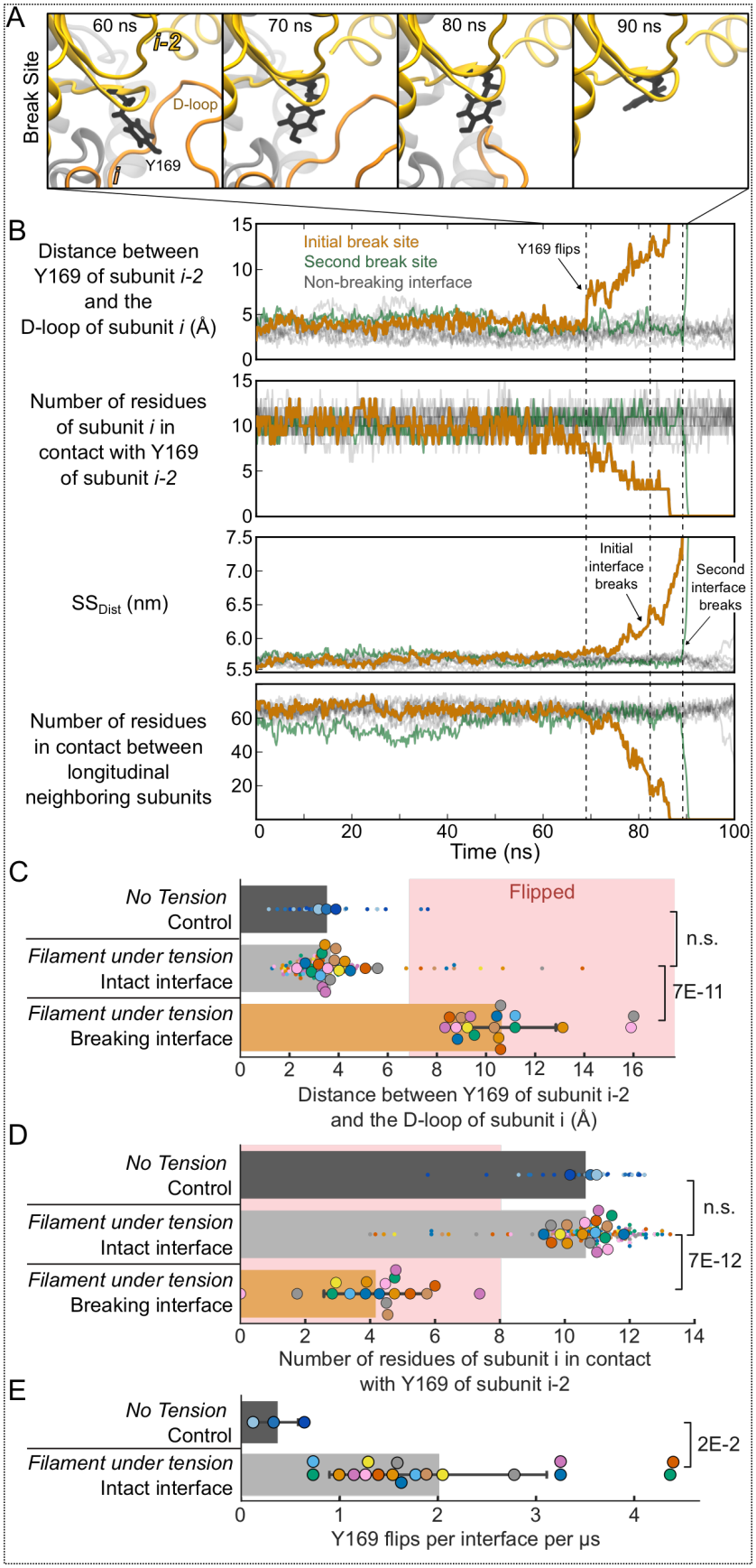

Figure 3.2 Actin filaments break at interfaces where Y169 of subunit i-2 flips away from the D-loop of subunit i.
(A) Snapshots of a longitudinal interface breaking under 550 pN of tension. The break is preceded by Y169 of subunit i-2 (black) flipping away from its connection with the D-loop of subunit i (orange). (B) Time courses of key metrics tracking a longitudinal interface breaking under 550 pN of tension. The first and second interfaces to break are shown in orange and green, respectively, and non-breaking interfaces are shown in gray. (Top) The distance between the CZ atom of Y169 of subunit i-2 and the center of mass of Cα of residues 41, 42, 48, 49 of the D-loop of subunit i at each interface reveals a characteristic flip of Y169 at the initial break site. (Middle Top) After flipping, the number of residues of subunit i in contact with Y169 of subunit i-2 decreases. (Middle Bottom, Bottom) The distance between the center of masses of subunits i and i-2, ss_{dist}, at the initial break site increases in step with a corresponding decrease in the total number of contacts and leads to complete fragmentation. Contacts are calculated using a 5 Å cutoff. Dashed lines mark the annotated transitions.

Figure 3.2 continued: (C and D) Swarm plots of the distance between the CZ atom of Y169 of subunit i-2 and the center-of-mass of the D-loop of subunit i (C), as well as the number of inter-subunit contacts with Y169 (D) show that intact interfaces with and without tension (dark and light gray bars, respectively) both generally maintain unflipped Y169 residues with a small population of flipped residues. In contrast, Y169 is flipped at breaking interfaces, which results in reduced contacts (orange bars). Values are averages of the final 2% of frames preceding the initial break. Small dots represent individual interfaces, while large dots represent the mean across all interfaces in a given simulation; color corresponds to replicates. Error bars represent standard deviation; p-values are displayed on the right. (E) Swarm plots of the rate of Y169 flipping reveal that tension increases the rate of flipping events. Error bars represent standard deviation; the p-value is displayed on the right.

The cracked interface presents a unique binding surface. Unstrained filaments maintained an ss_{dist} of 5.53 ± 0.02 nm (Fig. 3.3A). Strained-intact filaments showed a slight but consistent increase relative to this with increasing tension. At 200 pN, the ss_{dist} was 5.57 ± 0.01 nm, whereas the ss_{dist} was 5.71 ± 0.03 nm for intact interfaces under 600 pN (Fig. 3.3A). In contrast, cracked interfaces maintained much larger ss_{dist} values of 6.94 ± 0.37 nm (Fig. 3.3A).

Because cracked and strained-intact interfaces are both mechanically-induced states of the actin filament with the potential to present cryptic binding sites for mechanosensitive actin binding proteins, we evaluated how the filament surface in these states differed from unstrained filaments. In particular, we were interested in if the slight increases observed in the ss_{dist} of strained-intact filaments would expose residues to the filament surface that are buried in unstrained filaments. To quantify these changes, we performed accessible surface area (ASA) calculations of each amino acid at a probe radius of 4 Å. This revealed that the increased separation between longitudinal neighboring subunits in strained-intact filaments did not translate into large increases of the accessibility of individual amino acids (Fig. 3.3B *left* and 3.4). In contrast, cracked interfaces showed meaningful increases in the accessibility of many typically-buried residues (Fig. 3.3B *middle* and 3.5), some of which became exposed to levels comparable to completely fragmented interfaces (Fig. 3.3B *right* and 3.6). Many of the largest gains were made by hydrophobic residues

in the central D-loop of subunit i, V43, V45, M44, and M47 (Fig. 3.3C) that typically contact Y169 of subunit i-2 at intact interfaces. Summing over all residues, cracked interfaces had more than 11 times the increase in ASA of strained-intact interfaces, and over half the increase in ASA of fragmented interfaces (Figs. 3.4, 3.5, and 3.6).

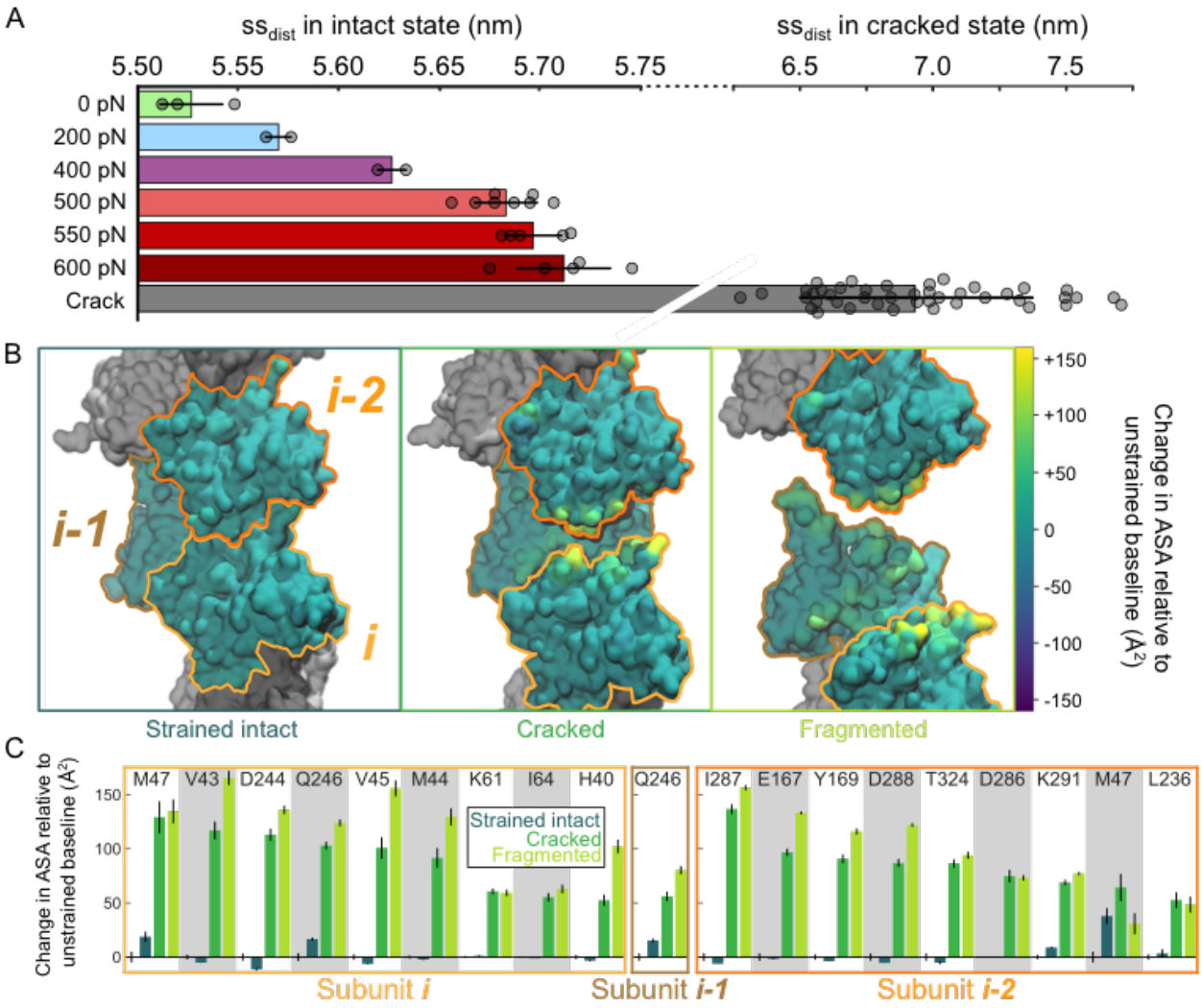

Figure 3.3 Cracks present a unique mechanosensitive binding surface, whereas surfaces of strained-intact filaments differ minimally from unstrained filaments

(A) Bar plots of the ss_{dist} reveal a consistent increase in the average distance between longitudinal neighboring subunits in intact filaments under tension, up to ~2 Å. The ss_{dist} of cracked interfaces are shown for comparison; Note the broken axis. Error bars represent standard deviations. (B) Space-filling models of filament interfaces in the strained intact, cracked, and fragmented states with surfaces colored according to the change in accessible surface area (ASA) of residues relative to unstrained baseline interfaces. Strained-intact interfaces do not show major differences relative to baseline, whereas cracked interfaces expose many typically-buried residues, some of which are comparable to values of fragmented interfaces. Only changes in ASA that are significantly different from unstrained ($p < 0.05$) are included. (C) Bar plots of the average change in ASA of residues that show the greatest increase relative to subunits within unstrained filaments. Each residue is separated by alternating shaded regions and contains four bars corresponding to unstrained, strained intact, cracked, and fragmented interfaces. Unstrained is the baseline case and therefore has a mean of 0. The probe radius is 4 Å and residues are included if either the strained intact or cracked states differed from unstrained by more than 50 $Å^2$; All residues are shown in Figs. 3.4, 3.5, and 3.6. Error bars represent standard error.

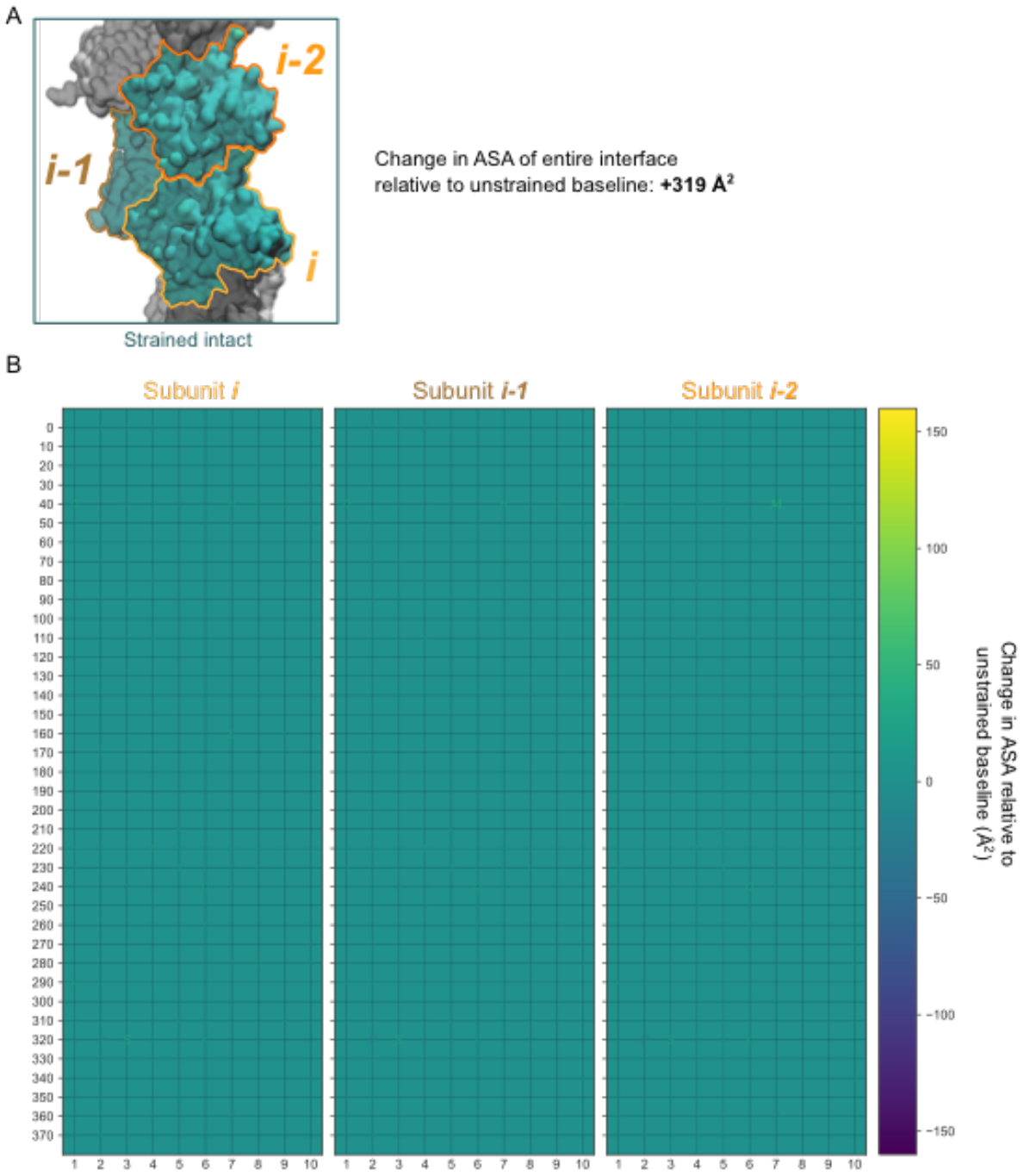

Figure 3.4 Strained-intact interfaces present a similar binding surface to interfaces in unstrained actin filaments.
(A) Space-filling representation of a typical strained-intact interface. Color corresponds to change in accessible surface area (ASA) relative to unstrained actin filaments according to the color bar in (B). (B) Three grids list every amino acid in subunits i, i-1, and i-2 at a strained-intact interface. The size and color of each amino acid is scaled based on the change in ASA. Given that all residues in strained-intact filaments maintain roughly the same ASA of unstrained filaments, these grids appear empty. The ASA probe radius is 4 Å.

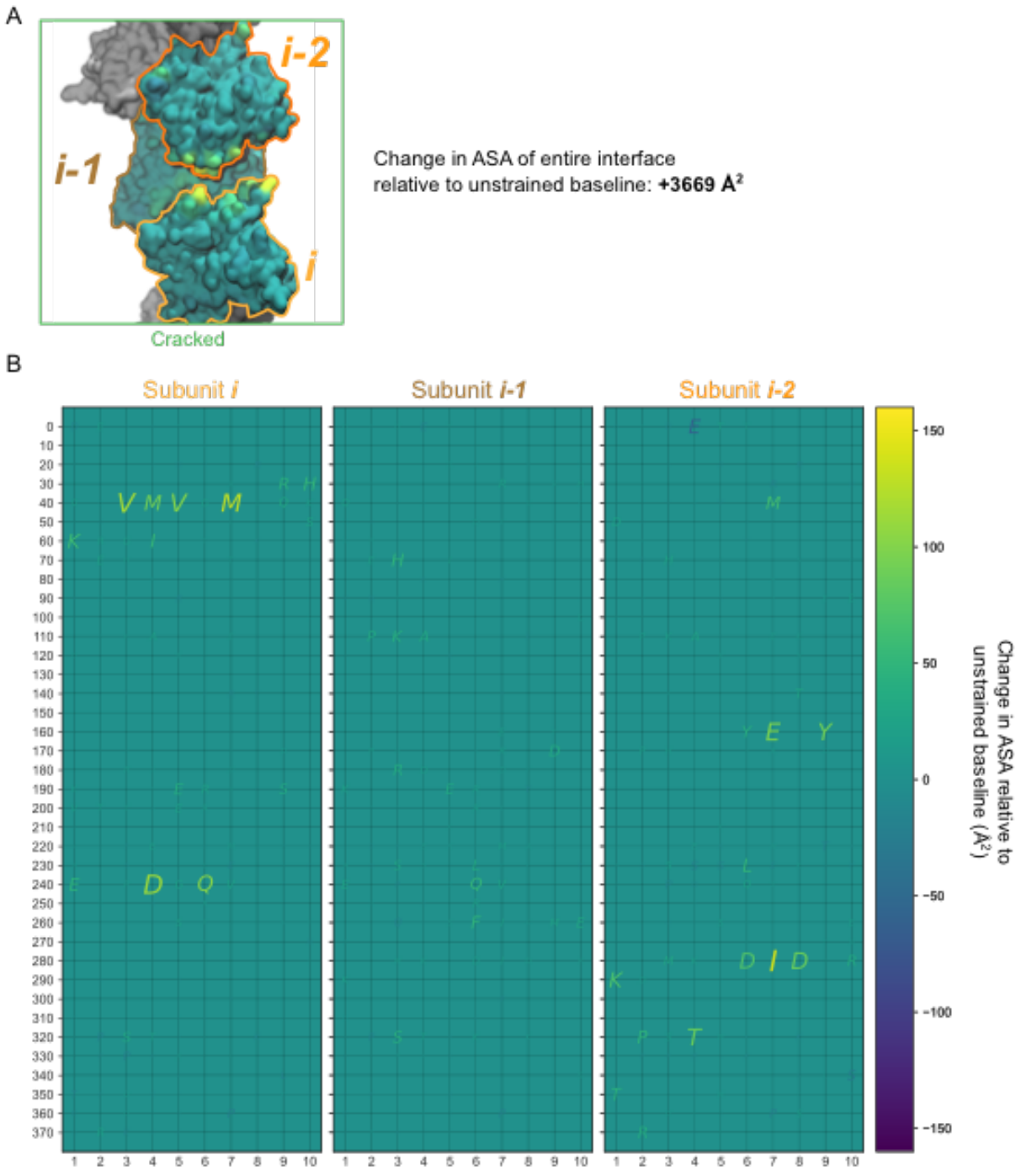

Figure 3.5 Cracked interfaces present a unique mechanosensitive binding surface.
(A) Space-filling representation of a typical cracked interface. Color corresponds to change in accessible surface area (ASA) relative to unstrained actin filaments according to the color bar in (B). (B) Three grids list every amino acid in subunits i, i-1, and i-2 at a cracked interface. The size and color of each amino acid is scaled based on the change in ASA. The ASA probe radius is 4 Å.

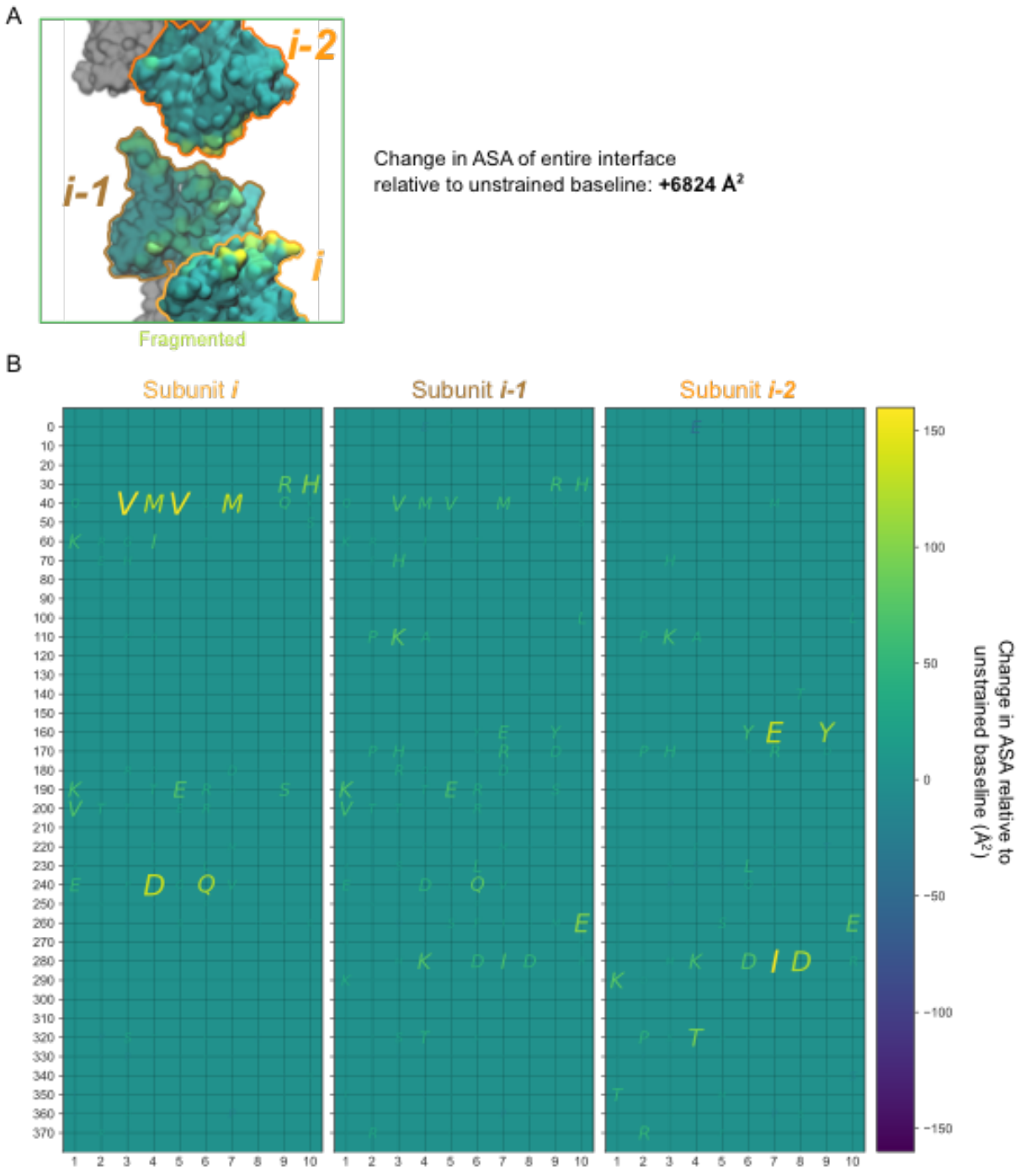

Figure 3.6 Filament fragmentation exposes typically-buried amino acids.
(A) Space-filling representation of a typical cracked interface. Color corresponds to change in accessible surface area (ASA) relative to unstrained actin filaments according to the color bar in (B). (B) Three grids list every amino acid in subunits i, i-1, and i-2 at a fragmented interface. The size and color of each amino acid is scaled based on the change in ASA. The ASA probe radius is 4 Å.

LIM domains bind cracked interfaces and stabilize filaments under tension

Given that cracks present a highly unique filament surface, we tested whether various ABPs associate preferentially with cracked interfaces by performing protein-protein docking simulations using ClusPro2.0 (see Methods) (17). We used the cracked 13-mer filament structure that emerged from MD simulations as the receptor and individual ABP structures as the ligand molecule. Because a limited number of LIM domain structures have been solved experimentally, we employed Alphafold2 (see Methods) (18) to predict the folded structure of 43 individual LIM domain sequences (Fig. 3.7A). We found that LIM domains had a strong preference for binding the cracked interface, and this preference was unique relative to other ABPs, such as cofilin, profilin, and Lifeact (Fig. 3.8A). This was particularly striking given that, in addition to one cracked interface, the actin 13-mer receptor contained ten strained-intact interfaces that were available for binding, which served as an internal control for each simulation.

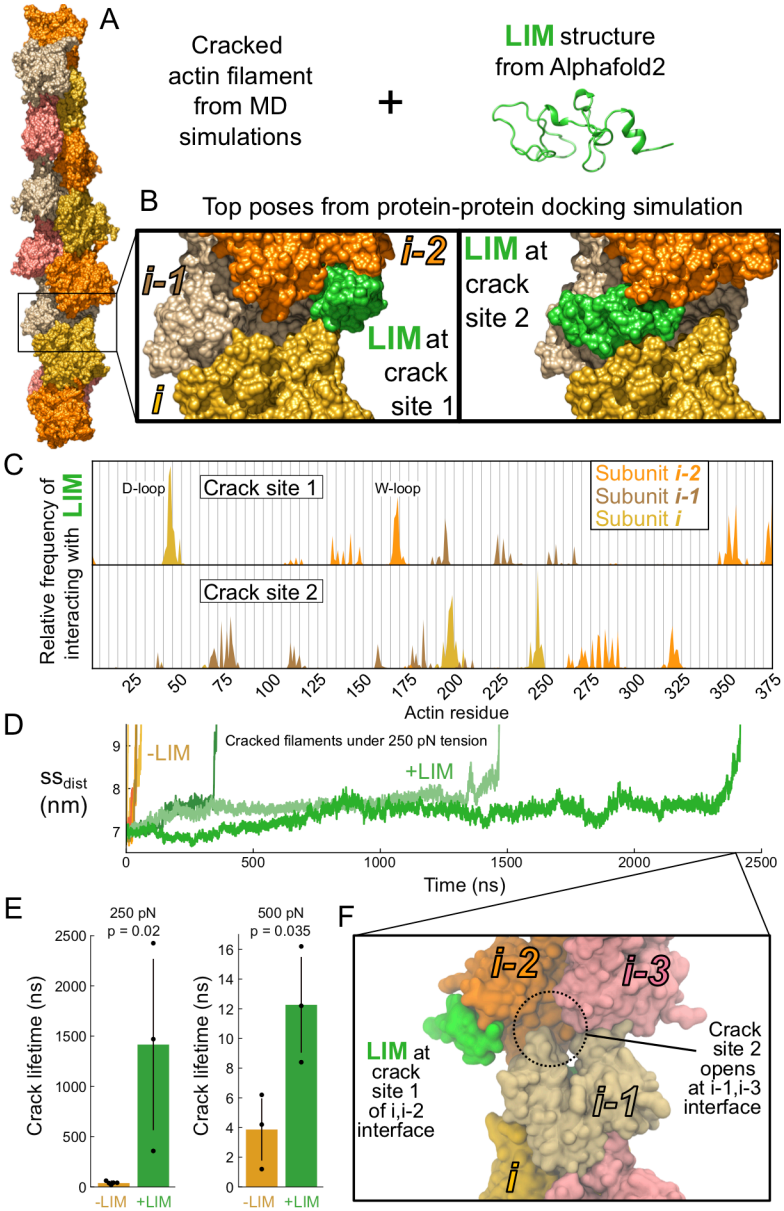

Figure 3.7 LIM domains bind cracked interfaces at two sites and stabilize filaments. (A) Left, Space-filling model of an actin 13-mer filament with a single cracked interface. Right, Ribbon diagram of a single LIM domain predicted by Alphafold2. The filament and LIM domains are input into protein docking simulations as the receptor and ligand, respectively. (B) Space-filling models of representative output poses from docking simulations of LIM domains bound to crack site 1 and crack site 2. Top poses for all LIM domain sequences bind the cracked interface over all other regions of the filament surface. (C) Frequency that each actin residue is in contact (5 Å cutoff) with LIM in docked structures at crack site 1 (top) and crack site 2 (bottom). Data is aggregated across all 43 LIM domain sequences tested.

Figure 3.7 continued: (D) Time courses of the ss_{dist} of an MD simulation of a cracked actin 7-mer with (green) and without (orange) LIM domains bound to both crack sites under 250 pN of tension. The bound LIM domain is the first LIM domain of testin. (E) Bar plots of the crack lifetime at two tensions show LIM domains stabilize damaged actin filaments. Error bars represent standard deviation. (F) Snapshot of an actin filament with LIM domains bound to the initial cracked interface reveals that crack site 2 of the interface on the opposing strand becomes exposed prior to fragmentation.

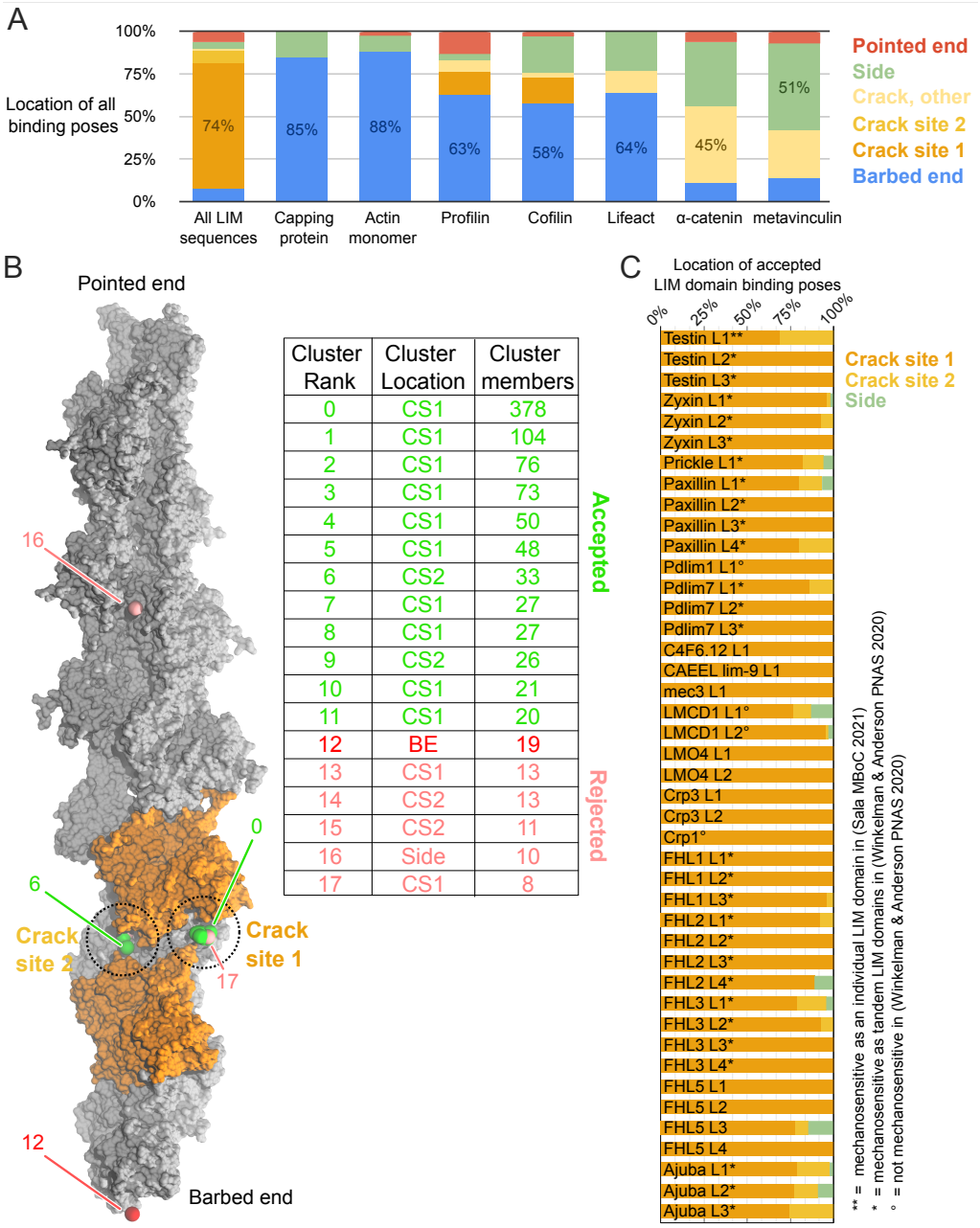

Figure 3.8. Docking simulations.
(A) Location of all docking poses on a cracked actin 13-mer receptor. Each column corresponds to a different ligand. All 43 LIM domain sequences are shown at left as an aggregated dataset. The most likely binding location for each ligand is labeled as a percentage on the bar. Note that LIM domains have a striking preference for the cracked interface. (B) Illustration of docking simulation processing. (Left) Space-filling model of the actin 13-mer receptor with subunits at the cracked interface highlighted in orange. Spheres represent the center of mass of each binding pose output by ClusPro2.0 for a single LIM domain sequence. Several spheres are labeled with their ranking by cluster size. Color corresponds to acceptance/rejection. (Right) Table of all binding poses. Poses with cluster size larger than the highest-ranked end-binding pose (red) are accepted (green) while others are rejected (pink). CS1/CS2 = crack site 1/2.

Figure 3.8. continued: (C) Location of all accepted binding poses for each LIM domain sequence. In total, ~93% of accepted binding is at crack site 1, ~5% is at crack site 2, and <2% is on the filament side, not at the crack site.

Individual LIM domains bound the cracked interface in two locations (Fig. 3.7B). The vast majority of binding poses were located between subdomain 2 of subunit i and subdomains 1 and 3 of subunit i-2 (Fig. 3.7B), accounting for 93% of accepted poses across the 43 LIM domain sequences (Fig. 3.8C). In this position, LIM bridged the broken connection between the D-loop and the W-loop containing Y169 and made contact with all three subunits at the cracked interface (Fig. 3.7C). In the second most common binding location, crack site 2, the LIM domain contacted subdomain 4 of subunit i and subdomain 3 of subunit i-2 simultaneously (Fig. 3.7B and C). Many of the key actin residues that LIM interacted with at the two crack sites (Figs. 3.9B and 3.10B) only became exposed once cracks formed (Fig. 3.5B). Less than 2% of accepted binding poses positioned LIM on the side of the filament, but not at the cracked interface (Fig. 3.8C).

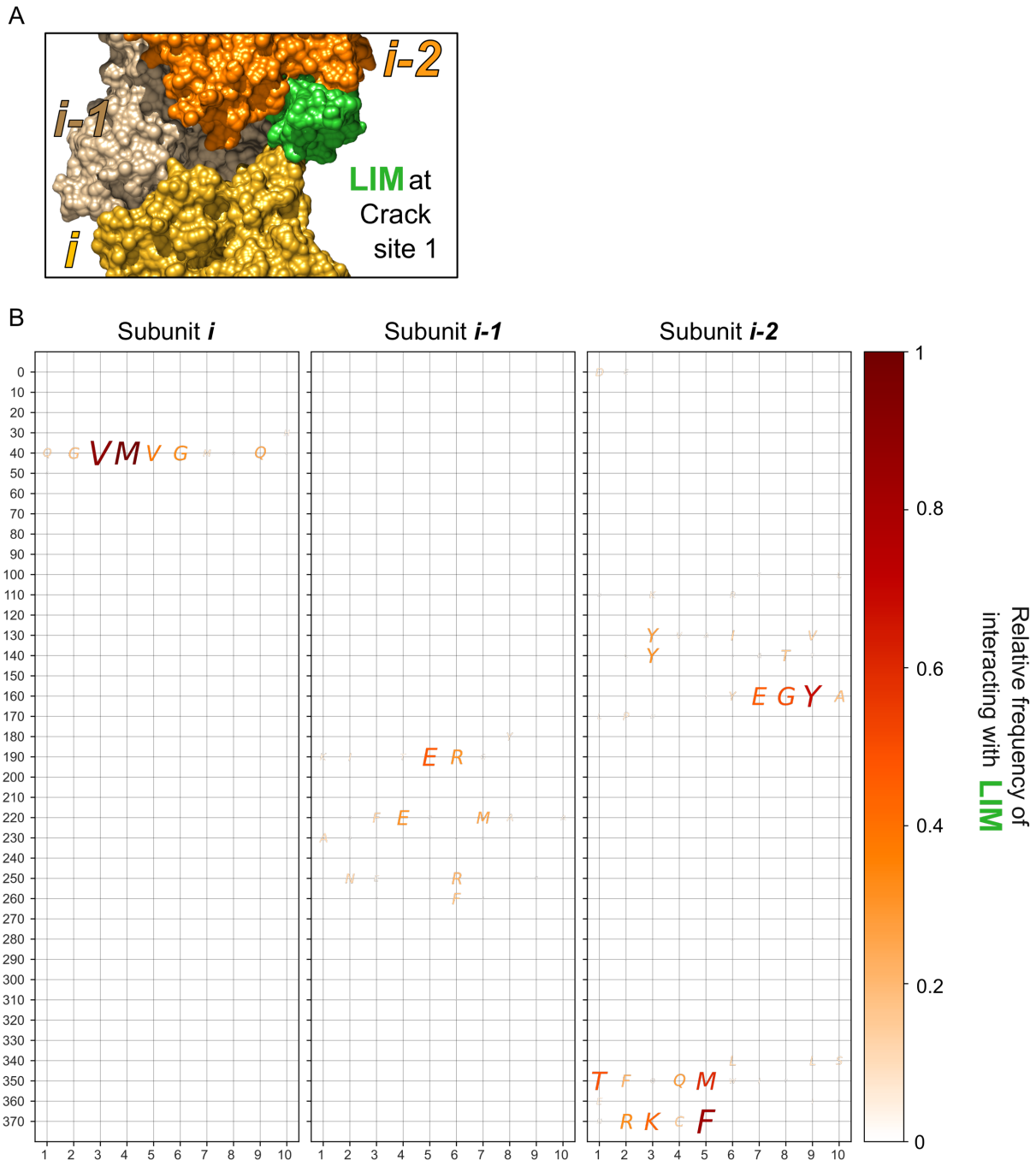

Figure 3.9. LIM domains bound to crack site 1 interact with residues that become exposed at cracked interfaces.

(A) Space-filling representation of a LIM domain (green) bound to the cracked interface at crack site 1. (B) Three grids list every amino acid in subunits i, i-1, and i-2 at the cracked interface. The size and color of each amino acid is scaled based on its relative frequency of interacting with LIM bound to crack site 1 across all accepted binding poses of all 43 LIM domain sequences. Contact was calculated using a 5 Å cutoff.

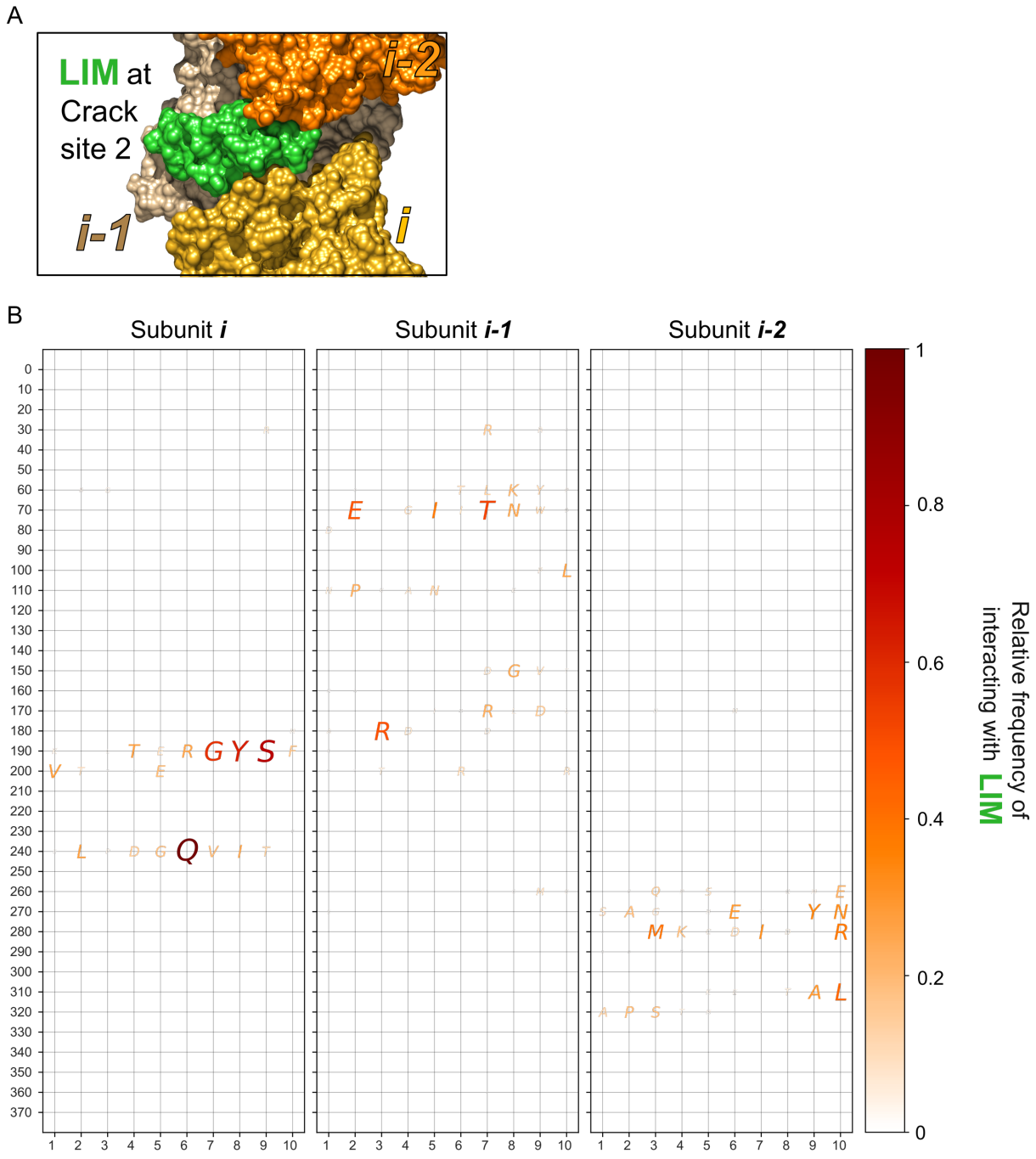

Figure 3.10. LIM domains bound to crack site 2 interact with residues that become exposed at cracked interfaces.
(A) Space-filling representation of a LIM domain (green) bound to the cracked interface at crack site 2. (B) Three grids list every amino acid in subunits i, i-1, and i-2 at the cracked interface. The size and color of each amino acid is scaled based on its relative frequency of interacting with LIM bound to crack site 2 across all accepted binding poses of all 43 LIM domain sequences. Contact was calculated using a 5 Å cutoff.

Intriguingly, a LIM domain bound to crack site 1 does not clash with a LIM domain bound to crack site 2, suggesting two LIM domains can bind a single cracked interface. This is particularly interesting because multiple LIM domains in tandem were observed to be an important driver of mechanosensitivity *in vivo* (13, 14). Having multiple, non-mutually exclusive LIM binding sites at the crack suggests a structural basis for LIM domain's apparent avidity-driven mechanosensitive response.

Although previous work has focused on LIM domains as sensors of strained actin filaments that recruit repair proteins such as VASP and α-actinin, we sought to test the idea that the presence of LIM at the cracked interface stabilizes the filament by itself. To that end, we built an MD system consisting of a cracked actin 7-mer with one LIM domain bound to each of crack sites 1 and 2. At both 250 pN and 500 pN tensions, the presence of LIM domains noticeably prolonged the period of time before the filament fragmented. This was especially pronounced at 250 pN, where the presence of LIM domains at the cracked interface increased the time before fragmentation over 37-fold from 38 ± 16 ns to 1416 ± 841 ns (Fig. 3.7D and E).

Interestingly, immediately before fragmentation, crack site 2 of the opposite protofilament became exposed (Fig. 3.7F). This suggests the possibility that after a crack has formed and been stabilized by LIM domains on one protofilament, continued tension can expose additional crack sites on the laterally neighboring interfaces available for further LIM binding.

3.3 Discussion

Y169 to D-loop connection. We find that flipping of Y169 away from the neighboring subunit's D-loop is a necessary step for longitudinal interfaces to break under strain (Fig. 3.11A). This result adds to the evidence that the connection between Y169 of subunit i-2 and the D-loop

of subunit i is critical for maintaining the stability of actin filaments. In addition to residue 169 being highly conserved as either a tyrosine or phenylalanine in WT actin sequences, previous studies have demonstrated that the D-loop's connection with Y169 buries a large fraction of the surface area between subunits within the polymer (9) and alone can support the terminal barbed end subunit’s attachment to the filament (16).

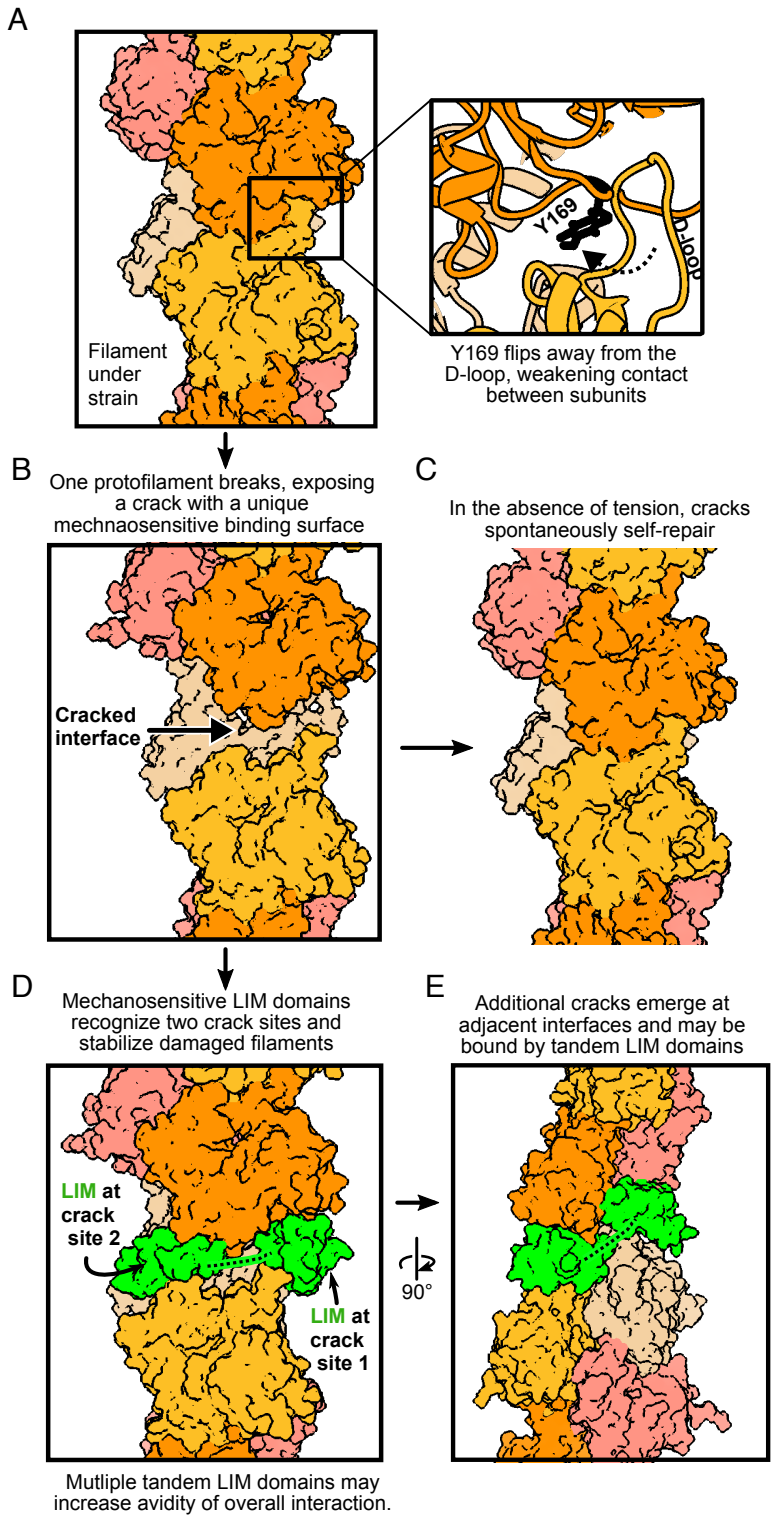

Figure 3.11. Cracked actin filaments as a mechanosensitive receptor. (A) Actin filaments subjected to mechanical strain break at interfaces where Y169 has flipped away from the D-loop of the neighboring subunit. Y169 flipping occurs more frequently at higher strains. (B) One protofilament breaks, while the other maintains all of its longitudinal connections, resulting in a cracked interface with a unique binding surface. (C) Cracks spontaneously self-repair when tension is no longer applied. (D) Cracks are mechanosensitive binding sites. LIM domains (green) can bind cracked interfaces in two non-mutually exclusive locations. Cracked interfaces with bound LIM domains withstand applied strain longer than without LIM bound. Dashed line represents the flexible linker between tandem LIM domains. (E) Under continued strain, additional cracks can form on the opposite protofilament strand. Tandem LIM domains may be able to bind cracks of two neighboring interfaces simultaneously, providing additional stability to the filament by binding both protofilaments. Dashed line represents the flexible linker between tandem LIM domains.

Given the importance of residue Y169, one could imagine that mutations away from tyrosine or phenylalanine would result in deleterious effects. One experimental study explored the naturally-occurring zebrafish mutation Y169S (23). *In vivo,* the authors observed that the phenotype showed a loss of filamentous actin. *In vitro*, the authors purified the equivalent yeast actin mutation F169S, which initially nucleated and polymerized, but rapidly depolymerized into fragments thereafter. This behavior was rescued by introducing phalloidin, a molecule that stabilizes actin filaments. Our results suggest a potential mechanism to explain the surprising behavior of this mutation. If F169S actin initially forms a favorable connection between residue 169 and the D-loop of the adjacent subunit, it may be able to nucleate and polymerize. However, if the rate at which S169 loses its connection with the D-loop is much higher than WT (e.g., by flipping quickly under thermal fluctuations), then it will rapidly break apart into fragments. Phalloidin, by reinforcing connections between subunits, would stabilize the filament enough to overcome the unfavorable orientation of S169 and suppress the resulting fragmentation.

Cracks as mechanosensitive receptors. We find that cracked interfaces present a unique force-induced binding surface, while subunits at strained-intact interfaces appear remarkably similar to subunits in unstrained actin filaments. In particular, amino acids do not generally become more exposed prior to crack formation. Therefore, we do not believe the strained-intact state is likely to contribute to force-activated binding of ABPs. More directly, our docking simulations included several strained-intact interfaces in addition to a cracked interface, and mechanosensitive LIM domains were unlikely to bind them. For these reasons, we propose that binding to cracked interfaces may be a general mechanism for mediating force-activated interactions between actin filaments and mechanosensitive ABPs.

Self-healing. In the absence of applied strain, we find that damaged actin filaments spontaneously repair themselves on short timescales without the need for chaperone proteins (Fig. 3.11C). This self-healing behavior is intuitive because the cracked interface consists of a barbed end and pointed end of neighboring subunits in close proximity and proper orientation with respect to each other. Given that barbed end elongation is diffusion limited, two nearby subunits oriented favorably would be expected to establish stable inter-subunit contacts quickly.

The fact that the D-loop of subunit i becomes almost as accessible at cracked interfaces as fragmented ones is intriguing (Fig. 3.3B and C). As proposed based in an earlier study (21), this suggests that the MICAL redox enzyme could access and oxidize M44 and M47 in the central D-loop, introducing a post-translational modification that favors disassembly to residues that are typically buried in intact interfaces. This chemical modification may interfere with the rapid self-healing behavior we observe in all-atom MD.

LIM. We report that LIM domains bind to cracked interfaces. This is consistent with experimental evidence that mechanosensitive LIM domains specifically recognize strained actin filaments (13-15). Furthermore, we observe two non-mutually exclusive binding sites at a single cracked interface. This result suggests a potential mechanism for why three or more LIM domains in tandem separated by 7-8 amino acid linkers was necessary for mechanosensitivity for the vast majority of LIM domain proteins (14). First, the ~4 nm separation between crack sites 1 and 2 is consistent with the separation between LIM domains in predicted structures by AlphaFold2, indicating a single LIM-containing protein could have multiple domains bound simultaneously at one cracked interface. Therefore, when one LIM domain is bound, unbound tandem LIM domains undergo tethered diffusion near a second LIM-binding site, boosting the avidity of the overall binding interaction (Fig. 3.11D). By tuning the linker lengths, the diffusive search is better

constrained. Secondly, when LIM domains are bound to a cracked interface and the filament remains under tension, we find that crack site 2 can become exposed on the opposite protofilament strand prior to fragmentation. By having free LIM domains undergoing tethered diffusion, a single LIM-containing protein bound to the crack on one protofilament can quickly associate with the newly exposed crack on the opposite protofilament strand, allowing the LIM-containing protein to effectively wrap around the filament and reinforce lateral connections (Fig. 3.11E). As this process repeats, cracked interfaces stabilized by LIM domains may propagate along the filament, which may explain the spreading of LIM domains on actin filaments *in vitro* (13).

We find that LIM domains bound to the crack substantially prolongs the time before damaged actin filaments fragment. In addition to stabilizing individual filaments, this helps to maintain intact actin filament networks in two ways. First, this prolongs the period that LIM domains can signal to repair proteins that the filament is damaged, increasing the likelihood that repair occurs prior to fragmentation. Second, physiological strains may be intermittent in nature, meaning if LIM domains stabilize filaments during periods of highest strain that otherwise would have resulted in fragmentation, then the filament may not be subjected to strains likely to lead to rupture again.

Impact of the nucleotide state. We used actin filaments in the ADP nucleotide state, as this represents the most aged filaments and likely matches the nucleotide state of the actin filaments in the *in vitro* experiments that inspired this work. It would be interesting to investigate whether the observations we have made here are modulated by the nucleotide state of actin. For example, if the prevalence that Y169 is in the flipped orientation is a function of ATP-hydrolysis and inorganic phosphate release, this likely in turn alters the prevalence of filament cracking for filaments in these nucleotide states. Given that ADP-actin filaments are less stable than ATP-actin

filaments (24-26), yet structures of F-actin in all nucleotide states are nearly identical (27), perhaps differences in dynamics and prevalence of rare states, such as Y169's flipping, can explain the observed differences in filament stability.

Cryo-EM. We predict that resolving cracks using cryo-EM will be difficult. Cracks are rare, transient events. Given that cryo-EM depends on the averaging over many observations of roughly the same structure, collecting a large number of micrographs of cracked actin filaments could pose a significant challenge. Additionally, although the separation between subunits at cracked interfaces is noticeable in atomistic MD simulations, this separation at the EM micrograph level is likely to be very subtle, and identifying these occurrences will pose another challenge.

A recent cryo-EM study reported the structure of bent actin filaments (12). At the subunit level, the changes with respect to unstrained filaments were subtler than the crack we observed in MD simulations. We believe that the structures solved by cryo-EM are most likely akin to the strained-intact state that we describe in this manuscript. This would be the much more common state for interfaces to be in in EM micrographs and displays much more subtle changes to the filament surface.

However, cracked interfaces with LIM domains present may prove easier to identify. For one, these structures are longer-lived than cracked interfaces with no LIM domains bound, so they will likely be better represented in the dataset. Additionally, the presence of bound LIM domains may aid in the identification of these structures in EM micrographs, especially if LIM domains bind to cracked interfaces at multiple neighboring interfaces and wrap around the filament.

Methodological considerations. We set out to observe the fragmentation of actin filaments on MD timescales, typically limited to hundreds of nanoseconds to microseconds for

large, multiprotein systems. Therefore, we applied tensions on the order of hundreds of piconewtons, which is higher than physiological tensions. However, we are confident that our major conclusions are relevant at lower forces. First, Y169 flipping was observed in our control simulations in which no tension was applied. Tension increased the rate at which Y169 flipped and resulted in the interface breaking, but it was not required for flipping to occur. Second, although we had not predicted the metastable cracked state before performing these simulations, it is intuitive in hindsight and should be relevant across all tensions. Actin is a double helix composed of two protofilament strands. As long as both protofilaments do not break at neighboring interfaces at the exact same time, cracks will form. The physiological relevance of the intermediate cracked state depends on how long cracks remain metastable, and it is clear from our data that cracks last longer, and so would be even more relevant, at lower tensions. Additionally, cracks in actin filaments are reminiscent of the physiologically relevant damaged states reported for other biological polymers such as microtubules and DNA (19, 20).

However, it is possible that the relatively high tensions that we applied here obscure the existence of additional steps on the fragmentation pathway (i.e., these steps did not have enough time to become noticeable). With the lowest tension that we observed fragmentation with, 250 pN, crack site 2 became exposed before crack site 1. It seems plausible that at lower tensions, crack site 2 consistently becomes exposed first, as the exposure of crack site 1 is limited by the flip of Y169. Importantly, we applied strain using constant force, which is an important choice for this and any similar study. Constant velocity pulling schemes will not reveal metastable states, as force is increased on-the-fly to push past stable states.

Additionally, we applied tensile strains. We believe our findings under these conditions are relevant to other modes of strain, which at the scale of an individual interface likely appear very similar to tension (e.g., an out-of-equilibrium separation between neighboring subunits). In support

of this, mesoscale modeling of actin filaments indicated that strain is concentrated under a variety of modes of applied force (e.g., bending, compression, tension, twisting)) (21). We propose this localized strain under other types of mechanical strain also leads to the same metastable cracking behavior observed in our all-atom MD simulations. However, further studies may investigate the differences that arise from different modes of applying force.

Docking simulations have important limitations. In particular, molecules are treated as rigid bodies, so flexible linkers or conformational changes upon binding are not accurately reflected (22). For this reason, we used the structured individual LIM domains instead of tandem LIM domains separated by flexible linkers as the ligands for our docking simulations, and focused on conclusions that were common among the 43 LIM domain sequences we tested.

3.4 Methods

METHODS

MD simulations of the actin 13-mer: We used the 13-mer actin filament system in the ADP-state from Zsolnay PNAS 2020 (16) with an updated Charmm36m force field (28). Briefly, we patterned the ADP-F-actin subunits from PDB 6DJO (9) according to the reported rise and twist values and included waters near the catalytic center from previously equilibrated simulations of actin filaments. We used the autosolvate and autoionize plugins in VMD (29) to construct a 100 mM KCl solvent box with a minimum of 2.2 nm of TIP3P water separating the protein from its periodic image. We then performed sequential energy minimizations using NAMD (30) with a 10 kcal $mol^{-1}Å^{-2}$ harmonic constraint on 1) everything except buffer; 2) everything except buffer and protein sidechains; 3) only the bound nucleotide and Mg^{2+}; and 4) only Mg^{2+}. The system underwent a 1-ns heating protocol bringing the temperature from 0 to 310 K under constraint

selection 1). This was followed by a series of five 400-ps constrained equilibrations with the force constant on constraint selection 1) being halved each iteration (k = 10, 5, 2.5, 1.25, 0.625 kcal $mol^{-1}Å^{-2}$) followed by a sixth constrained equilibration of k = 0.1 kcal $mol^{-1}Å^{-2}$ lasting 1 ns. The system was equilibrated without constraints for 60 ns.

Production runs were performed on Department of Defense High Performance Computing systems using GROMACS version 2019.1(31) in the isothermal-isobaric (constant NPT) ensemble with v-rescale temperature coupling, Parinello-Rahman pressure coupling, and the leapfrog integrator. The particle mesh Ewald sum method was used to calculate electrostatic interactions with a cutoff of 1.2 nm. Equal and opposite forces were applied on the Cα center of mass of the three terminal subunits at the barbed and pointed ends via a constant force scheme using the GROMACS pull code. The direction of the force was along the axis of the filament throughout the duration of the simulation.

Docking simulations: We used the ClusPro2.0 web server to perform the docking simulations (17, 22). Briefly, for each simulation run, a receptor and ligand structure are given as input. The ligand molecule is rotated 70,000 times, and each rotation is translated to fully explore the receptor, generating ~10^9 unique orientations of the ligand with respect to the receptor. Each combination of rotation and translation is scored based on an estimate of the binding energy. The 1,000 orientations with the best score are selected from the original ~10^9 and are grouped into clusters of binding poses with an RMSD relative to one another less than 9 Å. Clusters are ranked according to the number of the top 1,000 poses that they contain. This typically yields 15 to 30 binding poses with vastly different cluster sizes. We determined the location of each output pose on the filament (e.g., barbed end, pointed end, cracked interface, side) and weighted them according to the cluster size (Fig. 3.8A). We used the experimental result that mechanosensitive LIM domains do not appear enriched at filament ends to further filter the LIM docking output by accepting only poses

ranked more highly than the highest ranked filament end-binding pose (Fig. 3.8B). This yielded a filtered set of binding poses for each of the 43 LIM domains tested (Fig. 3.8C). We also used the following PDB structures as non-LIM ligands: profilin: 2PAV; cofilin: 6UBY; α-catenin: 6UPV; metavinculin: 6UPW; Lifeact: 7AD9; CapZ: 7PDZ; actin: 1NWK (6, 32-35).

MD simulations of actin 7-mer: To compare the stability of cracked actin filaments with and without bound LIM domains, we constructed an actin filament system consisting of 7 actin subunits with a cracked interface in the middle of the filament. For simulations with LIM domains present, we included the top pose of the first LIM domain of testin at both crack site 1 and crack site 2. Zn^{2+} ions were positioned by aligning the Alphafold2 structure to the solution NMR structure of the third LIM domain of FHL2 (PDB 2D8Z). Coordinating cysteines were in the deprotonated state. The minimization, heating, equilibration, and force-application protocol was the same as described for the actin 13-mer filament system.

Analysis of MD simulations and docking structures: We report a distance between longitudinal neighboring subunits, the subunit-subunit distance, or ss_{dist}, which is the distance between the center of mass of Cα atoms of subunits i and i-2 (Fig. 3.1A). Interfaces were considered cracked when the 2-ns moving average of the ss_{dist} exceeded 6.3 nm. Filaments were considered fragmented when the second time derivative of the filament end-to-end distance (i.e., its acceleration) reached a maximum, indicating all connections had been severed. The end-to-end distance was calculated using the center of mass of Cα atoms of the three terminal subunits at each filament end. Accessible surface area (ASA) calculations were performed in VMD using a probe radius of 4 Å to estimate the filament surface relevant for protein-binding. MDAnalysis was used to construct contact maps (36). Visualizations were performed in VMD and Chimera (29, 37).

Table 3.1. Simulations performed in Chapter 3.

Simulation number	Initial structure	Number of actin subunits	Tension (pN)	Replicate number	Duration (ns)	Final state
1	6DJO	13	0	1	373	Intact
2	6DJO	13	0	2	988	Intact
3	6DJO	13	0	3	580	Intact
4	6DJO	13	200	1	1,091	Intact
5	6DJO	13	200	2	300	Intact
6	6DJO	13	400	1	810	Intact
7	6DJO	13	400	2	400	Intact
8	6DJO	13	500	1	91	Fragment
9	6DJO	13	500	2	123	Fragment
10	6DJO	13	500	3	340	Fragment
11	6DJO	13	500	4	307	Fragment
12	6DJO	13	500	5	251	Fragment
13	6DJO	13	500	6	510	Fragment
14	6DJO	13	500	7	180	Fragment
15	6DJO	13	500	8	110	Fragment
16	6DJO	13	550	1	200	Fragment
17	6DJO	13	550	2	100	Fragment

Table 3.1 continued.

18	6DJO	13	550	3	80	Fragment
19	6DJO	13	550	4	194	Fragment
20	6DJO	13	550	5	72	Fragment
21	6DJO	13	600	1	40	Fragment
22	6DJO	13	600	2	82	Fragment
23	6DJO	13	600	3	87	Fragment
24	6DJO	13	600	4	30	Fragment
25	6DJO	13	600	5	40	Fragment
26	Cracked	13	0	1	57	Intact
27	Cracked	13	0	2	142	Intact
28	Cracked	13	0	3	101	Intact
29	Cracked	13	300	1	171	Fragment
30	Cracked	13	300	2	141	Fragment
31	Cracked	13	300	3	55	Fragment
32	Cracked	13	300	4	358	Fragment
33	Cracked	13	300	5	60	Fragment
34	Cracked	13	350	1	30	Fragment
35	Cracked	13	350	2	70	Fragment
36	Cracked	13	350	3	70	Fragment
37	Cracked	13	350	4	100	Fragment

Table 3.1 continued.

38	Cracked	13	400	1	40	Fragment
39	Cracked	13	400	2	20	Fragment
40	Cracked	13	400	3	27	Fragment
41	Cracked	13	400	4	40	Fragment
42	Cracked	13	400	5	40	Fragment
43	Cracked	13	450	1	20	Fragment
44	Cracked	13	450	2	30	Fragment
45	Cracked	13	450	3	20	Fragment
47	Cracked	13	500	1	30	Fragment
47	Cracked	13	500	2	18	Fragment
48	Cracked	13	550	1	20	Fragment
49	Cracked	13	550	2	20	Fragment
50	Cracked	13	550	3	20	Fragment
51	Cracked	13	600	1	11	Fragment
52	Cracked	13	600	2	10	Fragment
53	Cracked	13	600	3	10	Fragment
54	Strained-intact	13	500	1	64	Fragment
55	Strained-intact	13	550	1	30	Fragment
56	Cracked	7	250	1	70	Fragment
57	Cracked	7	250	2	20	Fragment

Table 3.1 continued.						
58	Cracked	7	250	3	50	Fragment
59	Cracked	7	250	4	50	Fragment
60	Cracked	7	250	5	50	Fragment
61	Cracked	7	500	1	11	Fragment
62	Cracked	7	500	2	10	Fragment
63	Cracked	7	500	3	5	Fragment
64	Cracked+LIM[a]	7	250	1	1,479	Fragment
65	Cracked+LIM	7	250	2	2,430	Fragment
66	Cracked+LIM	7	250	3	370	Fragment
67	Cracked+LIM	7	500	1	21	Fragment
68	Cracked+LIM	7	500	2	15	Fragment
69	Cracked+LIM	7	500	3	15	Fragment
Total	—	—	—	—	**13,800**	—

a. System composed of a cracked actin 7mer with two copies of the first LIM domain of testin bound at both crack sites 1 and 2.

3.5 References

1. C. A. Anderson, D. R. Kovar, M. L. Gardel, J. D. Winkelman, LIM domain proteins in cell mechanobiology. *Cytoskeleton (Hoboken)* **78**, 303-311 (2021).
2. A. Jégou, G. Romet-Lemonne, Mechanically tuning actin filaments to modulate the action of actin-binding proteins. *Curr Opin Cell Biol* **68**, 72-80 (2021).
3. F. Martino, A. R. Perestrelo, V. Vinarský, S. Pagliari, G. Forte, Cellular Mechanotransduction: From Tension to Function. *Front Physiol* **9**, 824 (2018).
4. V. I. Risca *et al.*, Actin filament curvature biases branching direction. *Proc Natl Acad Sci U S A* **109**, 2913-2918 (2012).
5. N. G. Pandit *et al.*, Force and phosphate release from Arp2/3 complex promote dissociation of actin filament branches. *Proc Natl Acad Sci U S A* **117**, 13519-13528 (2020).
6. L. Mei *et al.*, Molecular mechanism for direct actin force-sensing by α-catenin. *Elife* **9** (2020).
7. K. Hayakawa, H. Tatsumi, M. Sokabe, Actin filaments function as a tension sensor by tension-dependent binding of cofilin to the filament. *J Cell Biol* **195**, 721-727 (2011).
8. H. Wioland, A. Jegou, G. Romet-Lemonne, Torsional stress generated by ADF/cofilin on cross-linked actin filaments boosts their severing. *Proc Natl Acad Sci U S A* **116**, 2595-2602 (2019).
9. S. Z. Chou, T. D. Pollard, Mechanism of actin polymerization revealed by cryo-EM structures of actin filaments with three different bound nucleotides. *Proc Natl Acad Sci U S A* **116**, 4265-4274 (2019).
10. F. Merino *et al.*, Structural transitions of F-actin upon ATP hydrolysis at near-atomic resolution revealed by cryo-EM. *Nat Struct Mol Biol* **25**, 528-537 (2018).
11. W. Oosterheert, B. U. Klink, A. Belyy, S. Pospich, S. Raunser, Structural basis of actin filament assembly and aging. *Nature* **611**, 374-379 (2022).
12. M. J. Reynolds, C. Hachicho, A. G. Carl, R. Gong, G. M. Alushin, Bending forces and nucleotide state jointly regulate F-actin structure. *Nature* **611**, 380-386 (2022).
13. X. Sun *et al.*, Mechanosensing through Direct Binding of Tensed F-Actin by LIM Domains. *Dev Cell* **55**, 468-482.e467 (2020).
14. J. D. Winkelman, C. A. Anderson, C. Suarez, D. R. Kovar, M. L. Gardel, Evolutionarily diverse LIM domain-containing proteins bind stressed actin filaments through a conserved mechanism. *Proc Natl Acad Sci U S A* **117**, 25532-25542 (2020).
15. S. Sala, P. W. Oakes, Stress fiber strain recognition by the LIM protein testin is cryptic and mediated by RhoA. *Mol Biol Cell* **32**, 1758-1771 (2021).
16. V. Zsolnay, H. H. Katkar, S. Z. Chou, T. D. Pollard, G. A. Voth, Structural basis for polarized elongation of actin filaments. *Proc Natl Acad Sci U S A* **117**, 30458-30464 (2020).

17. D. Kozakov *et al.*, The ClusPro web server for protein-protein docking. *Nat Protoc* **12**, 255-278 (2017).

18. J. Jumper *et al.*, Highly accurate protein structure prediction with AlphaFold. *Nature* **596**, 583-589 (2021).

19. M. Gazzola *et al.*, Microtubules self-repair in living cells. *Curr Biol* **33**, 122-133.e124 (2023).

20. J. Aymami *et al.*, Molecular structure of nicked DNA: a substrate for DNA repair enzymes. *Proc Natl Acad Sci U S A* **87**, 2526-2530 (1990).

21. A. C. Schramm, G. M. Hocky, G. A. Voth, J. L. Martiel, E. M. De La Cruz, Plastic Deformation and Fragmentation of Strained Actin Filaments. *Biophys J* **117**, 453-463 (2019).

22. I. T. Desta, K. A. Porter, B. Xia, D. Kozakov, S. Vajda, Performance and Its Limits in Rigid Body Protein-Protein Docking. *Structure* **28**, 1071-1081.e1073 (2020).

23. N. O. Glenn *et al.*, The W-loop of alpha-cardiac actin is critical for heart function and endocardial cushion morphogenesis in zebrafish. *Mol Cell Biol* **32**, 3527-3540 (2012).

24. R. Dominguez, K. C. Holmes, Actin structure and function. *Annu Rev Biophys* **40**, 169-186 (2011).

25. Z. A. Durer *et al.*, Structural states and dynamics of the D-loop in actin. *Biophys J* **103**, 930-939 (2012).

26. H. Isambert *et al.*, Flexibility of actin filaments derived from thermal fluctuations. Effect of bound nucleotide, phalloidin, and muscle regulatory proteins. *J Biol Chem* **270**, 11437-11444 (1995).

27. R. Dominguez, Nucleotide-dependent conformational changes in the actin filament: Subtler than expected. *Proc Natl Acad Sci U S A* **116**, 3959-3961 (2019).

28. A. Croitoru *et al.*, Additive CHARMM36 Force Field for Nonstandard Amino Acids. *J Chem Theory Comput* **17**, 3554-3570 (2021).

29. W. Humphrey, A. Dalke, K. Schulten, VMD: visual molecular dynamics. *J Mol Graph* **14**, 33-38, 27-38 (1996).

30. L. Kalé *et al.*, NAMD2: Greater Scalability for Parallel Molecular Dynamics. *Journal of Computational Physics* **151**, 283-312 (1999).

31. M. J. Abraham *et al.*, GROMACS: High performance molecular simulations through multi-level parallelism from laptops to supercomputers. *SoftwareX* **1-2**, 19-25 (2015).

32. A. Belyy, F. Merino, O. Sitsel, S. Raunser, Structure of the Lifeact-F-actin complex. *PLoS Biol* **18**, e3000925 (2020).

33. P. Graceffa, R. Dominguez, Crystal structure of monomeric actin in the ATP state. Structural basis of nucleotide-dependent actin dynamics. *J Biol Chem* **278**, 34172-34180 (2003).

34. A. R. Huehn *et al.*, Structures of cofilin-induced structural changes reveal local and asymmetric perturbations of actin filaments. *Proc Natl Acad Sci U S A* **117**, 1478-1484 (2020).

35. J. Funk *et al.*, A barbed end interference mechanism reveals how capping protein promotes nucleation in branched actin networks. *Nat Commun* **12**, 5329 (2021).

36. N. Michaud-Agrawal, E. J. Denning, T. B. Woolf, O. Beckstein, MDAnalysis: a toolkit for the analysis of molecular dynamics simulations. *J Comput Chem* **32**, 2319-2327 (2011).

37. E. F. Pettersen *et al.*, UCSF Chimera--a visualization system for exploratory research and analysis. *J Comput Chem* **25**, 1605-1612 (2004).

Chapter 4: Formin Cdc12's specific actin assembly properties are tailored for cytokinesis in fission yeast

Preface

The work presented in this chapter was performed in collaboration with Kaitlin Homa, Tamara Bidone, Erin Neidt, Meghan O'Connell, Caitlin Anderson, Gregory Voth, and David Kovar. The experiments presented in Figures 4.3, 4.6, 4.7, 4.8, 4.9, 4.10, 4.11, and 4.12 were performed by Kaitlin Homa with assistance from Erin Neidt, Meghan O'Connell, and Caitlin Anderson. I developed the simulation code and performed the simulations with Tamara Bidone. I developed the analysis code and performed the analysis shown in Figures 4.1, 4.2, 4.4, and 4.5. This work was published in Biophysical Journal in August 2021 (doi: 10.1016/j.bpj.2021.06.023)

Abstract

Formins generate unbranched actin filaments by a conserved, processive actin assembly mechanism. Most organisms express multiple formin isoforms that mediate distinct cellular processes and facilitate actin filament polymerization by significantly different rates, but how these actin assembly differences correlate to cellular activity is unclear. We used a computational model of fission yeast cytokinetic ring assembly to test the hypothesis that particular actin assembly properties help tailor formins for specific cellular roles. Simulations run in different actin filament nucleation and elongation conditions revealed that variations in formin's nucleation efficiency critically impact both the probability and timing of contractile ring formation. To probe the physiological importance of nucleation efficiency, we engineered fission yeast formin chimera strains in which the FH1FH2 actin assembly domains of full-length cytokinesis formin Cdc12 were replaced with the FH1FH2 domains from functionally and evolutionarily diverse formins with

significantly different actin assembly properties. Although Cdc12 chimeras generally support life in fission yeast, quantitative live-cell imaging revealed a range of cytokinesis defects from mild to severe. In agreement with the computational model, chimeras whose nucleation efficiencies are least similar to Cdc12 exhibit more severe cytokinesis defects, specifically in the rate of contractile ring assembly. Together, our computational and experimental results suggest that fission yeast cytokinesis is ideally mediated by a formin with properly tailored actin assembly parameters.

Significance Statement

Cytokinesis, the physical separation of a mother cell into daughter cells, is a critical last step of the cell division cycle. Defects can negatively impact development or lead to the proliferation of cancer. The actin assembly factor formin facilitates cytokinetic contractile ring formation in eukaryotic cells by determining both how often and how fast actin filaments assemble. We investigated the importance of formin's specific actin assembly properties on cytokinesis in fission yeast, a model for cell division. By altering formin properties using a computational model and by engineering mutant fission yeast strains, we conclude that efficient actin filament nucleation is the most critical factor for proper contractile ring formation.

4.1 Introduction

Formins (formin homology proteins) are a family of large, highly conserved proteins that nucleate actin filaments (F-actin) and remain processively associated with their barbed ends to significantly increase the elongation rate for a variety of fundamental cellular processes, including polarization, motility, division, and adhesion (Breitsprecher and Goode, 2013; Courtemanche, 2018). Formins are characterized by two highly conserved formin homology (FH) domains that nucleate and elongate unbranched F-actin. The FH2 domain is a tethered, head-to-tail dimer that

nucleates and then processively encircles the growing F-actin barbed end (Otomo et al., 2005), while the unstructured FH1 domain binds profilin-actin via its multiple proline rich regions and delivers it to the FH2-bound barbed end to facilitate rapid elongation (Courtemanche, 2018; Kovar and Pollard, 2004; Paul and Pollard, 2009; Romero et al., 2004; Vavylonis et al., 2006). The conserved FH1FH2 domains are flanked by less well-conserved regulatory domains, which facilitate the activation of many formins at the correct time and place (Breitsprecher and Goode, 2013). Additionally, some formin isoforms carry out noncanonical functions, such as severing F-actin to promote depolymerization, generating F-actin bundles, and binding directly to microtubules to coordinate crosstalk between the actin and microtubule cytoskeletons (Courtemanche, 2018).

Most organisms express multiple formin isoforms, from two in budding yeast, three in fission yeast, seven in nematode worms, ~15 in mammals, to more than 20 in plants (Higgs and Peterson, 2005; Rivero et al., 2005; Schönichen and Geyer, 2010). Despite having well-conserved structural folds and general actin assembly mechanisms, distinct formin isoforms are required for different cellular processes in many cell types. For example, each of the three fission yeast formins assembles actin filaments for a specific F-actin network (Kovar et al., 2011): For3, polarizing actin cables (Feierbach and Chang, 2001; Nakano et al., 2002); Cdc12, the contractile ring of dividing cells (Chang et al., 1997); Fus1, the fusion focus during mating (Petersen et al., 1998, 1995). While regulation via activation at the right time and place has been established to be critical for the functional specificity of formin isoforms (Breitsprecher and Goode, 2013), it is also possible that a formin's particular actin assembly properties are also important (Vidali et al., 2009). In vitro measurements reveal that many formins have significantly different actin assembly properties, such as F-actin nucleation efficiency, barbed end elongation rate, and barbed end dissociation rate (Goode and Eck, 2007; Kovar et al., 2006). Consistent with this possibility, we previously

determined that the actin assembly properties of the three fission yeast formins (For3, Cdc12, and Fus1) vary widely (Table 4.1) (Scott et al., 2011), suggesting that a formin's specific properties might also be tailored for its cellular role. However, the extent to which each property contributes to the assembly of particular F-actin networks in vivo is less clear.

Table 4.1: In vitro actin assembly properties of formins used to generate formin chimeras[a]

Formin	Nucleation Efficiency	Elongation Rate (subunits sec^{-1} μM^{-1})	Dissociation Rate (sec^{-1})
Fission yeast Cdc12	1 filament per 2-3 dimers (Neidt et al., 2008; Scott et al	10-12 (Kovar et al., 2006; Neidt et al., 2008; Scott et al., 2011)	$4.7\text{-}7.0x10^{-5}$ (Neidt et al., 2008; Scott et al., 2011)
Fission yeast For3	1 filament per 170 dimers (Scott et al.,	10 (Scott et al., 2011)	$3.6x10^{-5}$ (Scott et al., 2011)
Budding yeast Bni1	1 filament per ~20 dimers (Kovar and Pollard, 2004; Moseley	20-25 (Moseley and Goode, 2005; (Kovar et al., 2006))	$8x10^{-4}$ (Kovar and Pollard, 2004)
Mouse Dia2	1 filament per ~8 dimers (Li and Higgs,	12 (Kovar et al., 2006)	$1.3x10^{-4}$ (Kovar et al., 2006)
Worm CYK-1	1 filament per 25 dimers (Neidt et al.,	~60 (Neidt et al., 2008; 2009)	$3.9x10^{-3}$ (Neidt et al., 2008)
Fission yeast Fus1	1 filament per 2 dimers (Scott et al.,	5 (Scott et al., 2011)	$6.5x10^{-4}$ (Scott et al., 2011)

Table 4.1. *In vitro* actin assembly properties of formins used to generate formin chimeras

[a]Formin nucleation efficiency (filaments per dimer), barbed end elongation rate (in the presence of profilin), and dissociation rate from the barbed end were determined previously with in vitro biochemical assays.

Cytokinesis, the physical separation of a mother cell into two daughter cells, is the final step of the cell cycle during which cells assemble a contractile ring of bundled, anti-parallel actin filaments and type II myosin motors. The molecular mechanism of cytokinesis and the role of formin Cdc12 are well established in fission yeast, providing an ideal system to investigate whether and how a formin's particular actin assembly characteristics are suited for its cellular role (Pollard and Wu, 2010). Fission yeast contractile ring assembly is accomplished via a primary mechanism

known as Search, Capture, Pull, Release (SCPR). In SCPR, several conserved cytokinesis proteins, including formin Cdc12 and type II myosin Myo2, are associated with ~140 pre-ring cytokinesis nodes that are cortically distributed around the cell middle (Fig. 4.1A) (Laplante et al., 2016; Lee et al., 2012; Vavylonis et al., 2008; Wu et al., 2006). Filaments nucleated and assembled by Cdc12, which is not thought to be canonically autoinhibited (Yonetani et al., 2008), are subsequently captured by Myo2 on an adjacent node (Search and Capture). Myo2 then exerts a pulling force on the Cdc12-assembled actin filament (Pull), bringing the two nodes closer together. These node-node connections are lost via severing from cofilin (Release), and the search phase starts again (Fig. 4.1A). After multiple rounds of search, capture, pull, and release, actin filaments coalesce into a contractile ring (Vavylonis et al., 2008; Wu et al., 2006). The SCPR model provides a solid framework for examining the importance of formin Cdc12's specific actin assembly properties in the assembly of a contractile ring.

Here, we first used a computational 3D SCPR model to characterize how formin-mediated actin filament nucleation efficiency and elongation rate affect cytokinetic ring formation. Our simulations predicted that both properties are important, but changes in formin nucleation efficiency have the largest impact on the timing and probability of contractile ring formation. We then tested the physiological importance of formin's actin filament nucleation efficiency and elongation rate using in vivo experiments. We developed formin chimera strains that express engineered formin chimeras in which the FH1FH2 domains of the cytokinesis formin Cdc12 were replaced with the FH1FH2 domains of functionally, evolutionarily, and biochemically diverse formins from different organisms. Quantitative imaging and analysis of the formin chimera cells reveal that formin-mediated cytokinesis in fission yeast is robust, but support the modeling predictions that Cdc12's nucleation efficiency has the largest impact on contractile ring assembly rate.

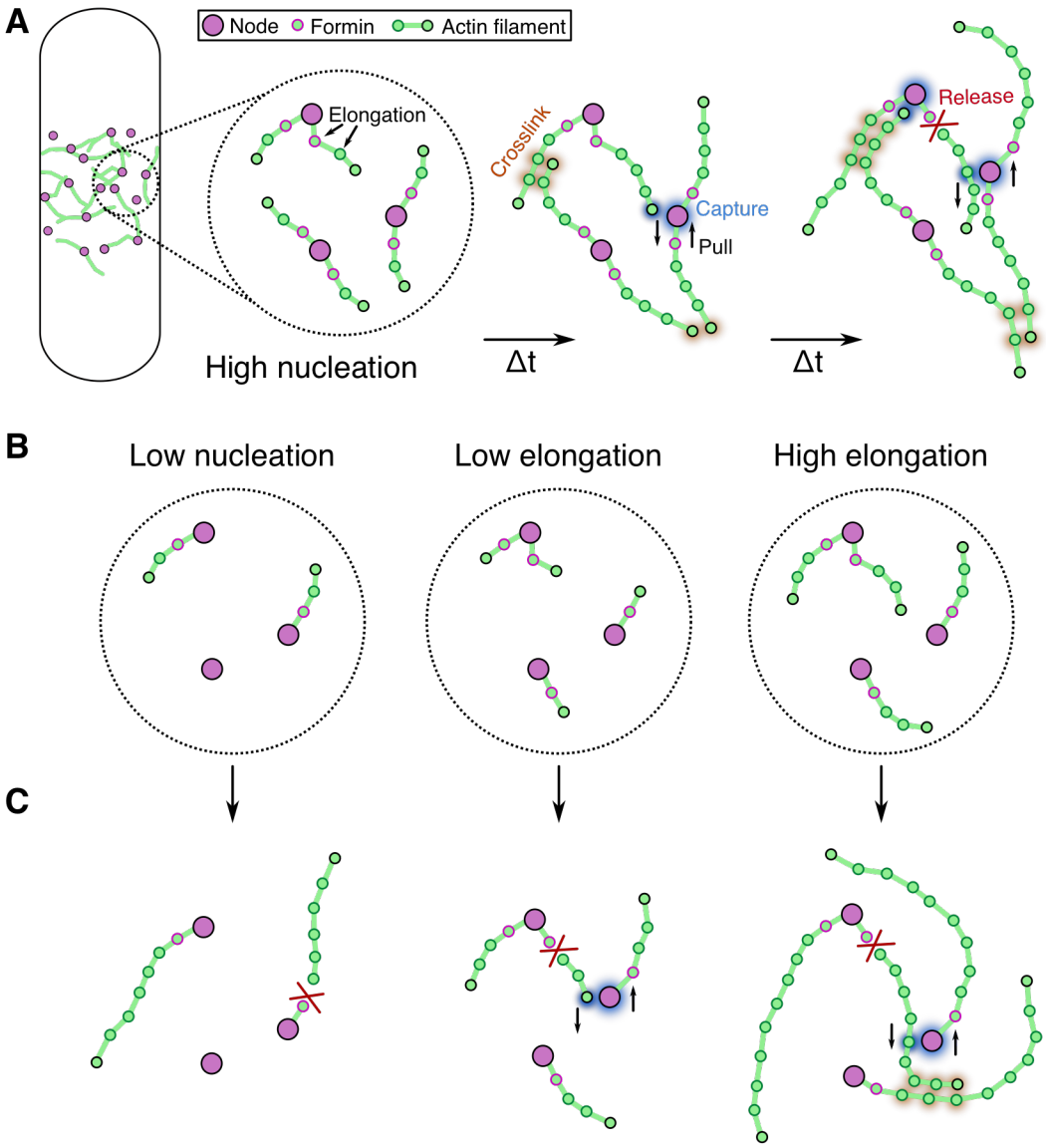

Figure 4.1. Overview of 3D SCPR computational model.
(A) Cartoon showing three time points of the Search, Capture, Pull, and Release mechanism used in the model. Under high nucleation wild-type (WT) conditions, approximately two actin filaments (string of green beads) elongate from formin beads connected to pre-ring cytokinesis nodes (purple). The pointed end bead is highlighted in black. These elongating filaments may be captured by myosin on adjacent nodes, which exerts a pulling force that brings two nodes closer together. When actin filaments are severed, the connection between two nodes is broken. See Materials and Methods for a detailed summary of the model. (B) We varied the rates of formin-mediated nucleation and elongation of actin filaments. Low nucleation, low elongation, and high elongation conditions are illustrated at early times in the simulation. (C) Illustrations of the dominant outcomes of non-WT formin-mediated nucleation and elongation properties. Low nucleation (left) results in few actin filaments that fail to be connect nodes. Low elongation (middle) produces short filaments that fail to form a continuous ring. High elongation (right) results in ectopic F-actin that fails to organize nodes favorably for ring formation.

4.2 Materials and Methods

SCPR model of ring assembly. To test the individual and combined effects of formin's actin assembly properties on fission yeast cytokinetic ring assembly, including actin filament nucleation and elongation rate, we extended a 3D model based on the SCPR mechanism (Bidone et al., 2014). The model implements a Brownian Dynamics algorithm within a domain that mimics shape, dimensions and other physical properties of a fission yeast cell (Fig. 4.1). By integrating the *Langevin* equation of motion over time (Nedelec and Foethke, 2007; Pasquali et al., 2001), the model reproduces the time evolution of actin filament nucleation, elongation, and severing of the SCPR mechanism, using explicit pre-ring cytokinesis nodes containing myosin and formin (Bidone et al., 2014).

The computational domain is a cylinder of radius 1.74 μm and length 13 μm, reproducing the dimensions of a fission yeast cell. Membrane-bound nodes are represented as explicit point particles that can move along the membrane. They are initially distributed according to a Gaussian distribution with mean centered along the domain long axis and standard deviation of 0.9 μm. Formins are represented as explicit point particles, bound to nodes, that nucleate and elongate actin filaments. The number of formins per node is selected depending on nucleation efficiency, which controls the total number of filaments, *N*. Formin-mediated actin elongation rate is assigned as a rate at which actin beads are added to the filament's barbed end, in contact with formin beads at the node. We simulated both conditions of fixed elongation rate and including formin mechanoinhibition reported in (Zimmermann et al., 2017), whereby elongation rate was reduced to ~30% of uninhibited values. Actin filaments are represented as series of beads and springs that form semi-flexible polymers with persistence length 10 μm (Alberts, 2009; Isambert et al., 1995; Tang et al., 2014). Actin and formin beads experience an effective drag of $\zeta_b = 0.108$ pN s/μm to account for cytoplasmic viscosity. When an actin bead comes within 0.1 μm of an adjacent node

(other than the one it originates from), a harmonic interaction is formed between them (parameter values are reported in Table 4.2). Nodes then exert 4 pN tension on captured beads in the direction of the pointed end, mimicking the power-stroke of myosin heads. The nodes experience an equal and opposite force, which generates sliding motion of the node along the membrane. Node movement is constrained by a membrane drag $\zeta_{node} = 400$ pN s/μm, mimicking cell membrane friction.

Table 4.2. List of reference model parameters used in simulations

Parameter	Description	Value	Unit
R	Rod-shaped domain radius	1.74	μm
l	Rod-shaped domain length	13	μm
n	Number of nodes	65 or 140	
N	Number of filaments	30-130 or 280	
dt	Simulation timestep	4×10^{-4}	s
v_{pol}	Actin polymerization rate	0.04-0.25	μm/s
τ	Actin filament lifetime	16	s
l_p	Persistence length of actin filaments	10	μm
l_0	Equilibrium distance between filament beads	0.1	μm
k	Spring constant between filament beads	100	pN/μm
ζ_b	Filament bead drag coefficient	0.108	pN s/μm
ζ_{node}	Node drag coefficient	400	pN s/μm
k_{crslnk}	Cross-linking spring constant between filaments	1	pN/ μm
r_{crslnk}	Threshold distance for cross-linking between filaments	0.1	μm
r_0	Equilibrium cross-linking length between filaments	0.03	μm
k_{formin}	Formin-node spring constant	100	pN/ μm
r_{formin}	Formin-node equilibrium length	0.05	μm
r_{node}	Node excluded volume radius	0.1	μm
2σ	Twice the standard deviation of Gaussian distribution	1.8	μm
F_{myo}	Node pulling force	4	pN
F_{rep}	Node repulsive force	50	pN
$F_{confinement}$	Node, actin filament bead and formin confining force	5	pN
F_{thresh}	Force threshold for polymerization inhibition	1	pN
r_{capt}	Node capture radius for actin filament beads	0.1	μm

$l_{node\text{-}filament}$	Equilibrium length between node and captured filament bead	0	μm
k_c	Spring constant between node and captured filament bead	2.5	pN/ μm
μ	Pulling force reduction factor (when filaments are crosslinked)	0.3	

Table 4.2 continued

Recent evidence suggests that there are 140 cytokinesis nodes in fission yeast (Laplante et al., 2016). Previous versions of the SCPR model have varied the number of nodes and reported that values greater than ~50 nodes all lead to comparable ring assembly kinetics (Vavylonis et al, 2008). We performed a subset of our simulations at both 65 and 140 nodes and observed that our conclusions are reproduced using either 65 or 140 nodes (Fig. 4.2). Therefore, we have used 65 nodes for simulations presented in the main text, which allowed a much larger exploration of parameter-space due to the increased computational efficiency.

When actin beads of different filaments come within 0.1 μm of each other, a harmonic interaction is also formed between them. The rest length is 0.03 μm and the stiffness is 1 pN/μm, mimicking the structural properties of the fission yeast contractile ring actin filament crosslinking protein Ain1 (Laporte et al., 2012).

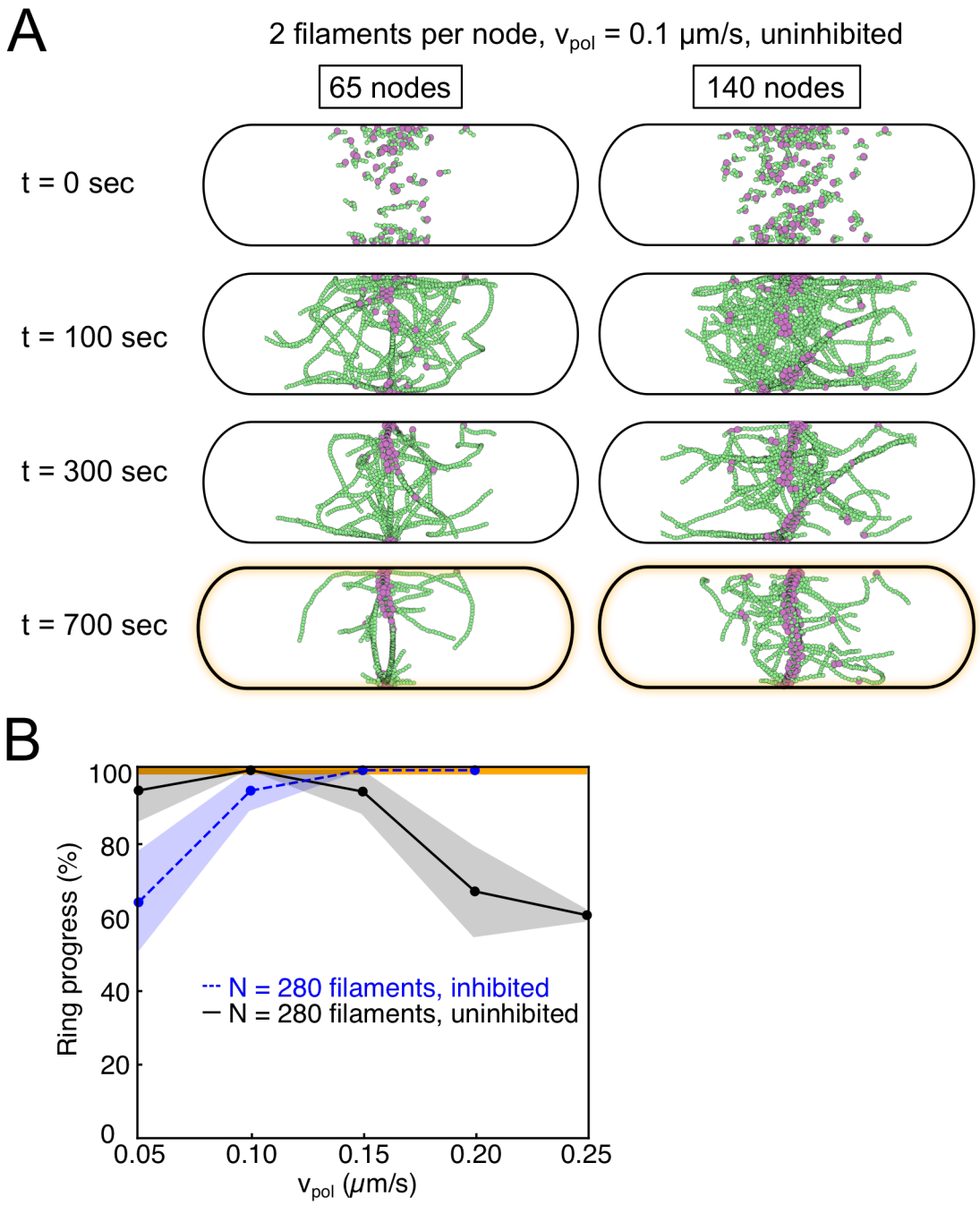

Figure 4.2. Comparison between simulations with 65 and 140 nodes.
(A) Snapshots depict the evolution of two simulations with 65 (left) or 140 (right) nodes, but otherwise equal parameters. Although there are clearly more nodes and filaments in the 140-node simulation, the phase of ring assembly at each time point is very similar. Yellow shading highlights ring formation in both simulations at t = 700 s. (B) The dependence of ring progress on vpol is shown at N = 280 and 140 nodes with and without mechanoinhibition. This figure is equivalent to Fig. 2B for the 65 node cases, and also illustrates that a wide range of vpol is favorable to ring assembly. Data points are averages of 5 independent runs and shading represents standard deviation.

The positions of both filament beads and nodes, $\boldsymbol{r_i}$ are updated at each time step of the simulation following the *Langevin* equation of motion (Nedelec and Foethke, 2007; Pasquali et al., 2001) with inertia neglected:

$$F_i = \zeta \frac{dr_i}{dt}$$

Where $\boldsymbol{F_i}$ is the total force acting on the particle and ζ is the drag coefficient. The force $\boldsymbol{F_i}$ acting on each particle is the 3D vector sum of a deterministic and stochastic force. In the case of filament beads, the deterministic force is the sum of crosslinking, bending, extension, myosin capturing, and myosin pulling interactions. For the nodes, the deterministic force comes from filament elongation at the node-bound formin sites, and node capturing and pulling. For both filament and formin beads, the stochastic force follows the fluctuation dissipation theorem:

$$\langle F_i^{thermal} F_i^{thermal} \rangle_{\alpha,\beta} = 2\left(\frac{k_\beta \mathrm{T}\xi}{dt}\right)\hat{I}_{\alpha,\beta}$$

Where $\hat{I}_{\alpha,\beta}$ is the second-order unit tensor (Pasquali et al., 2001). A detailed description of the model parameter values, actin, formin and node interactions, and algorithm implementation scheme are reported in Supplemental Methods and Table 4.2 and 4.3.

Table 4.3. Comparison of the extended 3D SCPR with previous SCPR models

	Domain	v_{pol}	Force-dependent inhibition of v_{pol}	F_{stoch}	τ	F_{node}/ζ_{node}	Crosslinking	l_0
Vavylonis, 2008	2D	0.2 μm/s	yes	no	20 s	0.02 μm/s	no	0.2 μm
Laporte, 2012	2D	0.1 μm/s	no	yes	20 s	0.02 μm/s	yes	0.2 μm
Bidone, 2014	3D	0.1 μm/s	no	yes	16 s	0.01 μm/s	yes	0.1 μm
Zimmerman, 2017	2D	0.2 μm/s	yes	yes	no	0.1 μm/s	no	0.25 μm
Extended 3D SCPR	3D	0.18 μm/s	yes	yes	16 s	0.01 μm/s	yes	0.1 μm

Simulations were analyzed using a continuous collective variable that estimates how ring-like the actin and node geometry are by taking into account the node broad band and continuity of actin beads around the midzone. This 'ring progress' collective variable is normalized between 0% and 100% such that 100% identifies fully formed rings. A complete description of this variable is provided in the Supplemental Methods. The ring progress value assigned to each simulation replicate was taken to be the maximum ring progress reached across all simulation frames. The first time point that reached 100% ring progress was recorded as the time to ring assembly.

Formin chimera strain construction. *cdc12* N-terminal sequence was amplified by PCR (iProof, Bio-Rad Laboratories) from wild-type *S. pombe* genomic DNA and cloned into pBluescript II KS (-) (Stratagene) using restriction enzymes XhoI and BamHI. Overlap PCR was used to link formin (FH1FH2) sequences from For3, Fus1, Bni1, mDia2, and CYK-1 to *cdc12* C-terminal sequences, followed by homologous recombination using the In-Fusion Advantage PCR Cloning Kit (Clontech, Mountain View, CA) into pBluescript already containing *cdc12* N-terminus, resulting in the *cdc12* chimera fragment *cdc12*(N)::formin(FH1FH2)::*cdc12*(C). PCR

amplifications of the *cdc12* promoter (1-700 bp upstream of the translation start site) from the wild-type *S. pombe* genome and monomeric GFP (mGFP) from the pSGP-572 vector were cloned into the *S. pombe* integration vector pJK210 (Keeney and Boeke, 1994) with restriction enzyme SacI. *Cdc12* chimeras were also cloned into pJK210 by In-Fusion downstream of the *cdc12* promoter and confirmed by sequencing.

Chimera formin constructs were integrated into the *ura4* locus under control of the *cdc12* promoter and tagged C-terminally with GFP to create pJK210-Pcdc12-cdc12(N-term)-formin(FH1FH2)-cdc12(C-term)-GFP::ura+ (Zimmermann et al., 2017). These strains, containing both integrated chimera formins and endogenous *cdc12,* were saved to perform the analysis seen in Fig. 4.3. For the remainder of the study, endogenous *cdc12* was deleted through Kan cassette gene replacement (Bähler et al., 1998), while markers for contractile rings (rlc1-tdTomato-natMX6) and spindle pole bodies (sad1-tdTomato-natMX6) were introduced to formin chimera strains through mating. Table 4.4 lists the fission yeast strains used in this study.

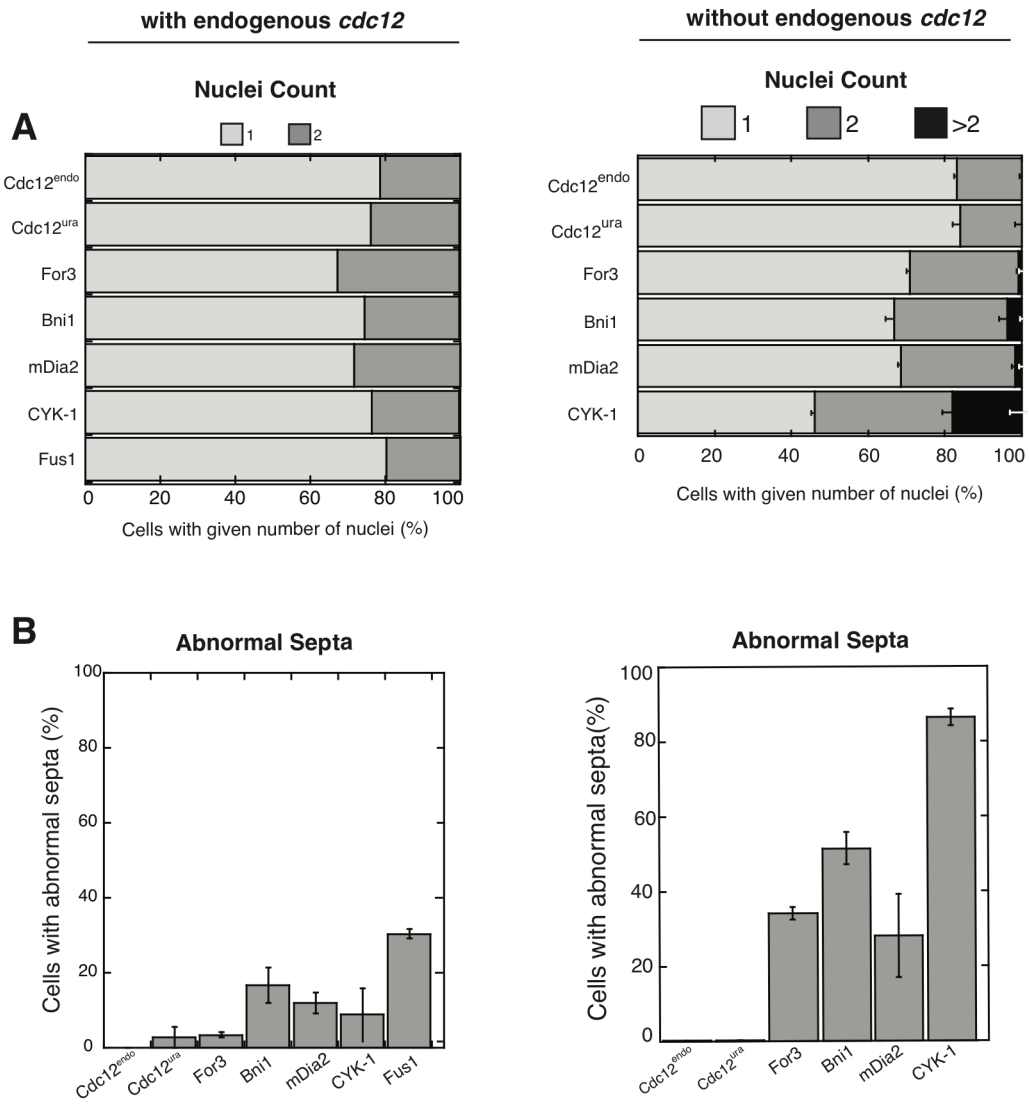

Figure 4.3. Formin chimera strains exhibit fewer cytokinesis defects in the presence of endogenous *cdc12*.

(A-B) Quantification of methanol fixed fission yeast cells stained with DAPI (nuclei) and Calcofluor (septa) for formin chimera strains with endogenous *cdc12* (left) and without endogenous *cdc12* (right). (A) Percent of cells with one, two, or more than two nuclei. (B) Percent of cells with septa exhibiting abnormal septa (misplaced, misoriented, or abnormally broad). Graphs of formin chimera strains without endogenous *cdc12* are also shown in Figure 4.9.

Table 4.4. Fission yeast strains used in Chapter 4

Strain name	Genotype	Reference
KV343	FY527 cdc12-mGFP::KanR	(Christensen et al., 2019)
KV387	h-, cdc12(Nterm)-cdc12(FH1FH2)-cdc12(Cterm)-GFP::ura4+,	This study
KV389	h-, cdc12(Nterm)-fus1(FH1FH2)-cdc12(Cterm)-GFP::ura4+, ura4-294	This study
KV391	h-, cdc12(Nterm)-cyk-1(FH1FH2)-cdc12(Cterm)-GFP::ura4+,	This study
KV395	h-, cdc12(Nterm)-for3(FH1FH2)-cdc12(Cterm)-GFP::ura4+, ura4-294	This study
KV399	h-, cdc12(Nterm)-bni1(FH1FH2)-cdc12(Cterm)-GFP::ura4+, ura4-294	This study
KV401	h-, cdc12(Nterm)-mdia2(FH1FH2)-cdc12(Cterm)-GFP::ura4+,	This study
KV405	h-, cdc12Δ::KanR, cdc12(Nterm)-cdc12(FH1FH2)-cdc12(Cterm)-GFP::ura4+ (chimera integrated at ura locus)	This study
KV407	h-, cdc12Δ::KanR, cdc12(Nterm)-for3(FH1FH2)-cdc12(Cterm)-GFP::ura4+ (chimera integrated at ura locus)	This study
KV408	h-, cdc12Δ::KanR, cdc12(Nterm)-bni1(FH1FH2)-cdc12(Cterm)-GFP::ura4+ (chimera integrated at ura locus)	This study
KV445	h-, cdc12Δ::KanR, cdc12(Nterm)-mdia2(FH1FH2)-cdc12(Cterm)-GFP::ura4+ (chimera integrated at ura locus)	This study
KV451	h-, cdc12Δ::KanR, cdc12(Nterm)-cyk-1(FH1FH2)-cdc12(Cterm)-GFP::ura4+ (chimera integrated at ura locus)	This study
KV489	h?, rlc1-tdTomato::natMX6; FY527 cdc12-mGFP::KanR	This study
KV552	h?, sad1-mCherry-NatMX6, cdc12Δ::KanR, cdc12(Nterm)-cyk-1(FH1FH2)-cdc12(Cterm)-GFP::ura4+ (chimera integrated at ura locus)	This study
KV778	h? rlc1-tdTomato-natMX6, cdc12Δ::KanR, cdc12(Nterm)-cdc12(FH1FH2)-cdc12(Cterm)-GFP::ura4+ (chimera integrated at ura locus)	This study
KV779	h? rlc1-tdTomato-natMX6, cdc12Δ::KanR, cdc12(Nterm)-bni1(FH1FH2)-cdc12(Cterm)-GFP::ura4+ (chimera integrated at ura locus)	This study

Table 4.4 continued.

KV790	h? rlc1-tdTomato-natMX6, cdc12Δ::KanR, cdc12(Nterm)-for3(FH1FH2)-cdc12(Cterm)-GFP::ura4+ (chimera integrated at ura locus)	This study
KV793	h? rlc1-tdTomato-natMX6, cdc12Δ::KanR, cdc12(Nterm)-mDia2(FH1FH2)-cdc12(Cterm)-GFP::ura4+ (chimera integrated at ura locus)	This study
KV794	h? rlc1-tdTomato-natMX6, cdc12Δ::KanR, cdc12(Nterm)-CYK1(FH1FH2)-cdc12(Cterm)-GFP::ura4+ (chimera integrated at ura locus)	This study
KV940	h? cdc12-mGFP::KanR, rlc1-tdTomato-natMX6, sad1-tdTomato-natMX6, ade6-M210 leu1-32 ura4-D18	This study
KV941	h?, cdc12Δ::KanR, cdc12(Nterm)-for3(FH1FH2)-cdc12(Cterm)-GFP::ura4+ (chimera integrated at ura locus), rlc1-tdTomato-natMX6, sad1-tdTomato-natMX6, ade6-M210, leu1-32, ura4-D18	This study
KV942	h?, cdc12Δ::KanR, cdc12(Nterm)-bni1(FH1FH2)-cdc12(Cterm)-GFP::ura4+ (chimera integrated at ura locus), sad1-tdTomato-natMX6 ade6-M210, leu1-32, ura4-D18	This study
KV943	h?, cdc12Δ::KanR, cdc12(Nterm)-bni1(FH1FH2)-cdc12(Cterm)-GFP::ura4+ (chimera integrated at ura locus), rlc1-tdTomato-natMX6, sad1-tdTomato-natMX6 ade6-M210, leu1-32, ura4-D18	This study
KV946	h? cdc12Δ::KanR, cdc12(Nterm)-cyk-1(FH1FH2)-cdc12(Cterm)-GFP::ura4+ (chimera integrated at ura locus), rlc1-tdTomato-natMX6, sad1-tdTomato ade6-M210, leu1-32, ura4-D18	This study
KV948	h? cdc12-mGFP::KanR, sad1-tdTomato-natMX6 ade6-M210	This study
KV949	h? cdc12Δ::KanR, cdc12(Nterm)-cdc12(FH1FH2)-cdc12(Cterm)-GFP::ura4+ (chimera integrated at ura locus), sad1-tdTomato-natMX6 ade6-M210, leu1-32, ura4-D18	This study
KV950	h? cdc12Δ::KanR, cdc12(Nterm)-for3(FH1FH2)-cdc12(Cterm)-GFP::ura4+ (chimera integrated at ura locus), sad1-tdTomato-natMX6 ade6-M210, leu1-32, ura4-D18	This study

Table 4.4 continued.

KV951	h- cdc12Δ::KanR, cdc12(Nterm)-mdia2(FH1FH2)-cdc12(Cterm)-GFP::ura4+ (chimera integrated at ura locus), sad1-tdTomato-natMX6 ade6-M210, leu1-32, ura4-D18	This study
KV962	h? cdc12Δ::KanR, cdc12(Nterm)-mdia2(FH1FH2)-cdc12(Cterm)-GFP::ura4+ (chimera integrated at ura locus), sad1-tdTomato-natMX6, rlc1-tdTomato-natMX6, ade6-M210, leu1-32, ura4-D18	This study

Cell imaging and growth. Differential interference contrast (DIC) and epifluorescence images were collected on an IX-81 microscope (Olympus, Tokyo, Japan) fitted with an Orca-ER camera (Hamamatsu, Bridgewater, NJ) and a 60X, 1.4 NA Plan Apo objective. Confocal images were acquired on a Zeiss Axiovert 200M microscope (Zeiss) equipped with a Yokogawa CSU-10 spinning-disk unit (McBain, Simi Valley, CA) fitted with a Cascade 512B EM-CCD camera (Photometrics, Tuscon, AZ) controlled by MetaMorph software (Molecular Devices, Sunnyvale, CA) and illuminated with 50 milliwatt 473- and 561-nm DPSS lasers.

For live cell DIC and epifluorescence imaging, cells were grown overnight in YE5S media at 25º C, subcultured into EMM5S minimal media without thiamine, and kept in log phase for 20-22 hr. They were then imaged directly on glass slides using Z-stacks of 10 slices with a 0.5 μm step size.

Cell growth assay. Each strain was grown for 24-36 hr in YE5S and then seeded in triplicate in a 96-well plate at initial OD_{600} readings of 0.03 and 0.06. OD_{600} readings were measured every 10 min for 24 hr in a Tecan Inifinite M200Pro (Tecan Systems, Inc., San Jose, CA) plate reader at 30º C with an orbital shaking amplitude of 4 mm.

BoDipy-phallicidin staining. Upon receipt, BoDipy-phallicidin stocks were prepared by resuspending 300 units BoDipy-phallicidin (Thermo Fisher Scientific, Waltham, MA) in 1.5 mL

methanol. This solution was divided into 25 µL aliquots, vacuum dried, and stored at -20º C. Immediately prior to use, one dry BoDipy-phallicidin aliquot was resuspended in 10 µL PEM buffer (0.1 M NA PIPES pH 6.8, 1 mM EGTA, 1 mM $MgCl_2$).

Cells were grown in YE5S for 36 hr. 1 mL cells for each strain growing at 25º C and OD_{600} ~0.4 were fixed with 333 µL 16% paraformaldehyde for 5 min. The fixed cells were washed 3 times at RT with PEM with 30 s spins at 7000 rpm in between. Cells were permeabilized in 1 mL PEM buffer with 1% Triton X-100 (Sigma-Aldrich, St. Louis, MO) at RT for 1 min. Cells were then washed three times as before and resuspended in 10 µL PEM and stained by adding 1 µL BoDipy-phallicidin solution for 30 min in the dark at room temperature. After staining, cells were washed once with PEM and spun for 30 s at 7000 rpm to obtain a pellet. The supernatant was removed, leaving a small amount of liquid. 4 µL of cells were imaged directly on glass slide as described above on an IX-81 microscope (Olympus).

DAPI/Calcofluor staining. Cells were grown in YE5S for 36 hr, and DIC images were acquired directly on glass before fixation. DAPI/Calcofluor staining was conducted as described previously (Christensen et al., 2017). Briefly, cells were grown in YE5S at 25º C for 36 hr and then fixed with 100% cold methanol. For staining, cells were incubated in 300 µL 50 mM sodium citrate with 4 µL Calcofluor White Stain (Fluka Analytical, Sigma-Aldrich, St. Louis, MO) for 5 min at 37º C. They were then washed with 1 mL 50 mM sodium citrate and resuspended in 15 µL sodium citrate and 4 µL DAPI stock (1 mg/mL in H_20, Life Technologies, Carlsbad, CA) and kept on ice until imaging. 2.5 µL of stained cells were placed on glass slide and imaged as described above on an IX-81 microscope (Olympus) with an Orca-ER camera (Hamamatsu) and 60X, 1.4 NA Plan-Apo objective.

Quantification of DIC and DAPI/Calcofluor images. DAPI/Calcofluor stained cells were scored for number of nuclei and appearance of septa, where abnormal septa were those that

were misplaced or misshapen. DIC images were used for quantification of cell length, cytokinesis defects, and morphology defects. Cell length was measured along the long axis of each cell. For cytokinesis defects, strains containing spindle pole body marker Sad1-tdTomato were quantified for number of spindle pole bodies. For morphology defects, DIC images of each strain were quantified for three cell width measurements: 2 µm from each cell tip (m1 and m3) and in the cell midzone (m2). The standard deviation of these cell width measurements was then calculated for each cell.

Quantification of formin chimera expression. Z-stacks of strains expressing formin chimeras tagged with GFP and Rlc1-tdTomato were imaged on glass slides as described above and sum slice projections were compiled. To measure formin chimera expression, ROIs were created of both contractile rings and the corresponding whole cell. The mean fluorescence of the formin-GFP was measured in the contractile ring and divided by the mean formin-GFP of the whole cell to control for background fluorescence. The average of this ratio was calculated for two replicates for each strain and normalized to the control.

Plasmid construction. A Cdc12 fragment containing the FH1FH2 domains and a portion of the C-terminal tail [Cdc12(882-1687)] was cloned by traditional restriction enzyme cloning into pET21a-MBP-TEV at BamHI/XhoI. The Bni1-Cdc12 [Bni1(1228-1766)-Cdc12(1391-1687)] and mDia2-Cdc12 [mDia2(527-1022)-Cdc12(1391-1687)] chimeras were amplified from plasmids constructed for building the formin chimera strains, and were inserted via Infusion cloning (Clontech, Mountain View, CA) into pET21a-MBP-TEV at BamHI/NotI to form MBP-chimera-HIS(x6).

Protein purification. The Cdc12 fragment [Cdc12(882-1687)] and the Bni1-Cdc12 and mDia2-Cdc12 chimeras were expressed in *E. coli* strain BL21-Codon Plus (DE3)-RP (Agilent Technologies, Santa Clara, CA) with 0.5 mM isopropyl ß-D-1-thiogalactopyranoside for 16 h at

16º C. Cells were lysed by sonication in extraction buffer (50 mM NaH_2PO (anhydrous), 500 mM NaCl, 10% glycerol, 10 mM imidazole, 10 mM BME pH 8) with EDTA-free Protease Inhibitor Cocktail (Roche, Basel, Switzerland) and were clarified. The extract was incubated for 1 h at 4º C with Talon Resin (Clontech), loaded onto a column, washed with extraction buffer, and protein was eluted with 250 mM imidazole. The formin chimeras were dialyzed into buffer [50 mM HEPES (pH 7.0), 50 mM NaCl, 5% glycerol, 0.01% NaN_3, 1 mM DTT] for cation exchange chromatography (GE Healthcare, Little Chalfont, UK). The cleanest fractions were pooled and dialyzed into SNAP buffer [20 mM HEPES (pH 7.4), 200 mM KCl, 0.01% NaN_3, 10% glycerol, and 1 mM DTT]. The mDia2-Cdc12 chimera required additional size exclusion chromatography and was filtered on a Superdex 200 10/300 GL column (GE Healthcare). Aliquots of all formin proteins were flash frozen in liquid nitrogen and stored at -80º C. Chicken skeletal muscle actin was purified as described in (Spudich and Watt, 1971). Fission yeast profilin Cdc3 was overexpressed and purified from *E. coli* using poly-L-proline affinity chromatography as described in (Lu and Pollard, 2001)

TIRF microscopy and analysis. TIRFM was conducted with the formin chimeras as described previously (Christensen et al., 2019). Briefly, time lapse TIRFM movies were obtained with through-the-objective TIRF illumination on an Olympus IX-71 microscope with an iXon EMCCD camera (Andor Technology) and a cellTIRF 4-line system (Olympus). 1 nM of either Cdc12, Bni1-Cdc12, or mDia2-Cdc12 formin chimeras was added to a polymerization mix (see Christensen et al., 2019) along with 2.5 uM fission yeast profilin Cdc3, which was then added to Mg-ATP-actin (10% Alexa-488 labeled) to induce actin assembly. This mixture was added to a flow chamber and imaged at 5 s intervals at room temperature.

The nucleation activity was determined by counting the total number of actin filaments for each TIRFM movie at frame 48, the same amount of time since the initiation of each actin assembly

reaction. Each construct (actin only, Cdc12, Bni1-Cdc12, or mDia2-Cdc12) was counted in triplicate. To determine the actin filament elongation rate, 10 individual actin filaments from each TIRFM movie were tracked over time, with their lengths measured every fifth frame for 7-9 total measurements. An average elongation rate was calculated for each filament, and then those were averaged to obtain an average for each movie. Each construct (actin only, Cdc12, or mDia2-Cdc12) was measured in triplicate with the exception of Bni1-Cdc12, which was only measured in duplicate due to a low number of Bni1-Cdc12-associated filaments in the third TIRFM movie due to Bni1-Cdc12's low nucleation activity.

4.3 Results

An SCPR model reveals the importance of nucleation efficiency on cytokinetic ring formation. We hypothesize that in addition to regulation of its activity in time and space, a formin's ability to facilitate a particular cellular function also depends on its specific actin assembly properties (Vidali et al., 2009). To begin to address this question, we investigated how the actin assembly properties of the fission yeast cytokinesis formin Cdc12 affect contractile ring assembly by extending a 3D SCPR model (Bidone et al., 2014). Cdc12 nucleates F-actin very efficiently, generating 1 actin filament per 2.5 Cdc12 dimers, and elongates F-actin at a rate of 10-12 subunits/s/μM (Table 4.1). Thus, we systematically varied both the number of node-bound filaments, N, representing formin nucleation efficiency, and the formin-mediated processive actin filament elongation rate, vpol (Fig. 4.1). We varied N from 30 (~one filament every two nodes) to 130 (two filaments per node), and vpol from 0.04 to 0.24 μm/s, capturing a relevant range for a wide array of formins (Kovar et al., 2006, 2006; Moseley and Goode, 2005; Neidt et al., 2008; Romero et al., 2004; Scott et al., 2011). Additionally, we performed simulations where formin-mediated actin filament elongation was inhibited by forces exceeding 1 pN at the barbed end,

mimicking the mechanoregulation of Cdc12 (Zimmermann et al., 2017). We analyzed simulations using a continuous collective variable that tracks ring progress throughout the simulation by accounting for gradual changes in actin and node morphologies that are organized in more or less ring-like structures. 100% ring progress corresponds to a fully formed ring.

Our simulations reproduced cytokinesis ring assembly at nucleation efficiencies and unloaded elongation rates close to those measured for Cdc12 (N=130 and vpol=0.18 μm/s, respectively, with mechanoinhibition) (Fig. 4.4A). Keeping N constant at Cdc12's nucleation efficiency of 130 filaments and varying the elongation rate, the model predicts that at low elongation rates (vpol = 0.04-0.10 μm/s), nodes form clumps with short actin filaments elongating radially from the nodes (Fig. 4.4A, top row, left). However, at high actin elongation rates (vpol > 0.20 μm/s), nodes condense into a small number of clumps that elongate actin filament bundles along the domain's long axis (Fig. 4.4A, top row). Neither high nor low actin filament elongation rates facilitate reliable ring formation, however, a wide range of intermediate values supported ring assembly (Fig. 4.4B). This held true for both mechanoinhibited and uninhibited formins, but shifted optimal ring-forming conditions toward lower values of vpol¬ for uninhibited formins (Fig. 4.4A, top row, right, and Fig. 4.4B-C). Mechanoinhibition also led to ring formation over a larger region of parameter-space (Fig. 4.5), consistent with the idea that Cdc12's activity is uniquely tailored for its role in cytokinesis.

Keeping the elongation rate constant at 0.18 μm/s, which maximizes ring assembly at Cdc12's high nucleation efficiency (Fig. 4.4B), and varying N, our simulations show that at low nucleation efficiency (N < 90), isolated clumps of nodes formed, but never assembled a ring (Fig. 4.4A, bottom row). Only high nucleation efficiencies (N ≥ ~110 filaments) reliably support complete ring formation (Fig. 4.4C). Uninhibited formins follow the same trend at lower values of vpol (Fig. 4.4B-C). Unlike high elongation rates, low N conditions were not noticeably different

between mechanoinhibited and uninhibited formins (Fig. 4.4C). Ring progress for the entire parameter-space explored (i.e., varying vpol and N simultaneously) are reported as heat maps in Fig. 4.5A and B.

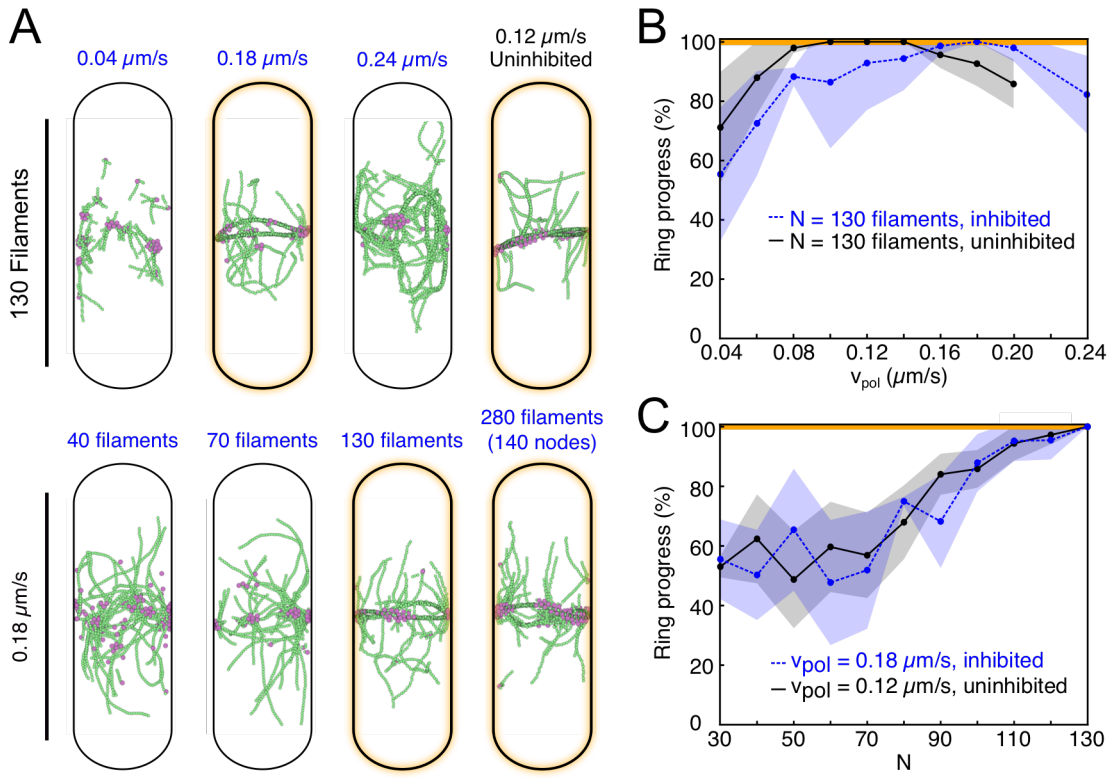

Figure 4.4. Ring assembly depends more strongly on formin nucleation efficiency than polymerization rate.
(A) Snapshots at t = 800 seconds of simulations at different values of v_{pol} and N. *Upper*: Snapshots at a constant nucleation efficiency, N = 130, depict non-ring morphologies resulting from too low or too high of polymerization rates, as well as proper ring formation for intermediate values (orange highlight). In the absence of formin mechanoinhibition, low polymerization rates (right) resemble higher elongation rates with inhibition. *Lower*: Snapshots at a constant polymerization rate, v_{pol} = 0.18 μm/s, depict a progression to more favorable conditions for ring assembly with increasing N. Outcomes of simulations using 65 nodes are comparable to those of equivalent simulations using 140 nodes (right, v_{pol} = 0.2 μm/s). (B-C) Dependence of ring progress (see Methods) on key parameters, where 100% corresponds to a fully formed ring (orange line). Data points are averages of 3-7 independent runs and shaded regions represent standard deviations. 2D heat maps are shown in Fig. 5 (B) At a constant nucleation efficiency, N = 130, progress toward ring assembly exhibits a gradual dependence on polymerization rate, v_{pol}, with many conditions supporting complete ring assembly. Peak values are shifted to higher v_{pol} with formin mechanoinhibition. (C) At a constant polymerization rate that favors ring assembly, ring progress increases drastically at high nucleation efficiency for both inhibited and uninhibited formins.

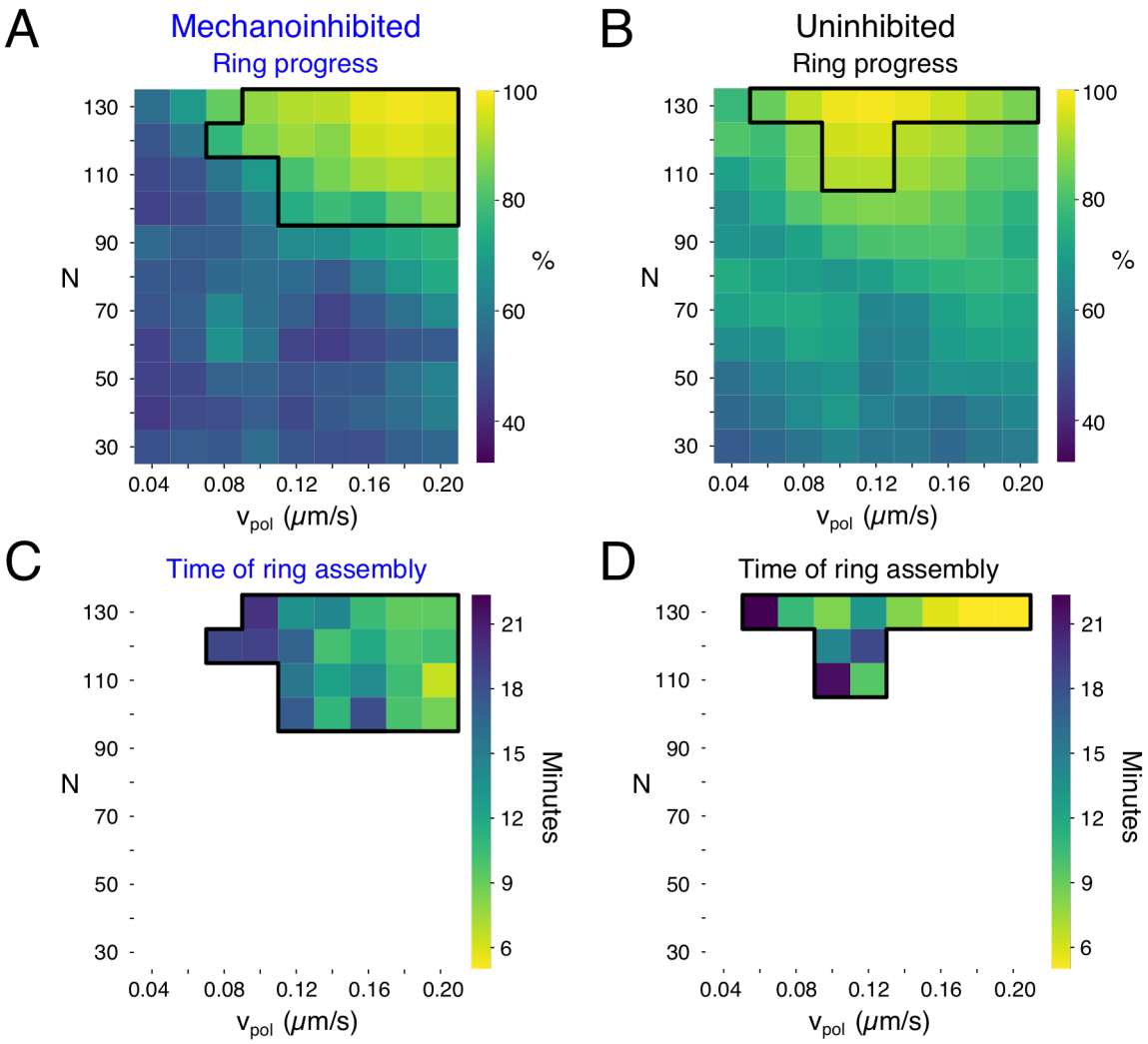

Figure 4.5. Heat maps of ring progress and time to ring assembly as a function of *N* and v_{pol}.

(A and B) The maximum progress toward ring formation (see Methods) is shown varying N and v_{pol} in the presence (A) or absence (B) of formin mechanoinhibition. The region in which at least one fully formed ring emerged is outlined in black, which is noticeably larger when mechanoinhibition is present. Data are averages of 3-7 independent runs and are smoothed with a Gaussian filter ($\sigma = 0.67$). Three simulations were run at $v_{pol} = 0.24$ μm/s for $N = 130$ with mechanoinhibition, and the results are shown in Fig. 4.4. (C and D) The average time of ring assembly is shown varying N and v_{pol} in the presence (C) or absence (D) of formin mechanoinhibition. Although average values are plotted, data come only from simulation runs where rings formed (i.e., at least one replicate reached 100% ring progress), meaning some values represent single runs.

Together, these quantifications indicate that while both are important, the nucleation efficiency of formin is a more powerful determinant of ring formation than the formin-mediated actin filament elongation rate.

Fission yeast formin Cdc12 chimeras localize to the contractile ring and produce viable cells that complete cell division. To test the results of our computational modeling in vivo, we aimed to alter the actin assembly properties of the contractile ring formin Cdc12 in fission yeast cells. Point mutations in formin's actin assembly FH2 domain typically lead to a nonfunctional protein due to the general importance of the FH2 domain in formin dimerization and barbed end-binding. Therefore, we instead engineered formin chimera strains in which the FH1FH2 actin assembly domains of full length Cdc12 were replaced with the FH1FH2 domains from functionally and evolutionarily diverse formins with significantly different actin assembly properties: Fus1 (fission yeast), For3 (fission yeast), Bni1 (budding yeast), mDia2 (mouse), and CYK-1 (worm) (Fig. 4.6A).

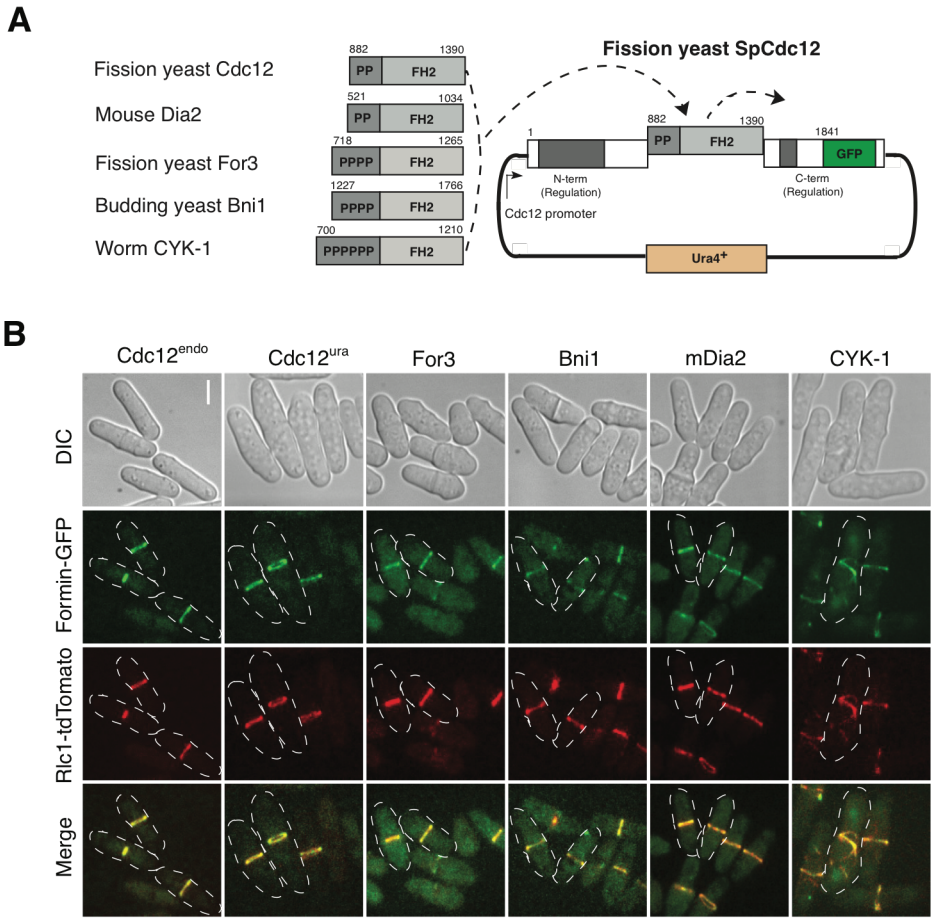

Figure 4.6. Fission yeast formin Cdc12 chimeras localize to the contractile ring and produce viable cells that divide.

(A) Schematic of fission yeast formin Cdc12 chimeras, in which the FH1FH2 actin assembly domains were replaced by FH1FH2 domains from formins with diverse actin assembly properties. Each "P" indicates a single FH1 polyproline motif. Image not drawn to scale. (B) Representative micrographs of formin chimera strains showing morphology (DIC), the formin chimera (Formin-GFP), the contractile ring (Rlc1-tdTomato), and the merge. Scale bar, 5 µm.

Given that we specifically replaced only the FH1FH2 domains, we expected the regulation and localization of the formin chimeras to be maintained, as Cdc12's N- and C-terminal regions are thought to be primarily responsible for targeting it to the contractile ring (Yonetani et al., 2008). However, the formin chimeras should exhibit a wide range of actin assembly properties (nucleation efficiency, barbed end elongation rate, barbed end dissociation rate). Table 4.1 details a comparison of in vitro actin assembly properties for all the aforementioned formins relative to Cdc12. As described in the modeling section above, Cdc12 is an efficient nucleator (1 filament per 2.5 dimers), but a comparatively slow elongator (10-12 subunits/s/uM) (Kovar et al., 2006, 2003; Scott et al., 2011). If, as suggested by our computational modeling, formin's actin filament nucleation rate is particularly critical for its role in cytokinesis, we predicted that the mDia2 chimera will compromise cytokinesis the least, as its nucleation rates is most similar to Cdc12 (Table 4.1). However, if formin's elongation rate is most important in vivo, then For3 and mDia2 chimeras will function best in fission yeast cytokinesis (Table 4.1).

One copy of each formin chimera was integrated into the ura4 locus under control of the endogenous cdc12 promoter and tagged at the C-terminus with GFP (Fig. 4.6A). Endogenous cdc12 was deleted by replacement with a kanR cassette (Bähler et al., 1998), and the contractile ring was observed by tagging the endogenous copy of the myosin II regulatory light chain Rlc1 with tdTomato. For controls, endogenous cdc12 was tagged C-terminally with GFP (Cdc12endo) and full length Cdc12-GFP was integrated into the ura4 locus with endogenous cdc12 deleted (Cdc12ura). With the exception of fission yeast Fus1, which was not studied further (see Supplemental Discussion), all of the formin chimera strains produced viable cells (Fig. 4.6B), despite the diverse in vitro actin assembly parameters of the various formin FH1FH2 domains (Table 4.1). Like control Cdc12 strains, the formin chimeras co-localize with Rlc1-tdTomato in the contractile ring or contractile ring-like material at the cell midzone (Fig. 4.6B), suggesting that

they are properly recruited to the cell division site. Furthermore, the formin chimera strains follow the same general growth curve over time as the control strains (Fig. 4.7A), and staining of fixed cells with BoDipy-phallicidin did not reveal significant differences in their general actin cytoskeletal architectures (Fig. 4.7B). We also validated that purified formin chimera constructs mDia2-Cdc12 and Bni1-Cdc12, which contain either the mDia2 or Bni1 FH1FH2 domains and a 296 amino acid Cdc12 tail, exhibit similar in vitro actin assembly properties (nucleation activity and barbed end elongation rate) as previously characterized for the isolated mDia2 and Bni1 FH1FH2 domains (Fig. 4.8 and Table 4.1).

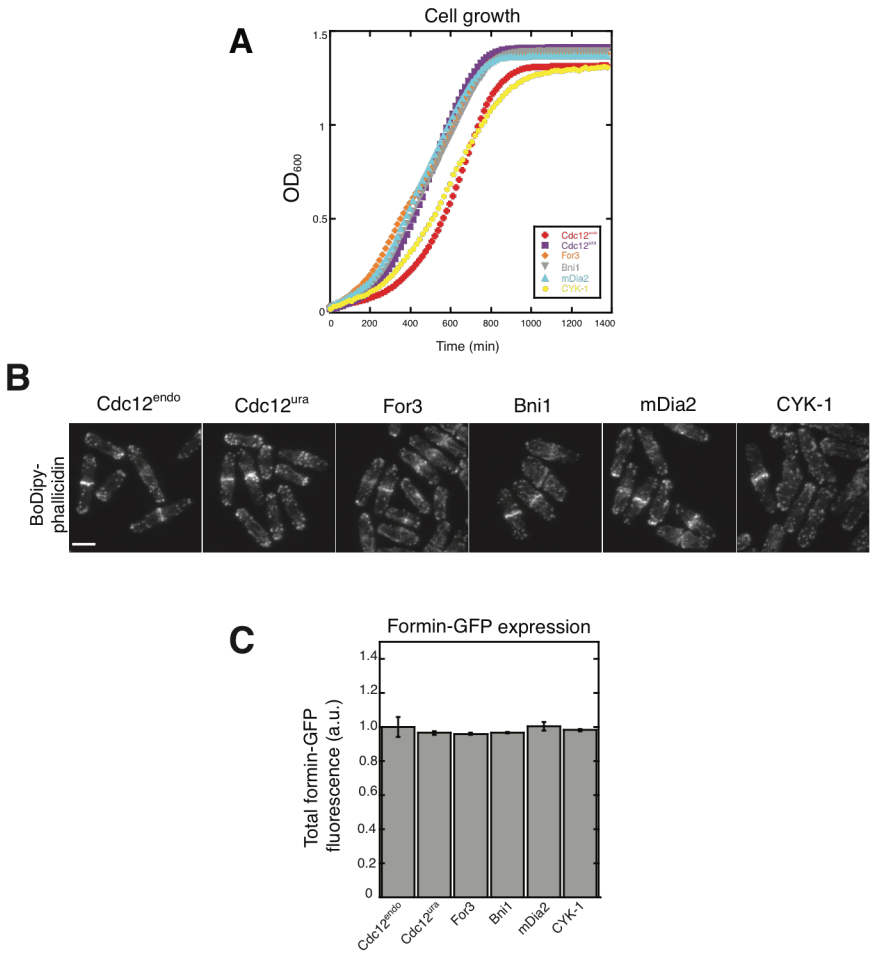

Figure 4.7. Growth rates and actin organization of formin chimeras are similar to WT. (A) Growth curve of formin chimera strains. (B) Micrographs of fixed formin chimera cells stained with BoDipy-phallicidin to label actin filaments. Scale bar, 5 µm. (C) Plot of formin-GFP expression levels normalized to Cdc12^{endo}. Error bars represent the standard error of two independent experiments.

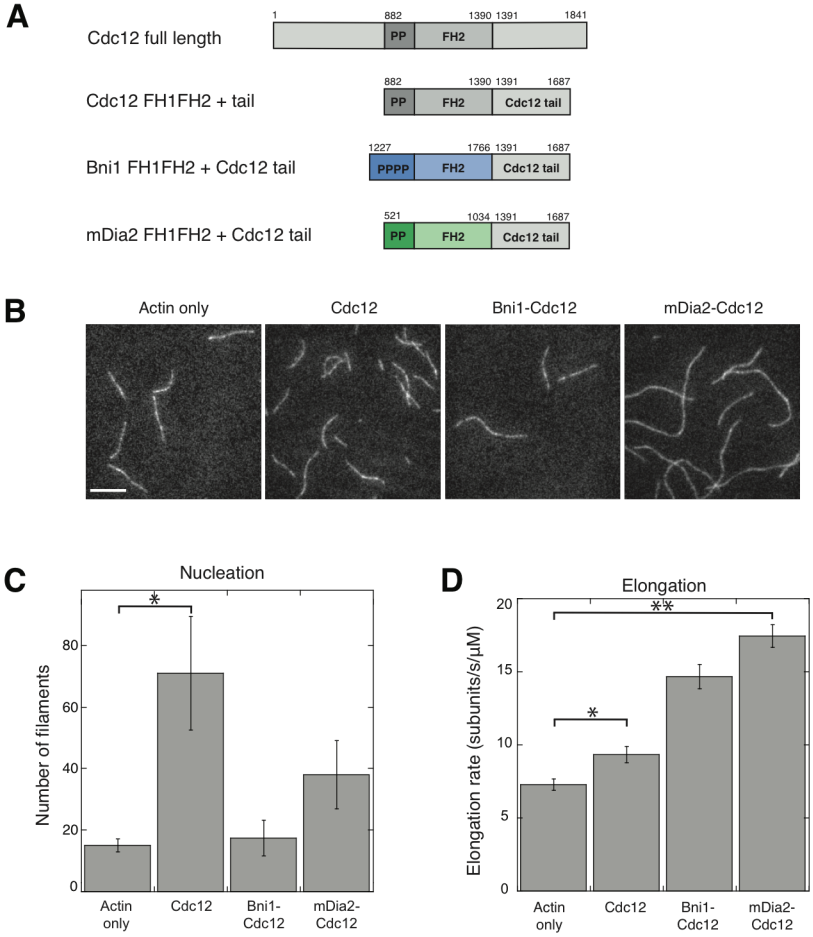

Figure 4.8. The biochemical properties of formin chimeras with a Cdc12 tail are similar to previously measured biochemical properties of isolated FH1FH2 domains.
(A) Schematic of full length Cdc12 compared to formin chimera constructs tested for biochemical activity. (B) Single color TIRFM of 1.5 μM Mg-ATP actin (10% Alexa-488 labeled) with 2.5 μM fission yeast profilin Cdc3, and either no formin (actin only) or 1 nM Cdc12, Bni1-Cdc12, or mDia2-Cdc12 formin chimeras. Scale bar, 8 μm. (C) Quantification of the number of filaments nucleated by formin chimera constructs. Two tailed t-tests for data sets with unequal variance yielded p-value *p=0.047. Error bars indicate standard error of three independent biological replicates of 10 actin filaments for actin only, Cdc12, and mDia2-Cdc12, and two independent biological replicates of 10 actin filaments for Bni1-Cdc12 due to a lack of Bni1-Cdc12-associated filaments in the third replicate. (D) Quantification of formin chimera elongation rates. Two tailed t-tests for data sets with unequal variance yielded p-values *p=0.038, **p=0.0013. Error bars indicate standard error of three independent biological replicates of 10 actin filaments for actin only, Cdc12, and mDia2-Cdc12, and two independent biological replicates of 10 actin filaments for Bni1-Cdc12 due to a lack of Bni1-Cdc12-associated filaments in the third replicate.

Formin Cdc12 chimera fission yeast strains display a range of cytokinesis and morphology defects. Although diverse formin chimeras localize to the contractile ring and generally support life in fission yeast, preliminary imaging suggested that some formin chimera strains may exhibit cytokinesis defects (for example, see CYK-1 in Fig. 4.6B). Importantly, quantification of the total amount of formin-GFP fluorescence revealed that the expression levels of the formin chimeras are not statistically different from Cdc12endo (Fig. 4.7C). Therefore, any observed cytokinesis defects are not likely due to differences in formin chimera expression.

To characterize general cytokinesis defects in the formin chimera strains, we stained methanol-fixed cells with DAPI and Calcofluor to quantify the number of nuclei and abnormal septa, respectively (Fig. 4.9). First, while only 15-20% of control Cdc12endo and Cdc12ura cells have two nuclei, 28% of For3, 30% of Bni1, 30% of mDia2, and 36% of CYK-1 cells have two or more nuclei (Fig. 4.9A-B), suggesting cytokinesis defects. Second, whereas no Cdc12endo or Cdc12ura cells have abnormally placed and/or shaped septa, 34% of For3, 52% of Bni1, 28% of mDia2, and 86% of CYK-1 cells contain abnormal septa (Fig. 4.9A,C). Formin chimera strains also exhibit varying degrees of morphological defects (Fig. 4.10). For example, CYK-1 chimera cells are abnormally long, growing to an average length of almost twice that of Cdc12endo cells (Fig. 4.10A), presumably because of their failure to divide properly. By imaging the spindle pole body (SPB) marker Sad1-tdTomato, we also determined that formin chimera strains have at least twice as many cells in mitosis compared to control strains (Fig. 4.10B). Finally, the formin chimera strains also exhibited abnormal bulging morphology defects (Fig. 4.10C). Collectively, these data indicate that formin chimeras have a range of general division and morphology defects, with CYK-1 exhibiting extreme abnormalities and mDia2 appearing the most similar to control strains.

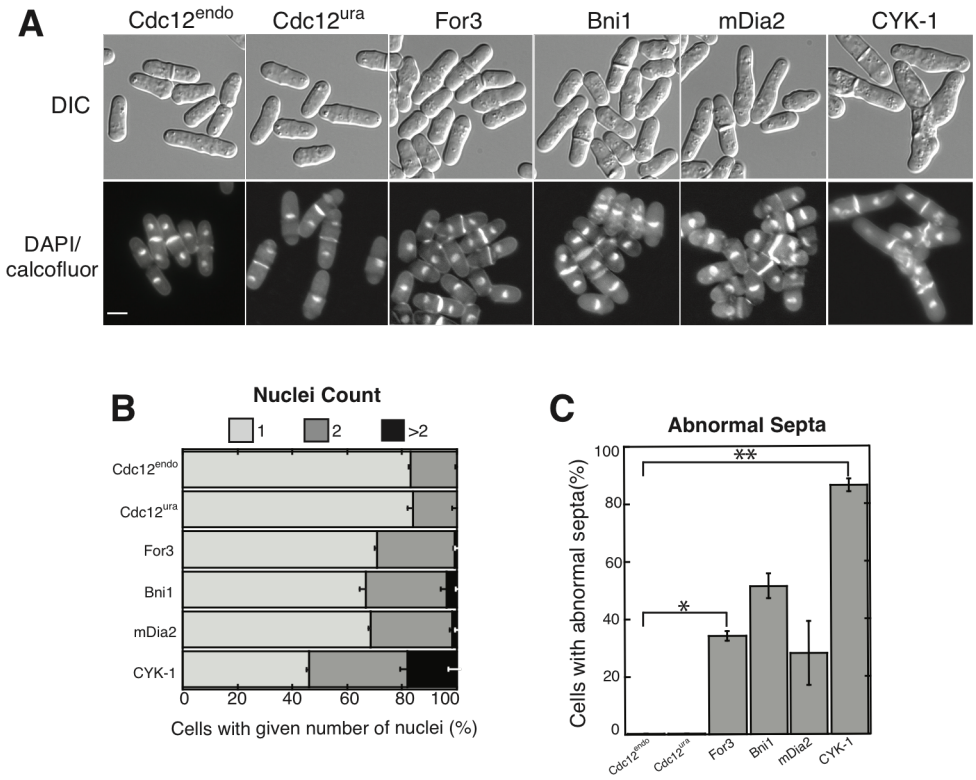

Figure 4.9. Formin chimera strains exhibit a range of cytokinesis defects.
(A) Representative micrographs of the indicated formin chimera strains; DIC (morphology) and methanol fixed cells stained with DAPI (nuclei) and Calcofluor (septa). Scale bar, 5 μm. (B-C) Quantification of general cytokinesis defects. (B) Percent of cells with one, two or >two nuclei. (C) Percent of cells with septa exhibiting abnormal septa (misplaced, misoriented, or abnormally broad). Two-tailed t-tests for data sets with unequal variance yielded p-values *p=0.030, **p=0.017. Error bars in (B-C) indicate standard error of two biological replicates of at least 400 cells each.

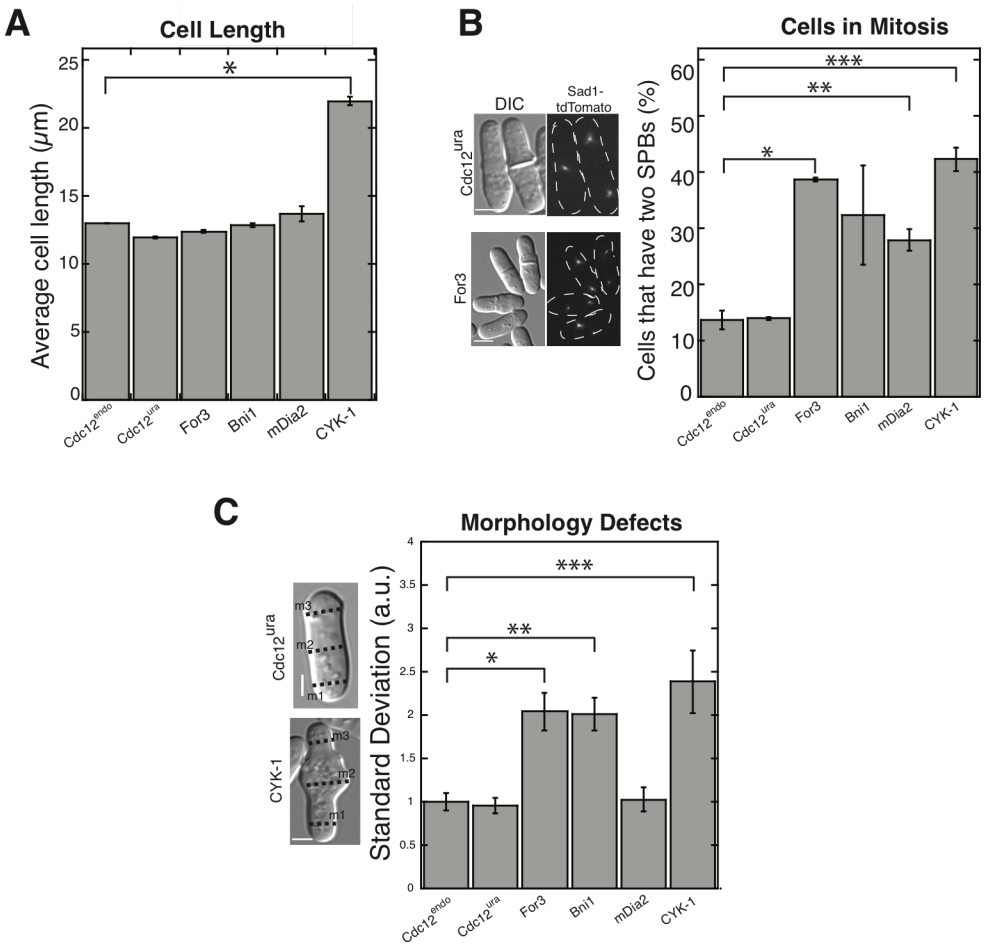

Figure 4.10. Formin chimera strains exhibit a range of morphology defects.
(A) Plot of average cell lengths. Two-tailed t-tests for data sets with unequal variance yielded p-value *p=0.023. Error bars indicate standard error of two biological replicates with at least 30 cells each. (B) Plot of the percentage of cells in mitosis, as indicated by the number of spindle pole bodies. Two-tailed t-tests for data sets with unequal variance yielded p-values *p=0.045, **p=0.030, ***p=0.0079. Error bars indicate standard error of two biological replicates of at least 15 cells each. (C) Plot of morphology defects, determined by calculating the standard deviation of three cell width measurements. Scale bar, 3 μm. Two-tailed t-tests for data sets with unequal variance yielded p-values *p=9.678×10^{-5}, **p=3.72×10^{-5}, ***p=0.0011. Error bars indicate standard error of at least 25 cells.

One possibility is that the formin chimeras are dominant negatives, whose expression causes cytokinesis and morphology defects irrespective of their ability to functionally replace endogenous Cdc12 for division. Therefore, we also analyzed whether cells simultaneously expressing both the formin chimeras (integrated at the ura locus) and endogenous cdc12 have division defects (Fig. 4.3). Formin chimera strains exhibit dramatically less severe general cytokinesis defects (abnormal septa and multi-nucleated cells) in the presence of endogenous Cdc12 (Fig. 4.3). Therefore, the observed abnormalities in cells exclusively expressing formin chimeras result primarily from deficiencies in their ability to replace endogenous Cdc12 for cytokinesis rather than because of secondary dominant negative effects.

Formin chimera fission yeast cells progress through cytokinesis at different rates.

The computational model specifically revealed that inefficient actin filament nucleation by formin causes defects in the rate of contractile ring assembly (Figs. 4.4, 4.5). Because the formin chimera cells exhibit varying degrees of general division defects (Fig. 4.9, Fig. 4.10), we used quantitative imaging to determine which cytokinesis steps are specifically compromised in each strain. Fission yeast cells primarily assemble contractile rings from precursor cytokinesis nodes through a well-defined temporal pathway of events (Fig. 4.11A): (1) formation of a broad band of precursor nodes, (2) contractile ring assembly, (3) initiation of constriction, (4) completion of constriction, and (5) cell separation (Vavylonis et al., 2008; Wu et al., 2003). We imaged dividing cells expressing the contractile ring marker myosin II regulatory light chain Rlc1-tdTomato and the SPB marker Sad1-tdTomato by time-lapse fluorescence microscopy of a single plane to comparatively quantify the kinetics of cytokinesis for the formin chimera strains (Fig. 4.11B-C).

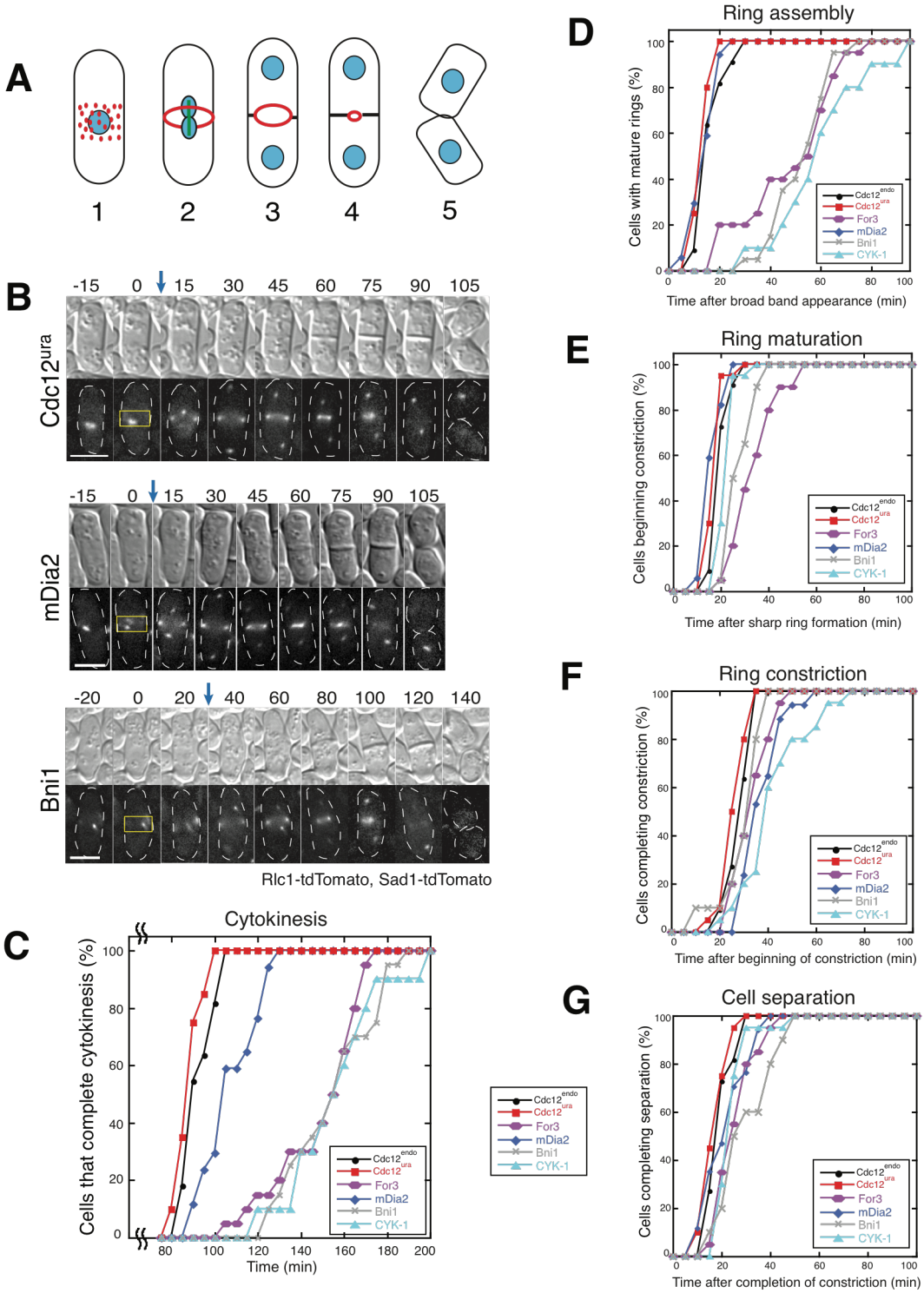

Figure 4.11. Formin chimeras with poor nucleation efficiency exhibit delays in ring assembly.

Figure 4.11 continued: (A) Schematic of fission yeast cytokinesis: (1) node assembly, (2) ring assembly, (3) Ring maturation, (4) Ring constriction, and (5) Cell separation. (B) Representative time-lapse micrographs of the morphology (DIC) and contractile ring (Rlc1-tdTomato) of representative formin chimera cells. Time is indicated in minutes. Spindle pole bodies are labeled with Sad1-tdTomato. Blue arrows indicate time of spindle pole body separation. Yellow boxes indicate broad band of precursor cytokinesis nodes. Scale bar, 5 μm. (C) Time required for at least 20 cells to complete the entire time course of cytokinesis for each strain. (D-G) Time required for at least 20 cells to complete the indicated step of cytokinesis for each strain. (D) Frequency of cells that assemble a sharp ring over time. (E) Frequency of cells that complete ring maturation. (F) Frequency of cells that complete ring constriction. (G) Frequency of cells that complete cell separation.

We compared the entire cytokinesis time course by analyzing cells that completed cytokinesis from precursor node appearance to cell separation within the three-hour imaging window (Fig. 4.11B-C). In control cells, SPBs separate around 10 minutes after Rlc1-labeled precursor nodes initially appear. However, the timing of SPB separation and the initiation of ring assembly is uncoupled in some formin chimera strains, where Rlc1 fluorescence appears at the midzone up to an hour before SPB separation (Fig. 4.11B, see Bni1 panel). Therefore, the initial appearance of the broad band of cytokinetic precursor nodes marks time zero in our experiments. 100% of Cdc12endo and Cdc12ura control cells complete cytokinesis with remarkably little variability in ~90 minutes after the appearance of precursor nodes. Conversely, the formin chimera strains have distinct kinetic profiles of the progression of cytokinesis events, some with significant delays (Fig. 4.11C). The mDia2 strain progresses through cytokinesis with only a slight delay as compared to control cells, with 100% of cells completing cell division within 120 minutes of precursor node appearance. However, For3, Bni1, and CYK-1 strains display substantial delays, as 100% of cells have not finished cell division until after ~160 minutes following precursor node appearance.

We next quantified the elapsed time for each well-defined cytokinetic event in order to determine which specific step(s) causes delays in formin chimera strain cytokinesis: ring assembly

(Fig. 4.11D), ring maturation (Fig. 4.11E), ring constriction (Fig. 4.11F), or cell separation (Fig. 4.11G). For ring assembly, we measured the time for each cell to assemble a fully formed contractile ring after the initial appearance of precursor node fluorescence at the midzone (Fig. 4.11D). Interestingly, two populations of ring assembly profiles emerged from this analysis. Similar to control strains, 100% of mDia2 cells assemble contractile rings within 25 minutes of broad brand appearance. Conversely, For3, Bni1, and CYK-1 exhibit a large lag in ring assembly, with 100% of cells finally forming contractile rings between 70-100 minutes after node appearance (Fig. 4.11D). After the contractile ring was assembled, we quantified the ring maturation time, or the time elapsed prior to the onset of cell constriction (Fig. 4.11E). The time course of ring maturation was similar for all formin chimeras, with most cells finishing ring maturation within 20 minutes of ring formation. Only For3 and Bni1 cells exhibit a brief lag, but are still much more similar to control strains than they are during ring assembly. Similarly, we found that the elapsed time for ring constriction (Fig. 4.11F) and cell separation (Fig. 4.11G) is similar for all of the formin chimera and control strains.

Our in vivo evidence reveals that different rates of contractile ring assembly are primarily responsible for major differences between the formin chimera strains in the overall time course of cytokinesis. This is consistent with formin-mediated actin assembly having a major role in generation of the contractile ring (Chang et al., 1997; Pollard and Wu, 2010), and because mDia2 has the most similar nucleation properties to Cdc12 (Table 4.1 and Fig. 4.8), supports the conclusion from our quantitative modeling that efficient formin-mediated nucleation of actin filaments is particularly critical for contractile ring assembly in fission yeast (Fig. 4.1).

4.4 Discussion

Formins associate processively with the growing barbed end of actin filaments to rapidly assemble long, unbranched actin filaments that facilitate diverse cellular processes, such as cytokinesis and polarization. While most formins assemble actin filaments by the same general nucleation and processive elongation mechanism, particular formins exhibit a wide range of specific rate constants. We previously determined that the quantitative actin assembly properties of the three fission yeast formin isoforms vary widely, indicating that in addition to activation at the right time and place, a formin's specific properties might be tailored for a particular cellular role (Scott et al., 2011; Vidali et al., 2009). Here, we investigated the effects of formin Cdc12's actin assembly properties on cytokinetic ring assembly by extending a computational model that was previously developed and validated for reproducing fission yeast ring formation in 3D based on the SCPR mechanism (Bidone et al., 2014; Laporte et al., 2011; Vavylonis et al., 2008). The model allowed us to independently control formin nucleation efficiency and elongation rate and to characterize their relative effects on ring assembly (Fig. 4.1). We also implemented a force-sensitive mechanism for actin filament elongation mimicking the mechanoregulation of formin Cdc12. Our simulations demonstrated that variations in formin nucleation efficiency sharply impact the probability of ring formation (Fig. 4.4A and C), which is consistent with our experimental characterization of formin chimera fission yeast cells. In contrast, changes in elongation rate had important effects at extreme values, but were less impactful overall (Fig. 4.4A and B).

To begin to test the roles of formin nucleation efficiency and elongation rate in vivo, we engineered formin chimera fission yeast strains in which the FH1FH2 actin assembly domains of Cdc12 were replaced with the FH1FH2 domains from a group of evolutionary and functionally distinct formins: Fus1 (fission yeast), For3 (fission yeast), Bni1 (budding yeast), mDia2 (mouse),

and CYK-1 (worm) (Fig. 4.6A). These formin chimeras retain Cdc12's localization and regulation, but demonstrate a wide range of actin assembly properties (Table 4.1).

We found that with the exception of fission yeast Fus1 (see further discussion in Supplemental Discussion), cells expressing formin chimeras instead of endogenous cdc12 are viable. More importantly, despite the proper localization of diverse formin chimeras to the division site, they exhibit a range of cytokinesis and morphological defects whose severity appears to be anticorrelated to the similarity of their nucleation efficiency to that of Cdc12. Specifically, the mDia2 formin chimera is generally less defective in cytokinesis than For3, Bni1, and CYK-1 formin chimeras (Figs. 4.9, 4.11). Interestingly, an analysis of their in vitro actin assembly properties reveals that For3, Bni1, and CYK-1 elongate actin as fast or faster than Cdc12 (Table 4.1). In fact, both For3 and mDia2 elongate actin at the same rate as Cdc12 (Table 4.1). Thus, a formin's elongation rate does not correlate well with its ability to successfully facilitate cytokinesis in fission yeast, at least over a ~4- to 8-fold range. However, For3, Bni1, and CYK-1 have drastically lower nucleation efficiencies than Cdc12, at 1.5%, 10%, and 3% as efficient, respectively. Conversely, mDia2 nucleates actin filaments 25% as efficiently as Cdc12 and completes cytokinesis at similar rates as control strains (Fig. 4.11). Together, these data indicate that fission yeast cytokinesis is extremely robust, but formins with low nucleation efficiency are unable to facilitate the assembly of a mature contractile ring as effectively as Cdc12. While our results indicate that contractile ring assembly in fission yeast relies on Cdc12's particular actin assembly properties, whether the actin assembly properties of other formins are tailored for their cellular process remains to be determined (Vidali et al., 2009).

Fission yeast cells use the SCPR mechanism for contractile ring assembly, which relies upon ~140 pre-ring cytokinesis nodes that contain formin Cdc12 and myosin, as well as other regulatory and scaffolding proteins (Vavylonis et al., 2008; Wu et al., 2006). Results from

simulations of 140 nodes confirm the data from simulations at 65 nodes (Fig. 4.2B). Node-bound Cdc12 is thought to nucleate and then elongate actin filaments that are captured and pulled by myosin on nearby nodes, bringing nodes closer together to assemble a continuous F-actin ring. These F-actin connections between nodes are severed by cofilin, and process starts again until the ring is fully formed (Vavylonis et al., 2008; Wu et al., 2006). It follows, then, that Cdc12's efficient nucleation of F-actin (one filament for every 2.5 Cdc12 dimers; Table 4.1) is paramount in its role as the sole cytokinesis formin in fission yeast because the initial step of contractile ring assembly requires efficient formation of actin filaments. Conversely, we suspect that a formin's processive run length (the number of actin monomers added) and dissociation rate contribute less to contractile ring assembly than its other actin assembly properties. Specifically, the F-actin severing protein cofilin is thought to abolish node-node contacts prior to dissociation of formin from the barbed end (Chen and Pollard, 2013). This is consistent with our experimental data, as mDia2 dissociates from elongating actin filament barbed ends an order of magnitude faster than Cdc12 (Table 4.1), but still effectively completes cytokinesis in fission yeast.

It has been shown that each pre-ring cytokinesis node contains only four Cdc12 dimers, which explains why the formin chimeras that are poor nucleators exhibit a long lag in ring assembly (Laplante et al., 2016). For3, Bni1, and CYK-1 produce 10% or fewer actin filaments per formin dimer as Cdc12 (Table 4.1), apparently resulting in impaired node coalescence and slower contractile ring formation (Figs. 4.4, 4.5). It is also possible that because For3, Bni1, and CYK-1 are poor nucleators, some of these formin chimera cells use a distinct 'spot' pathway for contractile ring assembly (Fig. 4.12) (Chang, 1999).

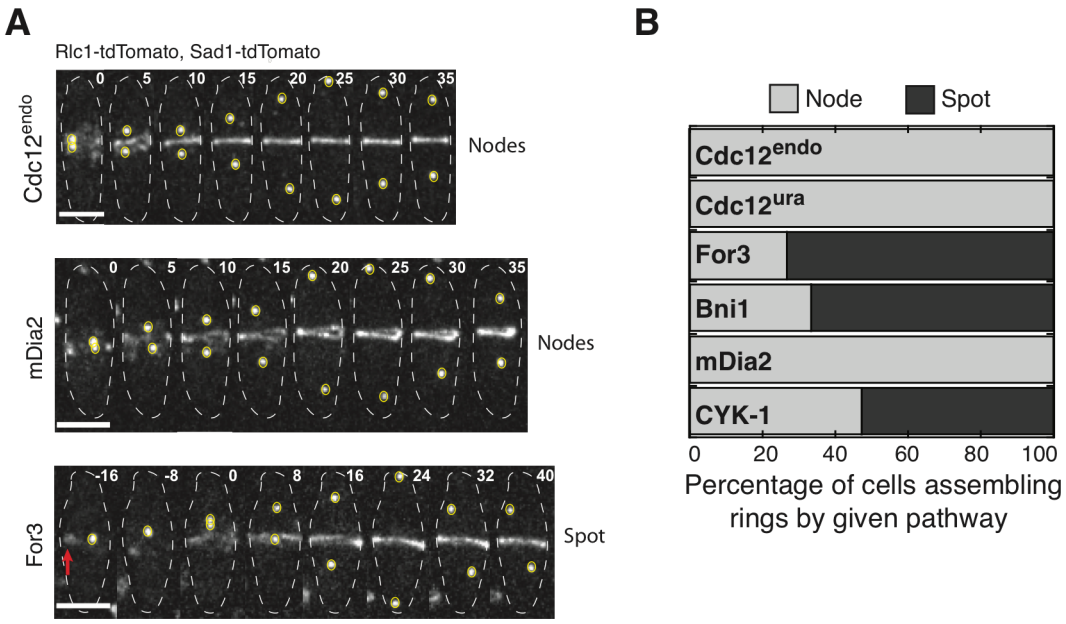

Figure 4.12. Formin chimera strains assemble contractile rings through different pathways.
(A) Representative confocal time-lapse images of the indicated strains showing assembly of the contractile ring (Rlc1-tdTomato). Red arrow indicates Rlc1-tdTomato spot (bottom panel). Spindle pole bodies are labeled with Sad1-tdTomato. Time 0: spindle pole body (yellow circles) separation. Time is indicated in minutes. Scale bar, 5 µm. (B) Percentage of cells that build contractile rings through the precursor cytokinesis node or spot pathways.

While a formin's elongation rate is also presumably tailored for its cellular role, formin elongation rates can be modulated by external mechanical forces. Cdc12 is a mechanosensor whose elongation is inhibited by myosin-mediated pulling of Cdc12-bound filaments (Zimmermann et al., 2017). Conversely, application of force to budding yeast Bni1 increases its F-actin elongation rate in the presence of profilin (Courtemanche et al., 2013). Actin filaments, especially in contractile networks, often experience mechanical forces that could modify elongation by mechanosensitive formins to facilitate assembly of particular F-actin networks.

Thus, formin chimera elongation rates might affect fission yeast cytokinesis less than their nucleation efficiencies.

Although our quantitative modeling and the associated in vivo experiments strongly support the importance of Cdc12's tailored actin filament nucleation efficiency to facilitate contractile ring assembly in fission yeast, we cannot rule out that cytokinesis defects in the formin chimera strains are due to other differences between the formins such as (1) FH1 and/or FH2 domain association with accessory proteins, (2) recruitment of distinct actin-binding proteins to formin-mediated actin filaments, (3) posttranslational modifications of FH1 and/or FH2 domains and associated activities, or (4) interaction with microtubules (for further discussion of each of these possibilities, see Supplemental Discussion). Finally, we cannot rule out the possibility that formin FH1FH2 domains have evolved to function optimally in the presence of the formin's native regulatory domains, such that swapping FH1FH2 domains would not automatically confer the same in vitro actin assembly properties. Despite these potential caveats, our experimental and computational observations are consistent and provide evidence that Cdc12's actin assembly properties are optimized for cytokinetic ring assembly, with its ability to efficiently nucleate actin filaments from cytokinesis nodes being a predominant factor.

4.5 Supplemental Discussion

The fission yeast mating formin Fus1 is the only formin chimera that produced unviable cells, the basis for which is presently unclear. Since Fus1 nucleates and elongates F-actin at similar rates as Cdc12 (Table 3), it is possible that there is an underlying technical issue. However, it is also possible that cells exclusively expressing Fus1 chimeras fail to grow because Fus1's FH1FH2 domains are specifically regulated to elongate F-actin only during mating. Unlike Cdc12, Fus1's FH1FH2 domain also bundles actin filaments (Scott et al., 2011). Thus, Fus1 chimeras could

bundle actin filaments at the midzone, leading to excessive bundling that result in failure of cell division, as it has been shown that fission yeast cytokinesis requires a dynamic bundler to accommodate filament sliding during contractile ring constriction (Li et al., 2016). However, the FH2 domain of mDia2 has also been shown to bundle F-actin (Harris et al., 2006), a characteristic that does not appear to lessen the mDia2 chimera strain's viability. We also observed that the Fus1 formin chimera produced the worst cytokinesis defects of any formin chimera even in the presence of endogenous *cdc12* (Figure 4.3), which suggests that it behaves as a dominant negative and could explain why the Fus1 strain is unviable once *cdc12* is deleted. Future work is required to understand why Fus1's FH1FH2 domains cannot replace Cdc12's during fission yeast cytokinesis.

Together, our quantitative modeling and in vivo experiments strongly support the importance of Cdc12's tailored actin filament nucleation efficiency to facilitate contractile ring assembly in fission yeast. However, we cannot rule out that differences in the severity of cytokinesis defects in the formin chimera strains are impacted by other differences between the formins such as (1) association with accessory proteins or recruitment of distinct actin-binding proteins, (2) posttranslational modifications and associated activities, and/or (3) interaction with microtubules.

First, some formins associate with cofactors that enhance their actin nucleation activity. For example, budding yeast nucleation promoting factor Bud6 interacts with formin Bni1 to enhance nucleation by recruiting actin monomers (Graziano et al., 2011). Any such interactions that increase the nucleation efficiency of formin chimeras that are poor nucleators would be absent in fission yeast, which could contribute to the long contractile ring assembly delays seen in For3, Bni1 and CYK-1 chimera strains. For example, cells expressing For3 formin chimeras also have severe cytokinesis defects even though For3 is a fission yeast formin that could potentially still interact with important accessory proteins. However, fission yeast Bud6 has been proposed to

serve as a tether that mediates cortical localization and potentially activation of For3 (Martin et al., 2007), so spatially restricting the For3 chimera to the cell midzone could abolish its ability to interact with Bud6.

Similarly, different FH1FH2 domains could assemble F-actin that associates with distinct actin-binding proteins. For3 and Cdc12 have been shown to interact with different tropomyosin variants in fission yeast cells (Johnson et al., 2014). Alternatively, it is possible that For3's poor nucleation efficiency is tailored for its role of assembling actin cables for polarized growth in fission yeast (Feierbach and Chang, 2001; Nakano et al., 2002). Is also possible that For3 bypasses inefficient nucleation by associating with and elongating existing filaments, such as those nucleated by Arp2/3 complex in endocytic actin patches (Kovar et al., 2011). Second, although Cdc12's FH1FH2 domains are not thought to bundle F-actin (Scott et al., 2011), Cdc12 contains a C-terminal multimerization domain that promotes Cdc12 clusters that can bundle actin filaments during early cytokinesis (Bohnert et al., 2013). However, Cdc12 is phosphorylated downstream of its FH2 domain during cytokinesis, which abrogates the interactions that cause multimerization and bundling (Bohnert et al., 2013). Because Cdc12's C-terminal regulatory region is present in all formin chimeras, it is unlikely that this specific phosphorylation alters the activity of our formin chimeras. However, it is possible that introducing different FH1FH2 domains presents new targets for post-translational modifications that could compromise the activity of the cytokinesis formin.

Third, many formins, including mDia2, have been shown to interact with microtubules, suggesting that they could function in cellular processes involving both the actin and microtubule cytoskeletons. mDia2's F-actin polymerization is inhibited by its association with microtubules (Gaillard et al., 2011). Potential interactions with microtubules could influence how efficiently different formin chimeras generate cytokinetic contractile rings in fission yeast cells.

4.6 Supplemental Methods

Computational model of 3D SCPR-based cytokinetic ring assembly. In this study, we extend the 3D SPCR model (Bidone et al., 2014) in order to investigate how the nucleation and elongation efficiencies of different formins affect cytokinetic ring assembly. We incorporate variability in the number of formins per node, to simulate different nucleation efficiencies and systematically vary the corresponding polymerization rates. An analysis of the impact of a different number of formin dimers per node was also provided in the first 2D SCPR model of cytokinetic ring formation in fission yeast (Vavylonis et al., 2008), but here we restructured the code to simulate cases where nodes have different number of formins in the same simulation run. This allows us to explore conditions of mixed number of formin per nodes, where nodes presented in the same simulation either no formin or 1 per node (to mimic conditions of very low nucleation efficiency), or either 1 or 2 formin per nodes (to mimic conditions of nucleation efficiency lower than Cdc12).

Actin filaments representation and interactions. Actin filaments are represented as semiflexible polymers elongating from membrane nodes, with persistence length l_p =10μm. Initially, filaments are 0.2 μm long and comprise one formin bead connected to the corresponding node, and two consecutive filament beads: the first one connected to the formin bead at equilibrium separation l_0 = 0.1 μm, and the second one connected to the first filament bead at the same equilibrium separation. When the filament elongates, it adds beads from the second one, at the defined polymerization rate. All filaments present as a chain of consecutive filament beads, interconnected to one another by harmonic potential energies, with uniform spring constant k = 100 pN/μm and equilibrium separation l_0, as in (Laporte et al., 2012) and (Bidone et al., 2014). Also as in (Laporte et al., 2012) and (Bidone et al., 2014), actin filament beads are subjected to thermal forces, to simulate random collisions with the cytoplasm, and implicit crosslinking, to

simulate the presence of crosslinking proteins in fission yeast (Laporte et al., 2012). In detail, crosslinking between filament beads occur when the two beads of filaments from different nodes become closer than r_{crslnk} = 0.1 μm, and establish a harmonic interaction potential, with spring constant k_{crslnk} = 100 pN/μm and equilibrium distance r_0 = 0.03 μm. Actin filaments polymerize from formin dimers at a rate v_{pol} that varies between 0.04-0.25 μm/s, depending on the specific conditions of formin polymerization rate tested in each simulation. Actin filaments also turnover and are removed from the simulation at every time step with a probability dt/τ, with the average lifetime τ = 16 s, of the same order of that detected experimentally and previously used in (Vavylonis et al., 2008; Laporte et al., 2012; Bidone et al., 2014). This value is in the range that allows ring assembly, as it was previously shown that either $\tau < 15$ s or $\tau > 30$ s promote clump formation (Vavylonis et al., 2008). Upon filament removal, a new filament is allowed to grow from the formin nucleator in a random direction and at the defined polymerization rate.

Basic algorithm. The computational model implements overdamped Langevin equation in order to update position of each filament bead, formin dimer and node bead, over time. We use Euler implementation scheme, in order to determine, at each time step dt, the new bead position r_i as a function of the previous position $r_{i,0}$, using the total force on the particle $F_{i,TOT}$ normalized by the particle friction ζ_i:

$$r_i = r_{i,0} + \frac{F_{i,TOT}}{\zeta_i}\, dt$$

The total force on each filament bead is obtained from a sum of deterministic and stochastic contributions, such that:

$$F_{i,TOT} = F_{i,spring} + F_{i,bend} + F_{i,myo} + F_{i,crslnk} + F_{i,stoch}$$

Where $F_{i,spring}$ is the force from the harmonic interaction potential between consecutive beads and $F_{i,bend}$ is the bending force, which depends upon l_p; $F_{i,myo}$ is the force from myosin pulling;

$F_{i,crslnk}$ is the harmonic interactions between an actin bead and another filaments' bead because of crosslinking (see Table 4.2 for parameter value); $F_{i,stoch}$ is a stochastic force representing thermal fluctuations and satisfying the fluctuation-dissipation theorem:

$$\langle F_{i,stoch} F_{i,stoch} \rangle_{\alpha,\beta} = 2\left(\frac{k_\beta \mathrm{T}\xi}{dt}\right)\hat{I}_{\alpha,\beta}$$

Where $\hat{I}_{\alpha,\beta}$ is the second-order unit tensor.

Computational domain. The computational domain is a yeast-shaped cylinder with with radius R = 1.74 μm and length l =13 μm. All particles in the domain, myosin nodes, actin filament beads and formin dimers, are subjected to a boundary, confinement force $F_{confinement}$ = 5 pN, directed inward. This force is of the order of magnitude needed to confine one actin filament bead brought outside by Brownian motion and is equally applied to formin and node beads when crossing the boundary.

Myosin motors representation, initialization and interactions. Myosin motors, which capture and directionally pull actin filaments from other nodes, are distributed on the simulation domain cylindrical boundary, mimicking the fission yeast cell membrane. They are initially distributed randomly circumferentially and according to a Gaussian distribution, in a band of 2σ = 1.8 μm centered in the middle of the domain, which represents the cell equator. Over the course of the simulations, motors undergo stochastic intermittent movements as a result of pairwise attractions between them, which emerge from capturing and pulling actin filaments from other nodes. They remain confined at the cylindrical boundary and move in 2D, as an inward force is incorporated $F_{confinement}$ = 5 pN. In order to reproduce experimentally detected 2D diffusion rates, node friction is ζ_{node} = 400 pN s/μm as in (Vavylonis et al., 2008; Laporte et al., 2012; Bidone et al., 2014; Zimmerman et al., 2017). Motors are also stably bound to explicit formin nucleators,

represented as beads, harmonically bound to the motors using equilibrium separation r_{formin} = 0.05 μm and spring constant k_{formin}=100 pN/μm. Formins elongate actin filaments at specific rates, mimicking different elongation efficiencies and motors capture and pull actin filaments nucleated from other nodes, within a distance r_{capt} = 0.1 μm and force F_{myo} = 4 pN. To limit the magnitude of pulling force when nodes connect with bundles of actin filaments, the pulling force was reduce as $F_{myo} = \mu F_{0,myo}/N_c$, where μ = 0.3 and N_c is equal to the number of filament beads cross-linked to the captured bead, when $N_c > 3$. This reduction in force represents the distribution of myosin force over many filaments in the bundle and the interference of myosin activity with actin cross-linkers, as in (Bidone 2013 and Laporte 2012). When motors become close to one another ($r_{node} < 0.1$ μm), they are subjected to a short range repulsive radial potential, corresponding to a repulsive force F_{rep}=50 pN.

Model of formin nucleators and initialization. The presence of formin dimers on a node is simulated using spherical particles directly connected to the node through fixed elastic interactions with stiffness k_{formin}=100 pN/μm and equilibrium separation r_{formin} = 0.05 μm. Formins elongate actin filaments in random directions inside the domain because, while their equilibrium distance from the bound node is fixed, they can freely rotate around the node, under the effect of thermal, randomized forces. Formins are subjected to the same cytoplasmic friction of the actin filament beads, ζ_b = 0.108 pN s/μm. Each formin polymerizes an actin filament by extending the equilibrium length of the spring connecting the formin to the first filament bead (the barbed end) at v_{pol}, up to twice its equilibrium value, then incorporating a new actin bead in the center. In the case of mechanoinhibition, v_{pol} is reduced to 30% when formin is subjected to forces >1pN (Zimmermann et al., 2017). Different types of formins are simulated using a different number of spherical formin particles per node. This parameter is adjusted by controlling the total number of

filaments, N, and using either none, 1, or 2 formins per node, depending on the difference between N and the number of nodes, n. During initialization, one formin is assigned to each node in a random order. If the number of filaments, N, is equal to the number of nodes, n, each node presents one bound formin particle. If $N < n$, then the system presents a mixture of nodes with bound either none or 1 formin particle. If $N < n$ and $N < 2n$ then some nodes present 2 formin particles while others present 1. If $N = 2n$, all nodes are bound to 2 formin particles. Formin particles experience boundary effects, similar to nodes and actin filament beads, using an inward force $F_{confinement} = 5$ pN.

Comparison with previous SCPR models. The main difference of this model with respect to previous SCPR models (Vavylonis et al., 2008; Laporte et al., 2012; Bidone et al., 2014; Zimmerman et al., 2017) is that it allows simulations with different number of formins per node within the same run (section above). With respect to the 3D SCPR model (Bidone et al., 2014), it also incorporates force-dependent formin inhibition of polymerization rate, similar to (Vavylonis et al., 2008) and (Zimmermann et al., 2017). A detailed comparison of the main parameter values for each code is reported in Table 3.

Variations in number of filaments. The node condensation kinetics as a function of filaments number was also evaluated in (Vavylonis et al., 2008). By decreasing the total number of filaments in the system by half, thus assuming that each node is connected to one filament only instead of two, the time of ring assembly almost doubled. When the fraction of nodes containing filaments was systematically reduced, a linear increase of the time needed for ring assembly was observed, which corresponded to an increase in broad band width, with an insignificant effect on the largest node gap and node porosity.

Variations in polymerization rate. Ring assembly as a function of actin filament elongation rate was also evaluated in (Vavylonis et al., 2008). It was shown that, in order to obtain

reliable ring assembly, a polymerization rate >= 0.1 μm/s was needed. In fact, the time needed for ring formation, as well as the width of the node band at about half time of assembly did not vary significantly with v_{pol}>=0.1 μm/s. Our 3D SCPR model, by comparing both inhibited and noninhibited conditions, also shows a large range of v_{pol} acceptable for ring assembly greater than 0.1 μm/s.

Variations in number of nodes. We ran simulations at 140 nodes to mimic conditions observed in (Laplante et al., 2016). It was previously reported that the time needed to condense more than 50% of the nodes is equivalent between simulations with 65 nodes and simulations with > 65 nodes (Vavylonis et al., 2008). In this previous study, the node condensation kinetics were shown to be very similar for cases above ~50 nodes. Comparisons between our 65 and 140 node simulations are shown in Figs. 4.2 and 4.4, which agree with the conclusions of (Vavylonis et al., 2008) – both numbers of nodes lead to comparable ring assembly kinetics.

Ring Progress Collective Variable. We report an estimate of how closely the geometry of particles in the simulations resemble a ring. Our motivation was to improve on previous binary outcomes where rings either formed or not, and instead to develop a reproducible method to evaluate the many possible non-ring morphologies on the basis of being closer or farther from a ring.

This continuous collective variable is a linear combination of two normalized values that track (a) how spread out the nodes are along the cell-body long axis (y-axis), and (b) how connected the actin beads are near the central nodes. Our measurement for the broad band is calculated as the distance between the nodes at the 5 and 95 percentiles ranked by position along the cell-body long axis to ignore the effect of a small number of outlying nodes that are not necessary to form a ring. Typical values start around 2.8 microns and may reach ~0.5 microns in

well-formed rings. To assess the connectivity of actin beads, we consider actin beads within a range of 0.75 microns from the median y-position of the nodes and 0.25 microns from the cell surface. The angle coordinate about the y-axis is divided into 6° bins and the difference between median y-positions of the actin beads in adjacent bins is calculated. The maximum difference is used as a measure of discontinuity.

To get an equally-weighted linear combination, we normalize each value using a threshold characteristic of initial ring formation – 1.4 μm for node coalescence, and 0.13 μm for actin discontinuity. We clip values below the threshold, then subtract the threshold, resulting in favorable values that are 0 and unfavorable values are positive. This value is then subtracted from 1 and negative values are clipped to 0. Therefore, both variables will be 0 when far from ring assembly and both will reach 1 when a ring is formed. The ring progress collective variable is an average of these two normalized values and converted to a percentage. The ring progress value reported for simulations throughout the manuscript is the maximum value of this collective variable reached across all frames.

4.7 References

Alberts JB. 2009. Biophysically realistic filament bending dynamics in agent-based biological simulation. *PLoS ONE* **4**:e4748. doi:10.1371/journal.pone.0004748

Bähler J, Wu JQ, Longtine MS, Shah NG, McKenzie A, Steever AB, Wach A, Philippsen P, Pringle JR. 1998. Heterologous modules for efficient and versatile PCR-based gene targeting in Schizosaccharomyces pombe. *Yeast* **14**:943–951. doi:10.1002/(SICI)1097-0061(199807)14:10<943::AID-YEA292>3.0.CO;2-Y

Bidone TC, Tang H, Vavylonis D. 2014. Dynamic network morphology and tension buildup in a 3D model of cytokinetic ring assembly. *Biophys J* **107**:2618–2628. doi:10.1016/j.bpj.2014.10.034

Breitsprecher D, Goode BL. 2013. Formins at a glance. *Journal of Cell Science* **126**:1–7. doi:10.1242/jcs.107250

Chang F. 1999. Movement of a cytokinesis factor cdc12p to the site of cell division. *Current Biology* **9**:849-S2. doi:10.1016/S0960-9822(99)80372-8

Chang F, Drubin D, Nurse P. 1997. cdc12p, a protein required for cytokinesis in fission yeast, is a component of the cell division ring and interacts with profilin. *J Cell Biol* **137**:169–182.

Chen Q, Pollard TD. 2013. Actin Filament Severing by Cofilin Dismantles Actin Patches and Produces Mother Filaments for New Patches. *Current Biology* **23**:1154–1162. doi:10.1016/j.cub.2013.05.005

Christensen JR, Hocky GM, Homa KE, Morganthaler AN, Hitchcock-DeGregori SE, Voth GA, Kovar DR. 2017. Competition between Tropomyosin, Fimbrin, and ADF/Cofilin drives their sorting to distinct actin filament networks. *Elife* **6**. doi:10.7554/eLife.23152

Christensen JR, Homa KE, Morganthaler AN, Brown RR, Suarez C, Harker AJ, O'Connell ME, Kovar DR. 2019. Cooperation between tropomyosin and α-actinin inhibits fimbrin association with actin filament networks in fission yeast. *eLife* **8**:e47279. doi:10.7554/eLife.47279

Courtemanche N. 2018. Mechanisms of formin-mediated actin assembly and dynamics. *Biophysical Reviews*. doi:10.1007/s12551-018-0468-6

Courtemanche N, Lee JY, Pollard TD, Greene EC. 2013. Tension modulates actin filament polymerization mediated by formin and profilin. *Proceedings of the National Academy of Sciences* **110**:9752–9757. doi:10.1073/pnas.1308257110

Feierbach B, Chang F. 2001. Roles of the fission yeast formin for3p in cell polarity, actin cable formation and symmetric cell division. *Curr Biol* **11**:1656–1665.

Goode BL, Eck MJ. 2007. Mechanism and Function of Formins in the Control of Actin Assembly. *Annual Review of Biochemistry* **76**:593–627. doi:10.1146/annurev.biochem.75.103004.142647

Higgs HN, Peterson KJ. 2005. Phylogenetic Analysis of the Formin Homology 2 Domain. *Molecular Biology of the Cell* **16**:1–13. doi:10.1091/mbc.e04-07-0565

Isambert H, Venier P, Maggs AC, Fattoum A, Kassab R, Pantaloni D, Carlier MF. 1995. Flexibility of actin filaments derived from thermal fluctuations. Effect of bound nucleotide, phalloidin, and muscle regulatory proteins. *J Biol Chem* **270**:11437–11444.

Keeney JB, Boeke JD. 1994. Efficient targeted integration at leu1-32 and ura4-294 in Schizosaccharomyces pombe. *Genetics* **136**:849–856.

Kovar DR, Harris ES, Mahaffy R, Higgs HN, Pollard TD. 2006. Control of the assembly of ATP- and ADP-actin by formins and profilin. *Cell* **124**:423–435. doi:10.1016/j.cell.2005.11.038

Kovar DR, Kuhn JR, Tichy AL, Pollard TD. 2003. The fission yeast cytokinesis formin Cdc12p is a barbed end actin filament capping protein gated by profilin. *J Cell Biol* **161**:875–887. doi:10.1083/jcb.200211078

Kovar DR, Pollard TD. 2004. Insertional assembly of actin filament barbed ends in association with formins produces piconewton forces. *Proc Natl Acad Sci USA* **101**:14725–14730. doi:10.1073/pnas.0405902101

Kovar DR, Sirotkin V, Lord M. 2011. Three's company: the fission yeast actin cytoskeleton. *Trends in Cell Biology* **21**:177–187. doi:10.1016/j.tcb.2010.11.001

Laplante C, Huang F, Tebbs IR, Bewersdorf J, Pollard TD. 2016. Molecular organization of cytokinesis nodes and contractile rings by super-resolution fluorescence microscopy of live fission yeast. *PNAS* **113**:E5876–E5885. doi:10.1073/pnas.1608252113

Laporte D, Coffman VC, Lee I-J, Wu J-Q. 2011. Assembly and architecture of precursor nodes during fission yeast cytokinesis. *J Cell Biol* **192**:1005–1021. doi:10.1083/jcb.201008171

Laporte D, Ojkic N, Vavylonis D, Wu J-Q. 2012. α-Actinin and fimbrin cooperate with myosin II to organize actomyosin bundles during contractile-ring assembly. *Mol Biol Cell* **23**:3094–3110. doi:10.1091/mbc.E12-02-0123

Lee I-J, Coffman VC, Wu J-Q. 2012. Contractile-ring assembly in fission yeast cytokinesis: Recent advances and new perspectives. *Cytoskeleton (Hoboken)* **69**:751–763. doi:10.1002/cm.21052

Li F, Higgs HN. 2005. Dissecting Requirements for Auto-inhibition of Actin Nucleation by the Formin, mDia1. *Journal of Biological Chemistry* **280**:6986–6992. doi:10.1074/jbc.M411605200

Lu J, Pollard TD. 2001. Profilin Binding to Poly-l-Proline and Actin Monomers along with Ability to Catalyze Actin Nucleotide Exchange Is Required for Viability of Fission Yeast. *Mol Biol Cell* **12**:1161–1175.

Moseley JB, Goode BL. 2005. Differential activities and regulation of Saccharomyces cerevisiae formin proteins Bni1 and Bnr1 by Bud6. *J Biol Chem* **280**:28023–28033. doi:10.1074/jbc.M503094200

Nakano K, Imai J, Arai R, Toh-E A, Matsui Y, Mabuchi I. 2002. The small GTPase Rho3 and the diaphanous/formin For3 function in polarized cell growth in fission yeast. *J Cell Sci* **115**:4629–4639.

Nedelec F, Foethke D. 2007. Collective Langevin dynamics of flexible cytoskeletal fibers. *New Journal of Physics* **9**:427–427. doi:10.1088/1367-2630/9/11/427

Neidt EM, Skau CT, Kovar DR. 2008. The Cytokinesis Formins from the Nematode Worm and Fission Yeast Differentially Mediate Actin Filament Assembly. *Journal of Biological Chemistry* **283**:23872–23883. doi:10.1074/jbc.M803734200

Otomo T, Otomo C, Tomchick DR, Machius M, Rosen MK. 2005. Structural Basis of Rho GTPase-Mediated Activation of the Formin mDia1. *Molecular Cell* **18**:273–281. doi:10.1016/j.molcel.2005.04.002

Pasquali M, Shankar V, Morse DC. 2001. Viscoelasticity of dilute solutions of semiflexible polymers. *Phys Rev E Stat Nonlin Soft Matter Phys* **64**:020802. doi:10.1103/PhysRevE.64.020802

Paul AS, Pollard TD. 2009. Review of the mechanism of processive actin filament elongation by formins. *Cell Motility and the Cytoskeleton* **66**:606–617. doi:10.1002/cm.20379

Petersen J, Nielsen O, Egel R, Hagan IM. 1998. FH3, A Domain Found in Formins, Targets the Fission Yeast Formin Fus1 to the Projection Tip During Conjugation. *J Cell Biol* **141**:1217–1228.

Petersen J, Weilguny D, Egel R, Nielsen O. 1995. Characterization of fus1 of Schizosaccharomyces pombe: a developmentally controlled function needed for conjugation. *Mol Cell Biol* **15**:3697–3707.

Pollard TD, Wu J-Q. 2010. Understanding cytokinesis: lessons from fission yeast. *Nat Rev Mol Cell Biol* **11**:149–155. doi:10.1038/nrm2834

Rivero F, Muramoto T, Meyer A-K, Urushihara H, Uyeda TQP, Kitayama C. 2005. A comparative sequence analysis reveals a common GBD/FH3-FH1-FH2-DAD architecture in formins from Dictyostelium, fungi and metazoa. *BMC Genomics* **6**:28. doi:10.1186/1471-2164-6-28

Romero S, Le Clainche C, Didry D, Egile C, Pantaloni D, Carlier M-F. 2004. Formin is a processive motor that requires profilin to accelerate actin assembly and associated ATP hydrolysis. *Cell* **119**:419–429. doi:10.1016/j.cell.2004.09.039

Schönichen A, Geyer M. 2010. Fifteen formins for an actin filament: A molecular view on the regulation of human formins. *Biochimica et Biophysica Acta (BBA) - Molecular Cell Research* **1803**:152–163. doi:10.1016/j.bbamcr.2010.01.014

Scott BJ, Neidt EM, Kovar DR. 2011. The functionally distinct fission yeast formins have specific actin-assembly properties. *Mol Biol Cell* **22**:3826–3839. doi:10.1091/mbc.E11-06-0492

Spudich JA, Watt S. 1971. The regulation of rabbit skeletal muscle contraction. I. Biochemical studies of the interaction of the tropomyosin-troponin complex with actin and the proteolytic fragments of myosin. *J Biol Chem* **246**:4866–4871.

Tang H, Laporte D, Vavylonis D. 2014. Actin cable distribution and dynamics arising from cross-linking, motor pulling, and filament turnover. *Mol Biol Cell* **25**:3006–3016. doi:10.1091/mbc.E14-05-0965

Vavylonis D, Kovar DR, O'Shaughnessy B, Pollard TD. 2006. Model of Formin-Associated Actin Filament Elongation. *Mol Cell* **21**:455–466. doi:10.1016/j.molcel.2006.01.016

Vavylonis D, Wu J-Q, Hao S, O'Shaughnessy B, Pollard TD. 2008. Assembly Mechanism of the Contractile Ring for Cytokinesis by Fission Yeast. *Science* **319**:97–100. doi:10.1126/science.1151086

Vidali L, van Gisbergen PAC, Guerin C, Franco P, Li M, Burkart GM, Augustine RC, Blanchoin L, Bezanilla M. 2009. Rapid formin-mediated actin-filament elongation is essential for polarized plant cell growth. *Proceedings of the National Academy of Sciences* **106**:13341–13346. doi:10.1073/pnas.0901170106

Wu J-Q, Kuhn JR, Kovar DR, Pollard TD. 2003. Spatial and temporal pathway for assembly and constriction of the contractile ring in fission yeast cytokinesis. *Dev Cell* **5**:723–734.

Wu J-Q, Sirotkin V, Kovar DR, Lord M, Beltzner CC, Kuhn JR, Pollard TD. 2006. Assembly of the cytokinetic contractile ring from a broad band of nodes in fission yeast. *J Cell Biol* **174**:391–402. doi:10.1083/jcb.200602032

Yonetani A, Lustig RJ, Moseley JB, Takeda T, Goode BL, Chang F. 2008. Regulation and targeting of the fission yeast formin cdc12p in cytokinesis. *Mol Biol Cell* **19**:2208–2219. doi:10.1091/mbc.e07-07-0731

Zimmermann D, Homa KE, Hocky GM, Pollard LW, De La Cruz EM, Voth GA, Trybus KM, Kovar DR. 2017. Mechanoregulated inhibition of formin facilitates contractile actomyosin ring assembly. *Nature Communications* **8**. doi:10.1038/s41467-017-00445-3

Chapter 5: Probing the mechanoregulation of formin elongation activity using microfluidics

Preface

The work presented in this chapter was performed in collaboration with Cristian Suarez and David Kovar. Cristian Suarez and I developed the experimental protocol. I collected and analyzed the data presented in all figures.

Abstract

Formins are homodimers that nucleate and elongate actin filaments. The structured FH2 domains remain processively associated with the filament barbed end throughout the addition of many new actin subunits. The mostly-disordered FH1 domains bind to profilin-actin in solution to bring new actin monomers to the barbed end of the filament (1). Recent studies have demonstrated two diverging responses of different formin isoforms subjected to tension. Mammalian formin mDia1 and budding yeast formin Bni1 exhibit enhanced elongation activity under tensile forces, which maps to the FH2 domains (2, 3). In contrast, the elongation activity of fission yeast formin Cdc12 was observed to be inhibited by myosin-mediated pulling forces, and the mechanoinhibition mapped to the FH1 domains (4). Here I use a microfluidic system to exert tension forces on actin filaments *in vitro* to probe the mechanoresponse of anchored mammalian formin mDia2. I find two populations of formin-anchored actin filaments. One shows enhanced activity, while the other becomes inhibited. While these results are preliminary, they suggest a model whereby a single formin dimer has two competing force-dependent mechanisms that map separately to the FH1 or FH2 domains.

5.1 Introduction

Formins are a family of homologous proteins that interact with actin by nucleating and elongating actin filaments. These proteins perform an important role in cells by localizing to different regions and altering the assembly of actin locally. By doing this, formins are a major regulator of the higher order actin filament network architecture within a cell that must assemble distinct networks at the correct time and place in order to carry out specific functions.

At the molecular level, formin proteins have two major actin-binding domains in addition to autoinhibitory and signaling domains (1). The actin-binding domains are the FH1 (formin homology 1) and FH2 domains. The FH2 domains are structured and dimerize. This homodimer forms a ring that interacts with an actin filament by remaining processively associated with the barbed end. As new actin molecules are added to the filament barbed end, the FH2 domains 'steps' to the new barbed end (5). The FH1 domains are disordered segments interspaced with polyproline regions, which interact favorably with profilin molecules. Profilin molecules in turn are bound to actin monomers in one-to-one stoichiometry (profilactin). Profilin limits the ability of a bound actin molecule from nucleating or elongating filaments, but through the interactions with formin's FH1 domain, profilactin is brought to the barbed end of the actin filament, and upon being added to the filament, formin catalyzes the release of profilin, enabling further elongation to continue (6). This increases the elongation rate of actin filaments in a pool of profilactin dramatically. Combining these interactions with contrasting interactions whereby profilin inhibits Arp2/3 complex nucleation activity, it becomes clear that formin molecules are powerful regulators of actin filament networks (7).

Different formin isoforms have distinct actin nucleation and elongation properties, and there can exist multiple different isoforms of actin driving differing behavior of the associated actin filaments within a single cell (8). Additionally, recent research has demonstrated that formin

activity can be modulated by tension on the associated actin filament, and that different isoforms of formin are modulated to varying degrees. In some cases the force-responses of different formin isoforms are in completely opposite directions. For example, mammalian formin mDia1 and budding yeast formin Bni1 have been shown to have enhanced actin elongation activity in the presence of piconewton tensions and this appears to map to the FH2 domain (2, 3, 9). In contrast, the fission yeast cytokinesis formin Cdc12 is inhibited by forces exerted by myosin molecules on the associated actin filaments, and this maps to the FH1 domains (4). In this same study, the mammalian formin, mDia2, was observed not to be mechanoinhibited under the same conditions.

The mechanical response of formins is important to understand, as actin filaments under physiological conditions are constantly subjected to mechanical forces. In particular, Cdc12's unique mechanoinhibition was shown to be advantageous to robustly forming a cytokinetic ring in fission yeast both *in vivo* and in coarse-grained modeling (8).

Therefore, we set out to understand the origins of Cdc12's seemingly unique mechanoinhibition. To do this, we pursued a method that would allow us to both control and measure the mode and magnitude of the application of force. This ruled out the use of myosin molecular motors to exert forces on actin filaments because these forces, while potentially being able to be optogenetically turned on and off, could not be precisely controlled nor measured in real time. Instead, we opted to replicate the microfluidics set-ups that had successfully been used to understand the tension-dependent activity of mDia1 and Bni1(10).

Microfluidics systems flow fluid through a chamber with dimensions on the micron scale. By varying the flowrate and chamber dimensions, one can exert and alter the resulting forces experienced by anchored proteins within the sample (11). The work in this chapter describes setting up such an experimental system with the eventual goal of using it to understand the mechanoinhibition of Cdc12. As a control, we used the mammalian formin mDia2, which was

shown not to be modulated by myosin-mediated forces in Zimmermann et al. (4), and instead we observed that its activity is accelerated dramatically by applied force. Additionally, we observed a subpopulation of formin-bound actin filaments that stopped all activity after periods of elongation, which may be mechanoinhibition, but could also be an artifact of the experimental set-up. Further work will be necessary to follow up on these findings to identify the origins of the different modes of actin filament elongation activity.

5.2 Methods

Instructions for making PDMS chambers. Microfluidic masks were designed in Inkscape (example in Fig. 5.1A), converted to monochrome bitmap, and sent to the Pritzker NanoFabrication Facility (PNF) at the Pritzker School of Molecular Engineering at the University of Chicago (Chicago, IL). The channels are represented in black on the mask, which corresponds to raised regions in the silicon mastermold (Fig. 5.1A). These raised regions are then inverted in the eventual polydimethylsiloxane (PDMS) device. The height of the channel is a variable that can be changed for the same mastermold and corresponds to the intensity and/or duration of lithography exposure. Typical height dimensions are between 20 and 100 μm. A best practice is to have the channel depth printed on each of the eventual PDMS molds as it is difficult to determine the depth after the mold has been made.

PDMS was poured according to the following protocol. Combine 56 g of elastomer base with 5.6 g of PDMS curing agent (10:1 ratio) in a plastic weigh boat. Place weigh boat in a vacuum chamber, establish a vacuum, and let sit until gas bubbles are released from the PDMS mixture. Place the silicon wafer mastermold into a container that will hold PDMS; one can be made simply by forming aluminum foil tightly around the mastermold. Pour PDMS mixture onto the silicon wafer. Place back into vacuum chamber to release any bubbles that formed while pouring the

mixture. Cure the PDMS by cooking it on a hot plate set to 65° C for 4 hours. Allow to cool and peel off the cured PDMS carefully so as not to break the silicon wafer. Cut the PDMS chambers into sections using a razor blade. Punch holes into the PDMS so that the inlet tubing can access the channel. To do this, use a biopsy punch with an outer diameter that closely matches your tubing dimensions (0.75 mm) works well. Use PDMS section immediately, or store at room temperature in a covered petri dish or in cling wrap for later use. If these do not dry out, they last more or less indefinitely.

Fisherbrand™ Cover Glass 24 x 30 mm (product ID: 12545B) was cleaned by agitation in alternating baths of acetone, isopropanol, milliQ water for 7 minutes each. Then it was placed in a sonication bath filled with isopropanol for 30 minutes. The glass was stored in milliQ water. The cleanness of the glass is important for eventual coating of the glass with PLL-PEG.

Before the experiment, remove one piece of stored glass and allow it to fully dry. Place glass and cured PDMS mold into plasma cleaning machine on medium for 12 seconds. Remove and bond together tightly, channel-side of the PDMS facing the glass.

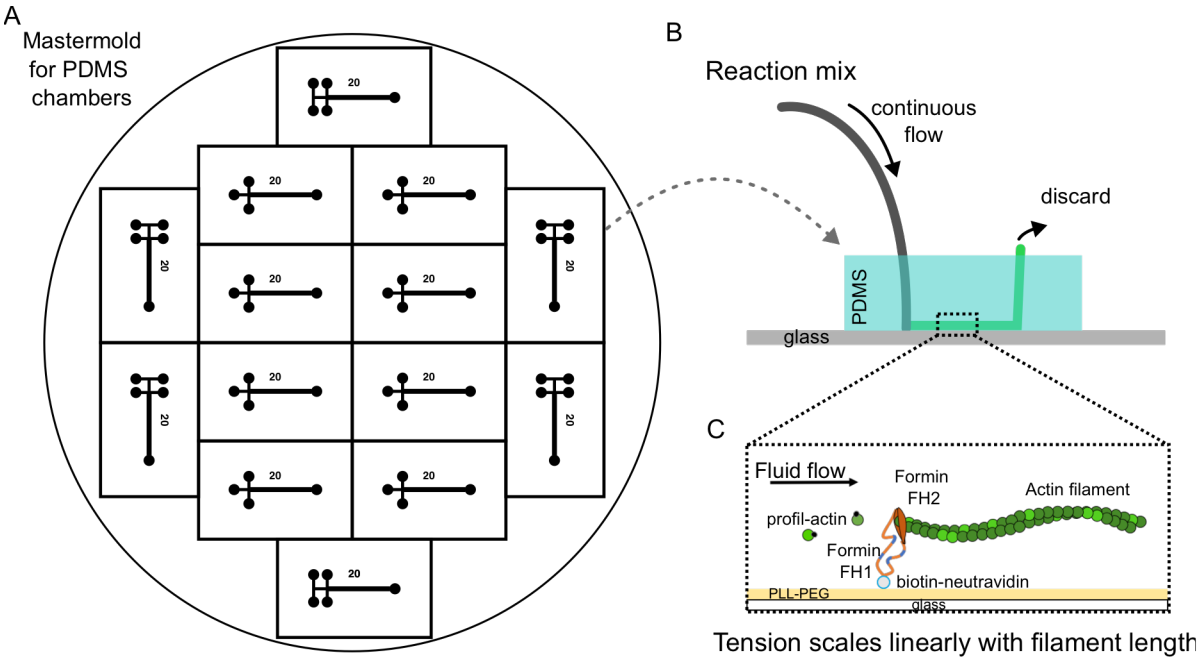

Figure 5.1. Schematic of the experimental system.
(A) An example of a microfluidic mask. Black regions are raised in the silicon mastermold onto which PDMS will be poured, creating channels in the final molds. Each rectangle contains a different channel with three or four inlets for different types of experiments. The number (in this case 20) is the depth of the eventual channels in microns. (B) Schematic of the PDMS channel fused to a coverslip with the actin mix being added continuously to produce a constant flow within the chamber. The coverslip is placed on the TIRM objective for imaging. (C) Zoom in at the single filament level. The glass is coated with PLL-PEG with a small percentage of PEG fused with biotin. Neutravidin is flowed in to bind tightly to the biotinylated PEG followed by formin molecules with biotin tagged to their FH1 domains. The FH2 domain is processively associated with the barbed end of an actin filament. A solution of profilactin is flowed in continuously to exert force and supply profilactin monomers for formin-mediated elongation. The tension exerted by fluid flow scales linearly with the length of the filament.

PDMS chambers were prepared by flowing in 0.1% PLL-PEG biotin at a concentration of 1 mg/mL to fill the channel volume and waiting 30 minutes. This was followed by a HEK-BSA wash. Then 100 μg/mL neutravidin was flowed and allowed to sit in the chamber for 5 minutes. HEK-BSA was flowed in to wash. Following this, 330 nM FH1 biotin-tagged mDia2 was flowed in and allowed to sit in the chamber for 5 minutes. HEK-BSA was used to wash out remaining formin. The chamber was slightly overfilled so that droplets covered the inlet(s) and outlet. The slide and chamber were then placed on the TIRF (total internal reflection fluorescence) microscope objective.

The actin mixture was prepared by first combining 80 μL of 9μM 10% Alexa-488 labeled actin with 16 μL 5xME. In a separate epindorf tube, combine 339 μL 1xKMEI, 20.8 μL of 35 μM profilin (Cdc3), 16 μL catalase glucose oxidase, and 8 μL of 1 M glucose. Combine the two mixtures and place in a epindorf tube with a screw top that interfaces with the microfluidic system. Note that the actin mixture lacks methylcellulose, the crowding agent typically used in TIRF experiments (12). We used the Fluigent Flow EZ™ to apply pressures between 0 and 345 mbar (Part number: LU-FEZ-0345). Pressure was applied to flow the actin mixture through the inlet tubing until a liquid droplet began to exit, at which point the pressure was set to 0. The droplet of the inlet tubing was placed in contact with the droplet on the inlet hole of the PDMS chamber. This liquid-liquid interface is important to make sure no air enters the chamber. Once the inlet tubing was securely placed, the pressure was increased gradually to allow liquid to flow into the chamber and imaging began. Periodically, the discard droplet at the outlet hole was wicked using a KimTech kimwipe. A schematic of the set-up is depicted in Fig. 5.1B. The desired system at the molecular level is illustrated in Fig. 5.1C.

In these initial experiments, we did not make measurements of the flow, but in future experiments, flow measurements would be desirable to allow calculation of the tension on the actin filaments. The theory behind calculations of filament tension from flow measurements is explained in detail in Jegou et al. and Wioland et al. (3, 11). For this work, the important relationship to highlight from theory is that tension scales linearly with filament length (3). That is, points along the filament are under tension proportional to the length of the filament downstream of that point.

Data was analyzed using ImageJ and the KymographBuiler plugin.

5.3 Results

Three populations of actin filaments are present in *in vitro* the microfluidic TIRF assay. In microfluidics TIRF experiments, anchored filaments are aligned within the TIRF field (Fig. 5.2A). This indicates that the experimental set-up succeeded in two key ways. First, actin filaments have been attached to the glass. Under continuous flow, unattached filaments would flow through the field of view instead of remaining stationary for prolonged periods of time. Second, fluid flow is exerting force on actin filaments. The fact that the filaments are aligned and even visible in the TIRF region (~200 nm above the glass), indicates that flow is pushing filaments down and in alignment with the fluid flow gradient. In typical in vitro TIRF experiments, a crowding agent, often methylcellulose, is used to concentrate the sample near the glass. However, in these microfluidic experiments, no crowding agent is used, and instead the flow forces the filaments to the surface of the glass. One also observes the effect of flow, perhaps more directly, by the fact that the filaments are aligned with respect to each other. In this way, the filaments act as ‘tracers’ of the direction, magnitude, and uniformity of the flow. The end of the filament farthest from the anchoring point comes in and out of focus as it goes in and out of the TIRF field. This indicates that the forces on regions of the actin filament are not uniform along the length of the

filament, in agreement with theory (see Methods), which states that force along the filament is linearly proportional to the distance from the anchoring point (i.e. proportional to the length of filament upstream from that point).

At a single filament level, we observed three subpopulations of actin filament behavior. These subpopulations were identified based on their different elongation characteristics. Because the actin used in these experiments is 10% labeled with Alexa488 fluorophore, regions of polymerized actin randomly have higher or lower percentages of labeled actin. This allows for tracking of fiducial marks along the actin filament as brighter or darker regions of the filament emerge. In particular, because actin polymerizes two orders of magnitude faster at the barbed end than the pointed end, one can determine which end of the filament is anchored. If the fiducial marks appear stationary as the filament elongates, then the filament is anchored by its pointed end. If instead, the filament is anchored by its barbed end (i.e., where formin is), then as the filament elongates, the fiducial marks move at the rate of elongation. This gives the appearance of the fiducial marks 'flowing' from the anchoring point.

We see populations of actin filaments anchored by both the barbed and pointed end. Filaments bound by the barbed end also showed two types of behavior. One population elongated and then stopped elongating. These did not restart elongation on the timescale of the experiment. Another population elongated continuously and clearly showed accelerated polymerization activity as a function of time and filament length.

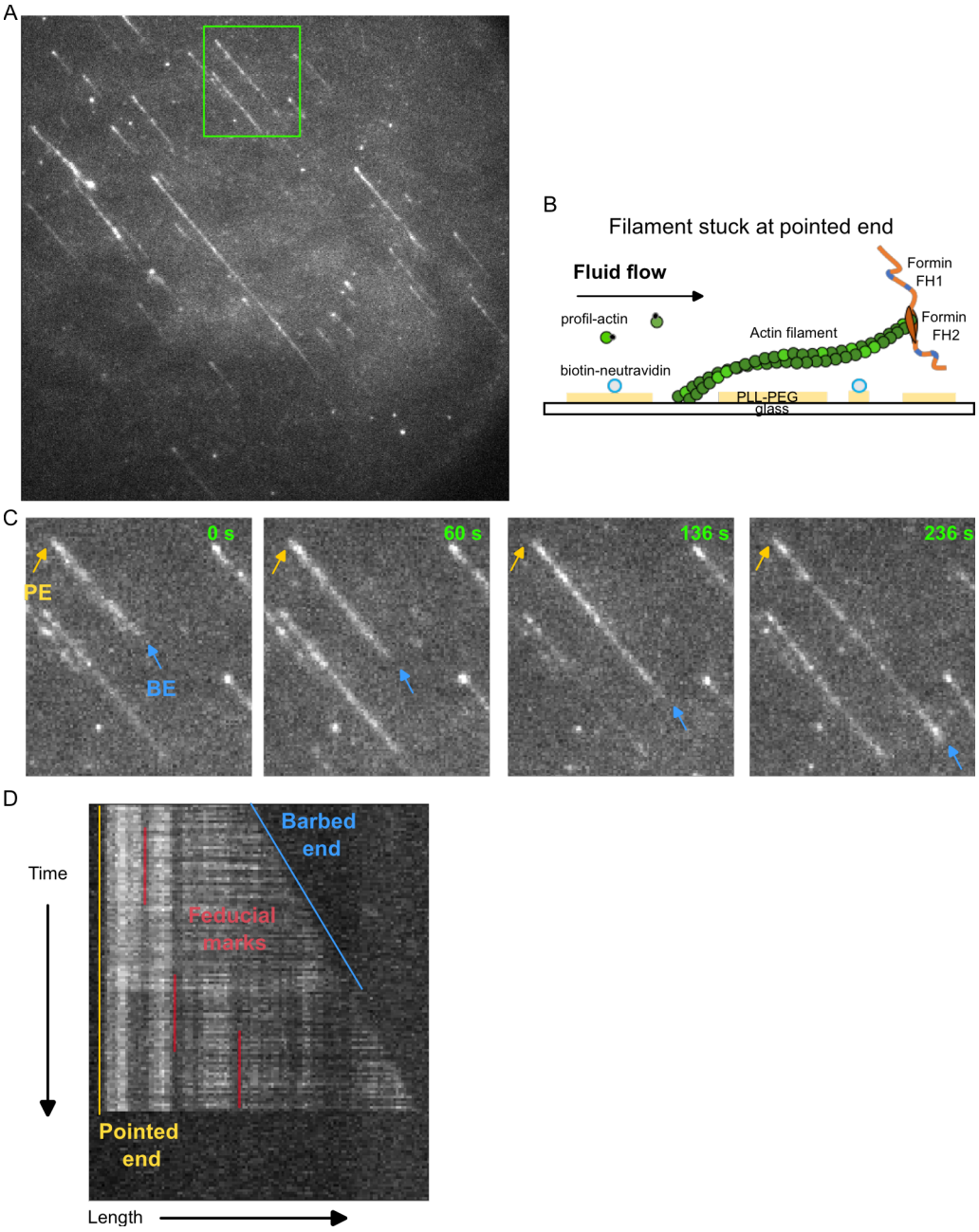

Figure 5.2. Filaments anchored by their pointed ends elongate linearly and continuously. (A) Entire field of view of TIRF experiment containing three subpopulations of filaments exhibiting distinct behavior. Representative filament anchored by the pointed end is highlighted. (B) Schematic depicting how the filaments belonging to this subpopulation are likely bound to the coverslip. (C) Snapshots of the actin filament elongating continuously. The barbed and pointed ends are marked with blue and yellow arrows, respectively. (D) Kymograph of actin filament elongation over time. Fiducial markings are clearly stationary even as the length of the filament increases (red), indicating the filament is anchored by the pointed end. The elongation rate is linear. The time axis is 2 seconds per frame and the length axis is 160 nm per pixel. The actin, profilin, and mDia2 concentrations are 1.5, 1.5, and 0.33 μM, respectively.

Filaments anchored by the pointed end elongate at a constant rate. Although our intentions were to only have filaments anchored by the FH1 domains of formin, we observed actin filaments that clearly maintained stationary fiducial marks as they elongated (Fig. 5.2C, D). At the molecular level, we hypothesize that the coating of the glass with PLL-PEG, to which proteins do not normally bind with high affinity, was imperfect and left regions of the glass exposed, which allowed actin filaments to become stuck by their pointed ends (Fig. 5.2B). These filaments elongated at a constant rate of ~20 subs s-1 at 1.5 μM actin (Fig. 5.2D). We could not determine if the filaments were being elongated with the presence or absence of formin at the barbed end because the elongation rates of formin-mediated assembly for mDia2 is roughly the same as bare actin filaments (Kovar Cell 2006).

Filaments anchored by mDia2 at the barbed end can stop elongating. We observed another population of actin filaments that initially elongated with moving fiducial markings consistent with elongation from a barbed end bound to an anchored formin. Interestingly, while these filaments initially polymerized, at some point they stopped elongating completely (Fig. 5.3C). This was unexpected and has not been reported for other formins. In particular, the only study to report mechanoinhibition of formin observed that mDia2 was not inhibited by force. Nonetheless, the elongation behavior that we observed clearly shows an initial flow of fiducial marks followed by a period of no elongation (Fig. 5.3D). We are not sure what is causing this behavior, but it may be the result of the profilin not being released from the barbed end, the FH1 domains becoming tangled or mechanoinhibited, but most likely this is the result of the actin filament itself becoming anchored in a second location (Fig. 5.3B), which can cause geometrical constraints that limit elongation (Suzuki Nano Lett 2020).

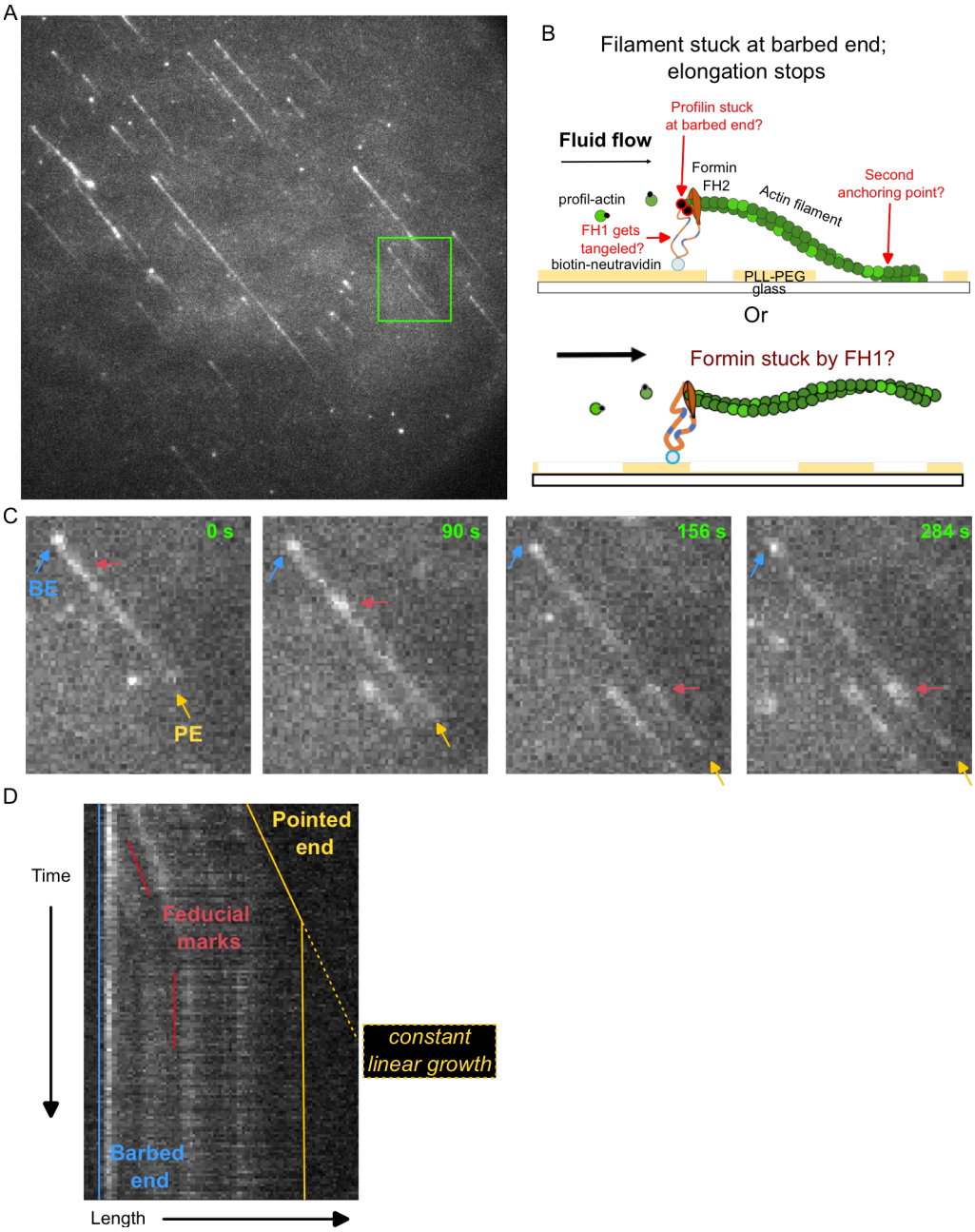

Figure 5.3. Some filaments anchored by their barbed ends elongate then stop.
(A) Entire field of view of TIRF experiment containing three subpopulations of filaments exhibiting distinct behavior. Representative filament anchored by the barbed end with stopping behavior is highlighted. (B) Schematic depicting how the filaments belonging to this subpopulation are likely bound to the coverslip. Possible reasons for why stopping occurs are annotated in red. (C) Snapshots of the actin filament initially elongating and then stopping. The barbed and pointed ends are marked with blue and yellow arrows, respectively. Fiducial marks are marked by red arrows (D) Kymograph of actin filament elongation over time. The filament length initially increases and fiducial marks follow the same slope, indicating the filament is anchored by the barbed end. The elongation suddenly drops to approximately zero partway through the experiment, as seen by stationary fiducial marks (red) and pointed end.

Figure 5.3. continued: The time axis is 2 seconds per frame and the length axis is 160 nm per pixel. The actin, profilin, and mDia2 concentrations are 1.5, 1.5, and 0.33 μM,

Filaments anchored by mDia2 at the barbed end can elongate at an accelerating rate. In contrast, we also observed a filament that was clearly elongating from an anchored barbed end, as fiducial marks flowed out from the anchoring point (Fig. 5.4D). However, instead of elongating at a constant rate or stopping, this filament elongated with an accelerating rate. This was apparent in the kymograph, which showed fiducial marks and the pointed end moving with increasing rates (Fig. 5.4D). We believe that this represented the desired experimental setup, whereby the filament was anchored via a bound formin molecule attached to the glass by its FH1 domain (Fig. 5.4B), but it also could have been a formin molecule electrostatically attached to the coverslip by its FH2 domain.

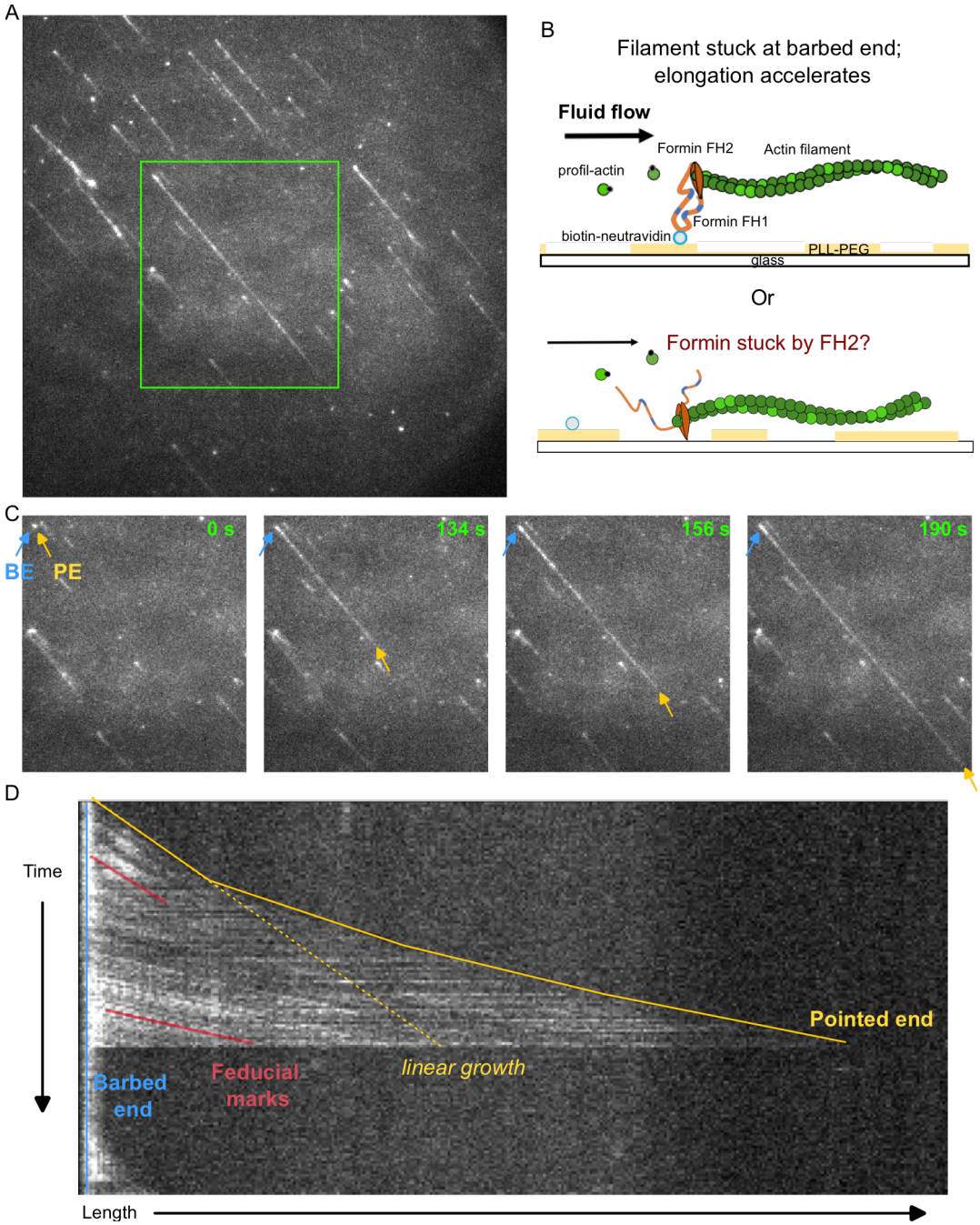

Figure 5.4. One filament anchored by the barbed end displays accelerating elongation. (A) Entire field of view of TIRF experiment containing three subpopulations of filaments exhibiting distinct behavior. Representative filament anchored by the barbed end with accelerating activity is highlighted. (B) Schematic depicting how the filaments belonging to this subpopulation are likely bound to the coverslip. (C) Snapshots of the actin filament elongating. The barbed and pointed ends are marked with blue and yellow arrows, respectively. (D) Kymograph of actin filament elongation over time. The filament length increases at an accelerating rate and fiducial marks follow the same length-dependent slope (red). The time axis is 2 seconds per frame and the length axis is 160 nm per pixel. The actin, profilin, and mDia2 concentrations are 1.5, 1.5, and 0.33 μM, respectively.

Because the pointed end anchored filaments were also in the same field of view, we used them as internal control filaments to compare to the behavior of the accelerating filament. Observing the length of the filaments as a function of time showed that elongation of the pointed end anchored filaments all showed similar elongation rates throughout the experiment (Fig. 5.5A). Comparing the elongation rate as a function of filament length, which is linearly proportional to the tension on the anchoring point of the filament (i.e., the formin), revealed that the pointed end anchored filaments showed no clear dependence of elongation rate on tension. In contrast, the FH1-anchored filament showed a striking dependence on tension, which appeared to be a linear dependence by eye for this range of forces. The elongation rate increased ~8-fold from a baseline

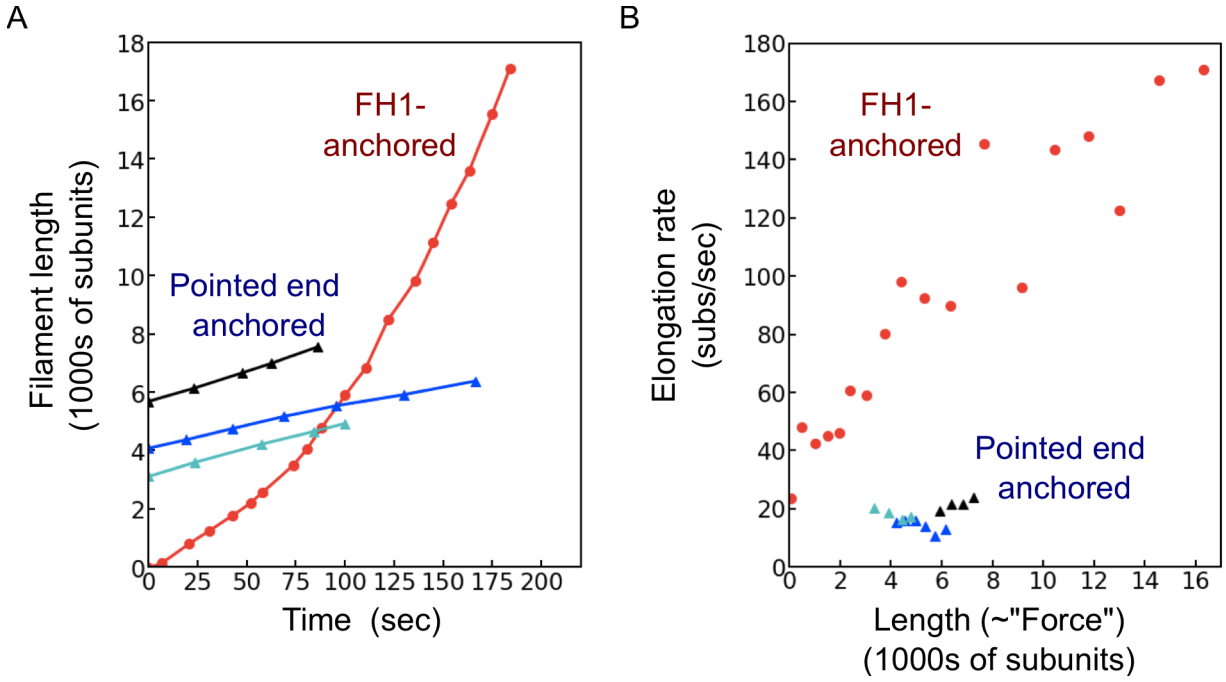

Figure 5.5. Distinct filament subpopulations show different force-dependent behavior. (A) Filament length is plotted as a function of time for filaments anchored by the pointed end (blue, cyan, black) and by the barbed end without stopping (red). Pointed end anchored filaments grow linearly, whereas the barbed end anchored filament accelerates. (B) Instantaneous elongation rate is plotted as a function of filament length for the filaments tracked in (A). Pointed end anchored filaments all polymerize at a constant rate of ~20 subs s^{-1} (~13 subs s^{-1} μM^{-1} actin), whereas the filament anchored by its barbed end elongates at a rate between ~20 subs s^{-1} and ~170 subs s^{-1}, which appears to be roughly linearly dependent on the filament length.

of ~20 to over 160 subs s-1 at 1.5 μM actin (Fig. 5.5B). For these experiments, we did not measure the flow rate, so we cannot estimate the force the mDia2 was subjected to.

5.4 Discussion

Enhanced activity of mDia2 under tension. mDia2 appears to be enhanced by tension. For other formins with that have enhanced actin elongation activity, the origins of this behavior has been traced to the FH2 domain. The current model is that tension helps the FH2 domain 'step' to the barbed end of the filament after the addition of a new actin subunit. It is reasonable to hypothesize that the activity of mDia2 is enhanced by a similar mechanism, but this would need to be explored. One possible way to do this would be to repeat these experiments with the FH2 domain biotinylated instead of the FH1 domain. When the FH1 is anchored, both FH1 and FH2 is subjected to strain, whereas with FH2 anchoring, only the FH2 domains are under tension. This insight can be used to infer which of the two domains is responsible for the behavior.

The mechanosensitve response of mDia2 is much larger compared to what has been observed for mDia1. When similar experiments were performed for mDia1, Jegou et. al observed force accelerated elongation by 2-fold from a no-force baseline of ~45 subs s^{-1} μM^{-1} to ~90 subs s^{-1} μM^{-1} (3). We see a much stronger increase of ~8-fold. Particularly interesting is that mDia1 at baseline values assembles ~45 subs s^{-1} μM^{-1}, whereas mDia2 assembles ~4 times slower at ~12 subs s^{-1} μM^{-1}. However, at the highest forces assessed, mDia1 assembled at ~90 subs s^{-1} μM^{-1} and mDia2 in the experiment presented here assembles at over 105 subs s^{-1} μM^{-1}. It is possible that our highest tensions exceeded those reported for mDia1, and at comparable tensions mDia1 would have had even higher elongation rates. To know for certain, one could repeat these experiments measuring the flow to calculate the forces

Inhibited activity of mDia2 under tension. We observe a subpopulation of actin filaments that clearly elongate from the barbed end based on analysis of the fiduciary marks, but that cease all elongation partway through the experiment (Fig. 5.4). It seems possible that this is the result of an undesirable characteristic of the experimental system that should be avoided via troubleshooting, for instance, the filament itself becomes stuck to the glass, constraining the filament and limiting elongation.

However, it is also possible that this is a meaningful result and should be investigated further. One possibility is that this behavior may be caused by a force-independent mechanism, such as 'clogging' of the barbed end by unreleased profilin, which was observed to be a rate-limiting step at high concentrations of profilactin (6). If this were true however, then this stopping behavior should be observed in a subpopulation of non-microfluidic TIRF experiments.

It could also be caused by a force-dependent mechanism, perhaps the same that underlies inhibition of Cdc12. In the case of Cdc12, mechanoinhibition was mapped to the FH1 domains. If it is the same mechanism, then this could be tangling of the FH1 domains, which may only occur rarely, but when it does, it shuts off elongation entirely. One possible explanation for the two types of behavior we observe here for filaments anchored by the barbed end is that the inhibited ones are anchored through the biotinylation of their FH1 domains, whereas the accelerated one is anchored via an electrostatic interaction with the coverslip itself, similar to how the pointed end anchored filaments are presumably attached (Fig. 5.4). Therefore, the FH2 domain would be under tension and the FH1 domains would not because FH1 is upstream of FH2.

One can imagine that there are competing force-responses in the FH1 and FH2 domains present in all formin isoforms. This would make it difficult, but even more interesting, to isolate the various mechanisms.

Considerations for using a microfluidic system. Microfluidics is a valuable tool to study the actin cytoskeleton. There are several key advantages over traditional TIRF microscopy experiments.

First, the user is able to both measure and actively control forces subjected to actin filaments as well as ABPs. In terms of control, this includes both the type of force applied (e.g., tension, bending) as well as the magnitude of the force. One can imagine this being useful for experiments such as the one featured here where an anchored ABP is subjected to tension. However, one could also imagine scenarios where the actin filament itself is under flow-induced strain, such as in the study of the mechanoresponsive binding of LIM domains. For this example, flow could be used to induce a length-dependent tension to actin filaments and analyzing the binding kinetics of various LIM domains, or alternatively perpendicular channels could be used to exert bending forces on filaments initially aligned (and anchored) to flow at a 90° angle. This procedure was used to investigate cofilin's mechanosensitivity (11), and a similar set-up may prove useful for evaluating mechanosensitivity of LIM domains with precision and in a myosin-independent manner.

Second, the method is high throughput. This is because a single field of view contains many filaments of various lengths. With a constant flow at all regions of the field of view, one experiment can yield measurements of biochemical activity of molecules subjected to a wide range of forces. Additionally, because the filaments are aligned and anchored, analysis is made much easier. One can easily track filaments over time, and they very rarely cross each other – a property that has made it difficult to automate the tracking of actin filaments, which is largely done by hand. Relatedly, because the filaments under tension are largely straight, tracking a single filament by hand is remarkably easy. Instead of going frame by frame and tracing the contour of a moving and wiggling filament with a segmented line, a single line at a single frame can be used to generate a

kymograph of the entire lifetime of that filament because its anchoring point keeps it from moving and the flow keeps it straight.

Third, microfluidics can be used to perform buffer exchange with minimal fluid forces applied to the sample. In traditional flow chambers, changing the buffer in the middle of an experiment typically means pushing everything in the field of view out if it is unattached, or subjecting the filaments to mechanical force exerted by the fluid if the filaments are anchored, resulting in fragmentation. This introduces a confounding variable, especially if the readout is something like severing rate, as would be expected for studies involving flowing in cofilin. Microfluidics can be used with no- or low-flow chambers to exchange buffer without introducing the fluid forces (13).

There are several noteworthy disadvantages. For one, experimental set-up takes considerably longer than traditional TIRF flow chambers, as only one PDMS channel is prepared at a time, and these require long incubation periods. So, although each experiment can have high throughput, fewer experiments can be performed per day in general. Secondly, flow is required to keep filaments anchored at one attachment point, as was desired in this project, close to the glass to remain in the evanescent wave to achieve good signal in TIRF microscopy. In traditional TIRF microscopy, one uses methylcellulose as a crowding agent to keep the sample close to the glass, but this is not the case in TIRF. Therefore, one is not easily able to turn off the flow mid-experiments and maintain a clear measurement of the filaments.

5.5 References

1. D. Zimmermann, D. R. Kovar, Feeling the force: formin's role in mechanotransduction. *Curr Opin Cell Biol* **56**, 130-140 (2019).

2. N. Courtemanche, J. Y. Lee, T. D. Pollard, E. C. Greene, Tension modulates actin filament polymerization mediated by formin and profilin. *Proc Natl Acad Sci U S A* **110**, 9752-9757 (2013).

3. A. Jégou, M. F. Carlier, G. Romet-Lemonne, Formin mDia1 senses and generates mechanical forces on actin filaments. *Nat Commun* **4**, 1883 (2013).

4. D. Zimmermann *et al.*, Mechanoregulated inhibition of formin facilitates contractile actomyosin ring assembly. *Nat Commun* **8**, 703 (2017).

5. F. Aydin, N. Courtemanche, T. D. Pollard, G. A. Voth, Gating mechanisms during actin filament elongation by formins. *Elife* **7** (2018).

6. J. Funk *et al.*, Profilin and formin constitute a pacemaker system for robust actin filament growth. *Elife* **8** (2019).

7. C. Suarez *et al.*, Profilin regulates F-actin network homeostasis by favoring formin over Arp2/3 complex. *Dev Cell* **32**, 43-53 (2015).

8. K. E. Homa *et al.*, Formin Cdc12's specific actin assembly properties are tailored for cytokinesis in fission yeast. *Biophys J* **120**, 2984-2997 (2021).

9. M. Yu *et al.*, mDia1 senses both force and torque during F-actin filament polymerization. *Nat Commun* **8**, 1650 (2017).

10. N. Courtemanche, T. D. Pollard, Determinants of Formin Homology 1 (FH1) domain function in actin filament elongation by formins. *J Biol Chem* **287**, 7812-7820 (2012).

11. H. Wioland, A. Jegou, G. Romet-Lemonne, Torsional stress generated by ADF/cofilin on cross-linked actin filaments boosts their severing. *Proc Natl Acad Sci U S A* **116**, 2595-2602 (2019).

12. D. Zimmermann, A. N. Morganthaler, D. R. Kovar, C. Suarez, In Vitro Biochemical Characterization of Cytokinesis Actin-Binding Proteins. *Methods Mol Biol* **1369**, 151-179 (2016).

13. T. Cambier *et al.*, Design of a 2D no-flow chamber to monitor hematopoietic stem cells. *Lab Chip* **15**, 77-85 (2015).

Chapter 6: Conclusion and Future Directions

Throughout my graduate research, I have set out to shed light on the mechanisms driving biomolecular behavior of major components of the actin cytoskeleton, namely actin, formin, and LIM domains.

In Chapter 2, I reported that a single mechanistic heuristic drives why and how actin filaments exhibit polarized elongation – actin subunits at filament ends tend towards the twisted conformation of actin monomers. In hindsight, this mechanism is intuitive. The key difference between the environment surrounding an actin molecule in solution and an actin molecule in the filament interior is the presence of four neighboring subunits that together make contacts with each subdomain of the molecule, keeping it in a flattened conformation. At the barbed and pointed ends, terminal subunits are lacking one or two of the neighboring subunits. Put another way, the environments for the terminal subunits are partway between that of a monomer and a subunit within the filament interior, and as a result, the subunits in these positions take on conformations partway between that of a monomer in solution and a subunit within the filament interior. Importantly, the set of neighboring subunits that the actin molecule at each of the terminal positions within a filament is lacking is unique. Therefore, each subunit has a unique landscape in conformational space that it explores.

At the barbed end, the terminal subunit is observed to have almost an entirely monomeric conformation with a twisted dihedral angle. This precludes it from making contact with the laterally neighboring subunit B-1, and so it dangles with its sole attachment to the filament being its D-loop's connection with the W-loop of subunit B-2, its longitudinal neighbor. Not only does this explain the fast off rate of the barbed end subunit, as it has only one connection, but this also points clues to the fast on rate for an incoming monomer attaching to subunit B-1. By fluctuating,

the terminal subunit is separated from subunit B-1, which allows incoming monomers unobstructed access to B-1.

At the pointed end, the penultimate terminal subunit P-1 also takes on a twisted dihedral angle characteristic of monomers in solution. However, this same mechanistic principle leads to an almost opposite effect as at the barbed end. Instead of losing contact with neighboring subunits that would normally be present within filament interiors, P-1 makes a novel connection with the terminal subunit P. This is mediated by the D-loop of subunit P-1, which binds to the side of subunit P. Put another way, without the longitudinal neighbor present to interact with, the D-loop of P-1 forms a connection with the lateral neighbor instead of simply dynamically exploring the surrounding solvent. Due to this, the D-loop of P-1 is unavailable for binding new actin monomers that collide with the filament end, limiting pointed end elongation. Additionally, due to the additional contact between subunit P and P-1, the pointed end is very stable and fluctuates at levels comparable to or even below that of subunits within the filament interior. This explains why the off rate is slow at the pointed end as well.

This project led to new mechanistic insight into one of the most well-known properties of actin filaments, which did not have a satisfying explanation prior to this study. Not only did it explain results that had already been known, but it also made predictions for future studies in anticipation of groups eventually overcoming the challenges making cryo-EM structures of the filament ends difficult to acquire. First, because the barbed end subunit is so dynamic in simulations, I proposed that this subunit should have very weak density in cryo-EM reconstructions compared to the other subunits in the same experiment. I also claimed that because the barbed end subunit is in a twisted conformation, and subunit flattening is what catalyzes ATP-hydrolysis, the barbed end subunit should be in the ATP state. Conversely, the pointed end subunit

P was observed to switch between a twisted and flattened conformation through its interaction with subunit P-1, promoting ATP-hydrolysis at this end.

Only now are structures of the filament ends being solved via cryo-EM at high resolution (2, 3). These structures confirm the hypotheses described above. At the barbed end, there is weak density of subunit B, consistent with a highly dynamic, minimally attached terminal subunit (Fig. 6.1A). It is resolved enough to make the determination that the bound nucleotide is in the ATP state. At the pointed end, subunit P-1 can be seen to have a monomeric conformation by which its D-loop is pointing towards subunit P, consistent with the unique lateral connection observed in my MD simulations. Additionally, the pointed end subunits are in the ADP state (Fig. 6.1B).

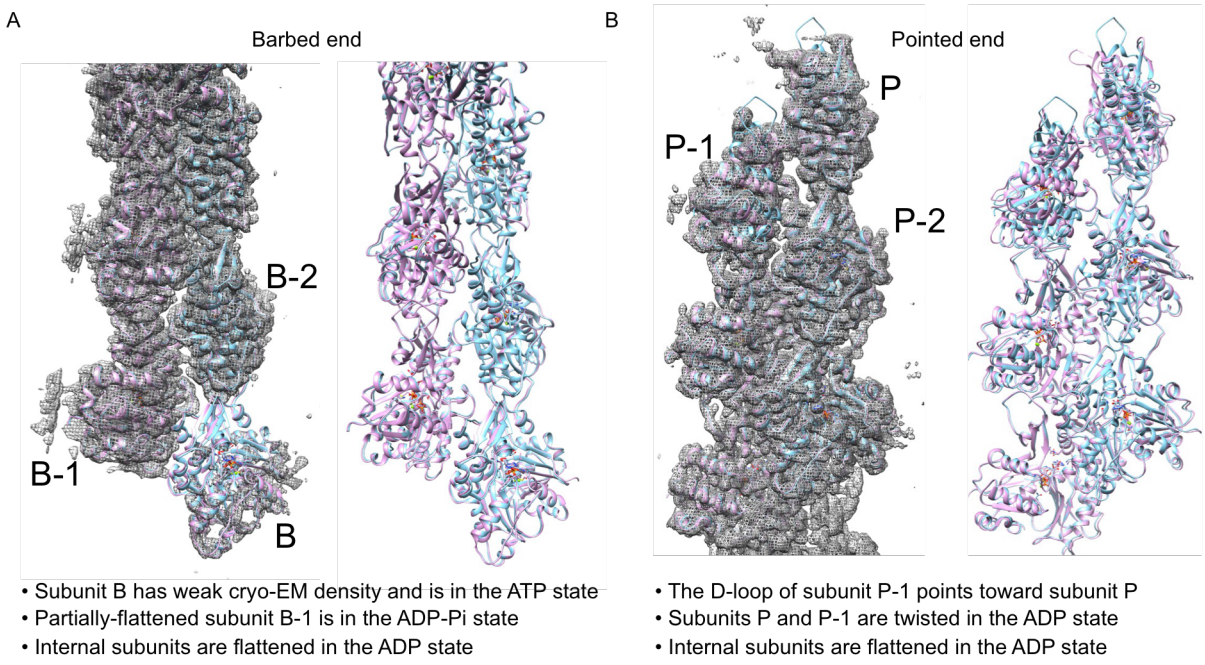

Figure 6.1. Newly resolved cryo-EM structures of the barbed and pointed ends of bare actin filaments.
(A) Ribbon diagrams of the barbed end subunits with (left) and without (right) accompanying cryo-EM density. Structural features of the barbed end subunits that were predicted in Zsolnay et al. PNAS 2020 are listed below (1). (B) Ribbon diagrams of the pointed end subunits with (left) and without (right) accompanying cryo-EM density. Structural features of the pointed end subunits that were predicted in Zsolnay et al. PNAS 2020 are listed below (1). Data comes from Steven Chou and Thomas Pollard (2) .

Another structure has recently been reported in a preprint to bioRxiv, which reports the barbed end of a phalloidin-stabilized filament (3). This has strong density for the barbed end subunit, suggesting phalloidin reduces the dynamics of the terminal subunit. I am curious why the authors of this study reported structures including phalloidin but not those without, and if omitting phalloidin resulted in an unaccounted-for density at the barbed end.

In the future, one could imagine using enhanced sampling methods to observe the dissociation of actin subunits at both filament ends and connect the resulting free energy of the unbinding pathway to the reported off rates. Additionally, one could look at the effect of the bound nucleotide on these rates, which can change dynamics ~4 fold between ATP-bound and ADP-bound terminal subunits. These studies should be modeled after similar ligand-unbinding computational studies.

In Chapter 3, I reported an intermediate metastable state between a fully intact and fully fragmented filament. This cracked state exists when one protofilament of the actin filament breaks, while the other protofilament remains intact. I show that the crack is a force-activated binding site for mechanosensitive LIM domains. I suggest that these may be identifiable in cryo-EM and I encourage structural biologists to investigate this possibility.

I imagine three obvious follow-up studies based on these results. First, I focused primarily on cracked actin interface as a mechanosensitve receptor in my research, but an equally interesting question is what on the LIM domain drives mechanosensitve binding to this site. I believe much of the data required to generate a strong hypothesis already exists in the dataset of docking simulations that I collected for 43 distinct LIM domain sequences. One would need to analyze which residues in the bound LIM domains are driving the favorable binding interactions, and likely this information would need to be used in concert with a complementary multiple sequence

alignment library. From these hypotheses, a researcher could mutate LIM residues to change test the behavior *in vivo* or *in vitro.* Furthermore, one could identify LIM domains that they predict to be mechanosensitive based on sequence alone. This could be done by BLAST search or even by engineering new protein sequences.

Second, other molecules, protein or otherwise, may bind to cracks in actin filaments. Using docking simulations in a high throughput manner, one could attempt to identify proteins or even small molecules that would bind to cracked interfaces. For protein molecules, this could suggest new pathways for mechanotransduction and signaling activities. For drug molecules, I would initially be interested in what the effect of such a drug is on the behavior of actin filaments *in vitro* and *in vivo.* Would the introduction of such a drug inhibit the cell's ability to recognize damaged filaments by outcompeting LIM domains for cracked interfaces?

Third, in the discussion of Chapter 3 I discussed experimental results of an actin mutation of residue 169 to a serine (4) in the context of my finding that residue Y169 of subunit i-2 was in a flipped orientation away from the D-loop of subunit i at all breaking interfaces. I can imagine an initial computational study where Y169 is mutated and assessing the probability that residue 169 interacts with the D-loop of the neighboring subunit. My initial trials would be Y169F, the WT residue in yeast actin, Y169S, for which there is experimental data, and perhaps Y169A. Y169F is a great choice because this actin should nucleate and polymerize, as it is WT yeast actins, but if there is a difference in flipped prevalence, then perhaps this would translate into a difference in severing or depolymerization rates in the absence of severing proteins like cofilin.

Future studies may also want to follow up on the explanation for why tandem LIM domains separated by 7-8 amino acid linkers enhance mechanosensitive binding that I proposed in Chapter 3. Briefly, I observed that there were two LIM binding sites at a single cracked interface, and the separation between them is consistent with the distance between LIM domains in

mechanosensitive sequences. Aside from structural studies that would directly observe this binding interaction, it is difficult to imagine a great experimental approach to test this idea. Computationally, one could imagine initiating a simulation with a LIM domain bound to one of the crack sites with a tandem LIM domain unbound and observing what the diffusive search of the unbound LIM domain looks like. There may be an advantage of doing this in a coarse grained (CG) model for better exploration of the complete conformational search space.

In Chapter 4, I introduce a collective variable (CV) that is capable of tracking incremental progress towards ring assembly in a system representing a fission yeast cell (5). Future studies may use this metric to explore the free energy landscape associated with ring assembly. This CV could be useful to identify where bottlenecks lie in the formation of a cytokinetic ring, how energetically favorable spontaneous ring assembly is under baseline conditions, and how this landscape changes for different phenotypes associated with, for instance, formins with different actin assembly properties, but also the presence of different cross linkers. Previous studies characterized the emergent actin network architecture and if it formed a ring by eye, which lacked efficiency and reproducibility. Even algorithmic ring detection with binary results (i.e., 1 for a ring, 0 for not a ring) could not be used as an effective CV as it is impossible to know if the added bias potentials are pushing the system closer or farther from a fully formed ring. However, this computational model would likely need to be rewritten in a program, such as LAMMPS, that interfaces with enhanced sampling software, such as PLUMED. Finally, this CV may prove a useful metric for understanding 3-dimensional results of experiments reconstituting ring assembly *in vitro* (6).

In Chapter 5, I reported preliminary results from an *in vitro* microfluidics set-up. These suggested that mammalian formin mDia2 is potentially mechanosensitive in two ways. One population of filaments anchored by formins at the barbed ends initially elongated and then stopped. Another subpopulation of formin-anchored filaments elongated continuously with an elongation rate that accelerated by almost an order of magnitude. One particularly interesting potential explanation for these two subpopulations and their very different behaviors is that one is stuck down by the FH1 domain, which conveys mechanoinhibition, and another is stuck by the FH2 domain, which conveys increased elongation under force. Because the FH1 domain is farther from the filament than the FH2 domain, if the formin is anchored by the FH2, the FH1 domains will not be subjected to tension, and therefore the effect of FH2 under tension on filament elongation is maximized. If on the other hand, FH1 is anchored and force stops almost all polymerization, then the accelerated 'stepping' of FH2 under tension has no effect, and FH1 inhibition dominates. This idea, while nascent, would be exciting, and potentially explain why different formins appear to behave so differently under tension, and yet are very similar both in sequence and in structure. This would suggest that all formins have these competing force-responses of the FH1 and FH2 (i.e., they both have the same mechanisms), but that they have different susceptibilities to each of them. The FH1 domains of mammalian formin mDia1, for example, may be more resilient to FH1 domain mechanoinhibition than Cdc12 at similar piconewton tensions, but both formin isoforms would still have the same mechanism generally.

One could also use steered MD simulations to apply tension to the FH1 domains of different formin isoforms and analyze how these domains behave differently when subjected to strain. One would imagine that the FH1 domains of Cdc12 should stand out in these studies. Secondly, an alternative simulation could exert forces on the FH2 domains of formin at

the barbed end to see how this accelerates the 'stepping' mechanism, similar to what was done in CG simulations (7).

Outside of formin, the microfluidics setup is useful for applying tensile and bending forces to actin filaments generally. It would be interesting to see if LIM domain binding could be activated under these conditions, perhaps following the protocol that Wioland et al. used to investigate the mechanosensitivity of cofilin (8). Additionally, the same mechanosensitivity assays that I have used for formin would be equally interesting for studying the mechanical response of ENA/VASP, which has yet to be investigated before as far as I am aware.

Outside of direct follow-up to the chapters presented in this thesis, there are gaps in understanding some of the most fundamental aspects of actin that new information and tools can only recently be deployed to gain answers. I am currently involved in a collaboration aimed at uncovering the mechanisms underlying the release of inorganic phosphate from actin subunits within filament interiors.

ADP-bound filaments are less stable than those with ATP bound. ABPs such as cofilin have higher affinities for ADP-bound filaments than in other nucleotide states (8-11). The nucleotide state in large part conveys the age of the actin filament as a signal to other components of the actin cytoskeleton and impacts the emerging actin network assembly and disassembly. However, the mechanism of inorganic phosphate release is not well characterized. I am currently working closely with Dr. Yihang Wang to establish both the release pathway and the corresponding free energy landscape using metadynamics simulations. We find that, in contrast to predictions based on actin filament structures, the hydrogen bond formed between residues R177 and N111 do not present a feasible rate-limiting gate for phosphate release from the back door of actin. Instead, our results show that the R177 to N111 hydrogen bond breaks and reforms

transiently in unbiased MD simulations under 1 μs in length. Instead, our preliminary free energy landscapes suggest that the highest energy barrier by far is breaking the interaction between the Mg^{2+} ion and the inorganic phosphate, which requires an increase in solvation to mediate phosphate release. However, once this interaction is broken, phosphate exits the protein molecule without the need to wait for long timescale conformational changes within the subunit interior.

Outside of my current research efforts, there are additional projects that MD simulations could be particularly helpful for shedding light on in the actin cytoskeleton. In particular, the interactions between profilin, formin, and actin have not been explained in satisfactory mechanistic detail. For example, profilin is known to catalyze nucleotide release from actin molecules bound to ADP. This is important for maintaining a pool of ATP-actin despite actin turnover disassembling what is largely ADP-bound actin molecules. It has been hypothesized that profilin binding to actin's barbed end opens the cleft between subdomains 2 and 4 at the pointed end of the actin subunit, creating additional space for ADP to be released. This hypothesis could be tested with enhanced sampling simulations that bias the unbinding of ADP into solution and reporting the importance of various conformational changes that arise in the presence or absence of bound profilin. One may find it useful to simultaneously bias the dihedral angle of the actin molecule in addition to the ligand unbinding CV to observe a two dimensional free energy landscape. It will also be interesting to characterize the behavior and dynamics of the nucleotide-free actin molecule, for which little is known. Fortunately, for anyone interested in these questions, there are high-resolution structures available of profilin-actin complexes.

Second, with the recent preprints of actin filament barbed ends becoming available at resolutions in the range of 3-4 Å (2, 3), I anticipate similarly well-resolved structures of formin FH2 domains bound to the barbed end of the actin filament becoming available in the next year or

two. Presumably there will be various isoforms reported. This should enable MD studies to shed light on various properties of different FH2 domains including how they have different gating factors, how they 'step' to remain processively associated with the filament barbed end and how this is modulated by tension, and importantly how the FH2 domains catalyze the release of profilin from the most recently added barbed end subunits. I am particularly interested in the latter because, seeing that barbed end subunits adopt monomeric twisted conformations and profilin binds with higher affinity to this conformation of actin, that the FH2 domains may encourage the release of profilin by simply flattening the barbed end subunits (1). It would be fascinating if different isoforms of formin are observed to flatten barbed end subunits to varying degrees, and this can be connected to the degree to which these formin molecules speed up actin filament elongation at the high concentration regime explored in Funk et al. (12).

Zooming out, the actin cytoskeleton has two large questions that I anticipate studies in the next decade will provide significant new understanding to the field. First is understanding how the actin cytoskeleton, microtubule cytoskeleton, and DNA are all interrelated. A growing body of recent research has supported the idea that crosstalk between the actin and microtubule cytoskeletons has physiologically important implications (13). In the past, the two major cytoskeletons have generally been treated separately and in isolation, with research groups specializing in studying one or the other. However, as more information becomes available about interactions between these two systems, there seems to be more reason for research to be performed at the interface of the two fields. In addition, the interplay between actin and gene expression has important implications and will be interesting to better understand the relationships. One interesting role for LIM domains has been as a regulator of gene expression by relaying information between the nucleus and cytoplasm (14). As more understanding develops

surrounding LIM domains binding to strained actin filaments, it will be particularly interesting to see how this turns on and off genes in response to mechanical stimulation.

Secondly, while actin is remarkably conserved across all eukaryotic lineages, prokaryotes have their own distinct cytoskeletons. However, there are fascinating similarities between the eukaryotic and prokaryotic cytoskeletons (15). Specifically, there are actin homologs present in prokaryotes– but these behave like and carry out the functions corresponding to microtubules in eukaryotic cells. Conversely, there are tubulin homologs in prokaryotes– but these behave like and carry out the functions of actin in eukaryotes. This fascinating reversal of function from what are presumably proteins originating from common ancestral proteins begs questions surrounding when, how, and why this change in behavior occurred. Furthermore, it suggests that there is a fundamental reason why functioning cells need to segregate processes to distinct cytoskeletons. I believe that research performed within the next decade will greatly push our understanding of these fundamental questions.

6.1 References

1. V. Zsolnay, H. H. Katkar, S. Z. Chou, T. D. Pollard, G. A. Voth, Structural basis for polarized elongation of actin filaments. *Proc Natl Acad Sci U S A* **117**, 30458-30464 (2020).
2. S. Z. Chou, T. D. Pollard, Cryo-EM structures of both ends of the actin filament explain why the barbed end elongates faster than the pointed end. *bioRxiv* 10.1101/2023.05.12.540494 (2023).
3. W. Oosterheert *et al.*, Molecular mechanisms of inorganic-phosphate release from the core and barbed end of actin filaments. *bioRxiv* 10.1101/2023.03.25.534205, 2023.2003.2025.534205 (2023).

4. N. O. Glenn *et al.*, The W-loop of alpha-cardiac actin is critical for heart function and endocardial cushion morphogenesis in zebrafish. *Mol Cell Biol* **32**, 3527-3540 (2012).

5. K. E. Homa *et al.*, Formin Cdc12's specific actin assembly properties are tailored for cytokinesis in fission yeast. *Biophys J* **120**, 2984-2997 (2021).

6. T. Litschel *et al.*, Reconstitution of contractile actomyosin rings in vesicles. *Nat Commun* **12**, 2254 (2021).

7. F. Aydin, N. Courtemanche, T. D. Pollard, G. A. Voth, Gating mechanisms during actin filament elongation by formins. *Elife* **7** (2018).

8. H. Wioland, A. Jegou, G. Romet-Lemonne, Torsional stress generated by ADF/cofilin on cross-linked actin filaments boosts their severing. *Proc Natl Acad Sci U S A* **116**, 2595-2602 (2019).

9. R. Dominguez, Nucleotide-dependent conformational changes in the actin filament: Subtler than expected. *Proc Natl Acad Sci U S A* **116**, 3959-3961 (2019).

10. W. Oosterheert, B. U. Klink, A. Belyy, S. Pospich, S. Raunser, Structural basis of actin filament assembly and aging. *Nature* **611**, 374-379 (2022).

11. C. Suarez *et al.*, Profilin regulates F-actin network homeostasis by favoring formin over Arp2/3 complex. *Dev Cell* **32**, 43-53 (2015).

12. J. Funk *et al.*, Profilin and formin constitute a pacemaker system for robust actin filament growth. *Elife* **8** (2019).

13. M. Dogterom, G. H. Koenderink, Actin-microtubule crosstalk in cell biology. *Nat Rev Mol Cell Biol* **20**, 38-54 (2019).

14. X. Sun *et al.*, Mechanosensing through Direct Binding of Tensed F-Actin by LIM Domains. *Dev Cell* **55**, 468-482.e467 (2020).

15. B. Wickstead, K. Gull, The evolution of the cytoskeleton. *Journal of Cell Biology* **194**, 513-525 (2011).

Appendix 1: Actin filament nucleation

Preface

The work presented in this appendix is in progress. It discusses research into the initial steps of spontaneous actin nucleation and is performed in collaboration with Thomas Pollard, David Kovar, and Gregory Voth.

Introduction

In 2001, Sept and McCammon published a computational study investigating the early stages of actin filament nucleation (i.e., dimerization, trimerization, etc.) (1). These rates suggested that dimers come together frequently ($k_{+1} \sim 10\ \mu M^{-1} s^{-1}$), but are extremely unstable, falling apart on the timescale of a few nanoseconds ($k_{-1} \sim 10^{8}\ s^{-1}$). Nearly 20 years later, Rosenbloom et al. reported a huge degeneracy of the rate constants that led to reasonable fits of actin assembly curves, but that the set of rates that fit the best conveyed a very different molecular picture. Instead of dimers forming frequently, dimers almost never form ($k_{+1} \sim 10^{-6}\ \mu M^{-1} s^{-1}$), but they are stable for minutes when they do ($k_{-1} \sim 10^{-2}\ s^{-1}$) (2). Rosenbloom proposed that the extremely slow forward reaction could be explained by a scheme in which only a small subpopulation of monomers are in an excited dimerization-competent conformation, so the effective concentration of "competent" monomers is much lower than the overall actin concentration. This past year, yet another group, Hundt et al., published a different set of rates claiming that dimers come together at rates similar to Sept's model ($k_{+1} \sim 10\ \mu M^{-1} s^{-1}$) but are stable for hundreds of milliseconds ($k_{-1} \sim 10\ s^{-1}$) (Fig. 6.2A and B) (3).

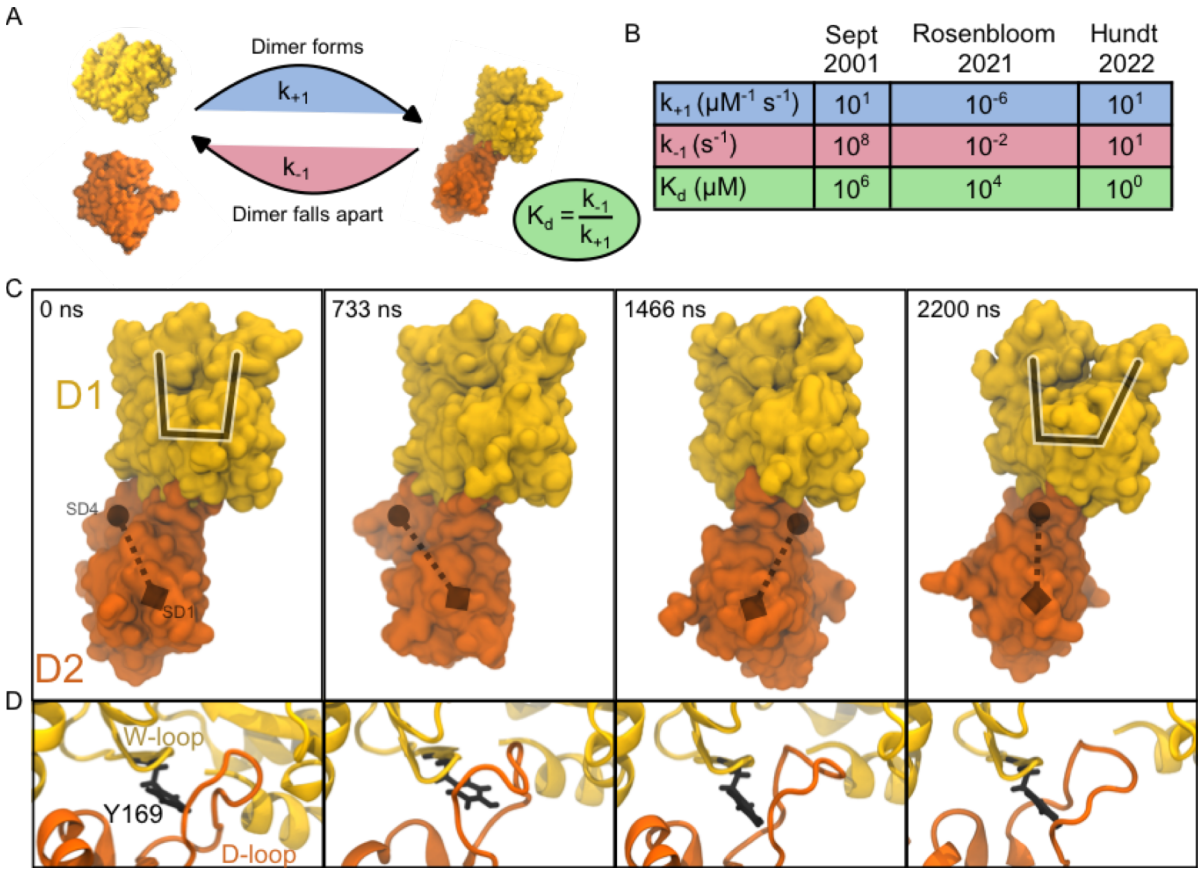

Figure 6.2. Dimers are stable for orders of magnitude longer than previously predicted. (A) schematic of the dimerization reaction. (B) Table of kinetic rates and dissociation constants predicted in three papers for the dimerization reaction. Note the orders of magnitude disagreements in rates. (C) Space-filling models of MD simulation snapshots of a longitudinal dimer remaining stable for at least 2.2 μs, orders of magnitude longer than predicted in Sept 2001. The dihedral angle of subunit D1 is illustrated and clearly expands as the simulation progresses. Subunit D2 fluctuates dynamically while remaining to D1 via its D-loop. A dotted line traces subdomain 1 (diamond) to subdomain 4 (circle) in all panels to highlight dynamics. (D) Despite the dynamics at the subunit-level, the D-loop to W-loop connection remains relatively stable and the W-loop of subunit D1 remains in the clamped state throughout the multi-microsecond simulation.

Given the large disagreements between the reported rates and dissociation constants for these reactions, any clarity from orthogonal methods that can point to which rates are reasonable will be valuable for the field. This is especially true because changing one of the rates in the set of rates, necessitates adjustments to all others. Realizing this, I have begun exploring the behavior of longitudinal dimers in solution.

The first key finding is that longitudinal dimers are stable for at least 2 orders of magnitude longer than predicted by the Sept model. Dimers in all-atom MD simulations are stable for simulations as long as 3.8 μs with no sign of dissociating (Fig. 6.2C). This calls into question the molecular picture put forth by Sept, which anticipated dimers falling apart after ~15 ns. However, all other rates are too slow to be tested in unbiased all-atom MD simulations. One could imagine enhanced sampling simulations designed to probe the free energy landscape, and therefore the rates, associated with the dimerization reaction.

The unbiased dimer simulations also showed an informative result. If one was to theorize the excited state conformation of a dimerization-competent monomer, it would likely have more similarities to a subunit in an actin filament than the typical monomer in solution, as this would promote the stabilizing interactions keeping actin filaments intact. Based on comparisons between actin monomers in solution and actin subunits in actin filaments, two primary structural differences become noticeable. First is that the monomer is in a twisted conformation, whereas the subunit in the filament interior is flattened, as discussed earlier. Secondly, the W-loop of the monomer is in a closed conformation, whereas the W-loop of subunits within filaments are 'clamped' upon the D-loop residues of the neighboring subunit (4). This D-loop to W-loop connection has been seen to be of enormous importance for the stability of inter-subunit interactions in both my study of filament ends, in which the barbed end subunit is attached to the filament through this connection alone, and in my study of filament fragmentation, in which breaks occur only where this connection is lost. Therefore, a leading hypothesis is that the W-loop should be more open in a dimerization-competent state than the ground state of a monomer. However, it has not been clear whether this W-loop opening observed in structures of monomers and interior subunits is coupled to the observed flattening transition that also occurs.

My long timescale MD simulations of dimers shed light on this question. Indeed, I see that the only important connection between dimers is the D-loop to W-loop connection. This alone keeps the two actin molecules in the dimer (D1 and D2) attached to one another, despite large subunit-level fluctuations (Fig. 6.2C). Additionally, it is clear that the W-loop remains in the more open 'clamped' orientation throughout the simulations (Fig. 6.2D). However, this is not coupled to subunit flattening in any noticeable way. The dihedral angle of D1, which maintains a clamped W-loop throughout the simulations, fluctuates, and tends towards more twisted values consistent with actin monomer structures (Fig. 6.2C, right). Therefore, it seems reasonable that a dimerization-competent monomer would need a more open W-loop, but not a flattened conformation.

To explore the conformational space possible for the W-loop of a monomer opening and closing, I have been using metadynamics simulations. This method biases the simulation to explore different regions of CV-space on shorter timescales than would occur in unbiased simulations (5). I defined a CV that describes the open state of the W-loop as an angle defined by the centers of mass of the alpha and beta carbons of 1) residues 168 to 170 (the W-loop), 2) residues 162, 163, 175, 176, and 3) residues 136 to 140. Using this angle definition, the monomer's closed state is ~44.5° and the subunit within a filament maintains a more open value of ~60.5°. In metadynamics simulations biasing this angle CV, a surprising result emerges. In addition to the ground state of a closed W-loop as observed in crystal structures of actin monomers, there is another higher energy metastable state (Fig. 6.3). However, the higher energy state is not at the ~60.5° value observed in cryo-EM of actin subunits within filaments, it is significantly higher around ~75°. In fact, the clamped orientation looks to be roughly at the transition state between the global minimum closed state and the new open state observed through metadynamics.

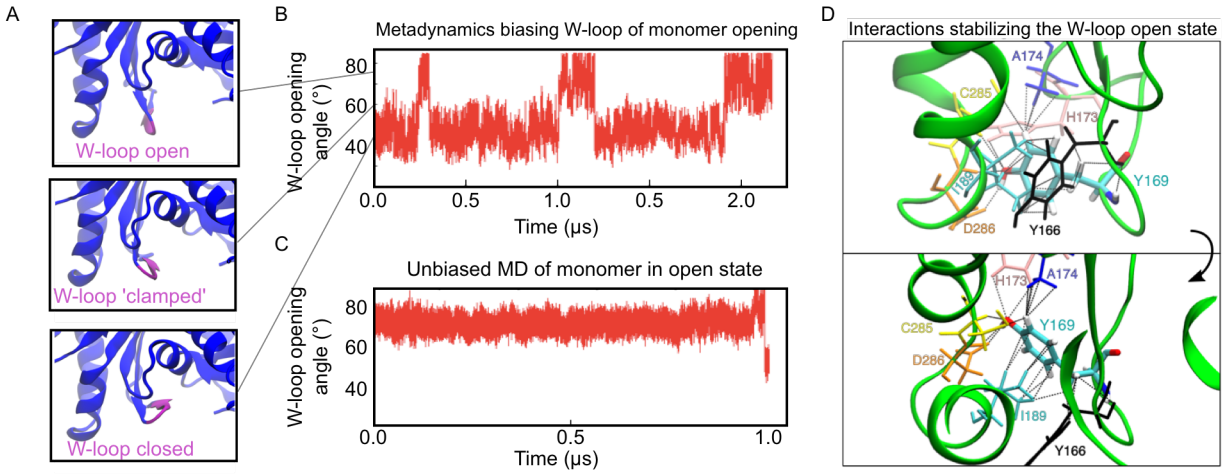

Figure 6.3. Actin monomers in solution can adopt a metastable W-loop open conformation. (A) Snapshots illustrating the relevant conformations of the W-loop (purple) of a monomer (blue). (B) Time course of the W-loop opening angle CV biased in metadynamics. The time course is characteristic of systems with two states. (C) Time course of the W-loop angle CV of a monomer started in the open-W-loop state in an unbiased MD simulation. This remains stable for ~1 μs before transitioning back to the closed state. (D) Depiction of the residue-residue contacts stabilizing the W-loop open state.

Importantly, the open state centered around 75° is a bonafide metastable state, consistently getting trapped in this orientation for prolonged periods of time. This is in contrast to what one might have expected, where deviations from the global energy minimum (closed state) have diminishing probabilities of occurring. To confirm that the existence of the metastable open state is not an artifact of the metadynamics scheme, I began an unbiased simulation in the W-loop open state and observe that this remains in the open state for ~1 μs before transitioning back to the closed state. This suggests that the open state sampled using enhanced sampling is indeed metastable. This is particularly intriguing because the W-loop orientation, even more open than in filament interiors, is exactly the kind of excited state conformation that we would predict would lead to the formation of stable dimers, as the D-loop to W-loop intermolecular connection can be made much more easily.

The interactions that stabilize the W-loop open state are sensible as well (Fig. 6.3D). The primary interactions are between residue Y169 of the W-loop interacting in a hydrogen bond network with residues 285-290, as well as H173 and A174. In particular, the interaction between Y169 and D286 appears to be particularly electrostatically favorable and therefore stabilizing.

Follow-up work on this research could include acquiring a free energy landscape for the W-loop opening, so as to estimate the forward and backward rates of the conformational change, and even more importantly, estimate the prevalence of the open state of the monomer in solution. It will be very interesting to know what fraction of monomers are in this excited, dimerization-competent state. Without this information, the takeaway is limited to the observation that some fraction of the monomers will be in the W-loop open state.

Additionally, one could mutate the residues involved in stabilizing the W-loop in the open conformation in order to observe the effect on the nucleation rates *in vitro*. In particular, D286G is a naturally occurring mutation that causes muscular dystrophy that may be interesting to investigate (6, 7). Alternatively, one could establish the free energy landscape of the W-loop opening transition for different WT actin sequences, for instance mammalian and yeast actin, and see if this can be connected to the observed nucleation rates *in vitro*.

Outside of the W-loop, the novel experimental technique used in Hundt and coauthors' study, in which individual oligomeric species were directly observed, is likely to be a rich tool for settling the discrepancies between reported rates. However, repeating their study is likely necessary to gain acceptance of the rate constants from the field in general (3). For one, it would be advantageous to use pyrene assembly curves at multiple concentrations of actin instead of light scattering data at a single actin concentration. Secondly, because spontaneous nucleation is so sensitive to the presence of dimers at time zero, it would be desirable to use a G-150 column in addition to or instead of a G-75 column to have greater confidence that their samples were not

contaminated with oligomers, capping protein, or covalently cross-linked dimers that have been found in actin purified from acetone powder. Thirdly, the authors incubated actin solutions for a period at higher concentrations and then dilute the solutions up to 20-fold directly before performing photometry measurements. This potentially introduces artifacts both because of the potential for depolymerization as well as the potential for severing due to mechanical forces. However, if these experimental concerns are addressed, the direct observation of oligomeric species that photometry offers is an additional rich dataset that can be used to confidently establish rates given the large degeneracy of rates that fit pyrene assembly curves well, as reported in Rosenbloom.

A.1 References

1. D. Sept, J. A. McCammon, Thermodynamics and kinetics of actin filament nucleation. *Biophys J* **81**, 667-674 (2001).

2. A. D. Rosenbloom, E. W. Kovar, D. R. Kovar, L. M. Loew, T. D. Pollard, Mechanism of actin filament nucleation. *Biophys J* **120**, 4399-4417 (2021).

3. N. Hundt *et al.*, Direct observation of the molecular mechanism underlying protein polymerization. *Sci Adv* **8**, eabm7935 (2022).

4. S. Z. Chou, T. D. Pollard, Mechanism of actin polymerization revealed by cryo-EM structures of actin filaments with three different bound nucleotides. *Proc Natl Acad Sci U S A* **116**, 4265-4274 (2019).

5. G. Bussi, A. Laio, Using metadynamics to explore complex free-energy landscapes. *Nature Reviews Physics* **2**, 200-212 (2020).

6. F. Parker, T. G. Baboolal, M. Peckham, Actin Mutations and Their Role in Disease. *Int J Mol Sci* **21** (2020).

7. J. Fan *et al.*, Molecular Consequences of the Myopathy-Related D286G Mutation on Actin Function. *Front Physiol* **9**, 1756 (2018).